2011

From the Killing Fields to the self-consistent field: The adventures of a Cambodian refugee in quantum chemistry

Sarom Sok
Iowa State University

From the Killing Fields to the self-consistent field:

The adventures of a Cambodian refugee in quantum chemistry

by

Sarom Sok

A dissertation submitted to the graduate faculty

in partial fulfillment of the requirements for the degree of

DOCTOR OF PHILOSOPHY

Major: Physical Chemistry

Program of Study Committee:
Mark S. Gordon, Major Professor
Kai-Ming Ho
Thomas A. Holme
Klaus Schmidt-Rohr
Xueyu Song

Iowa State University

Ames, Iowa

2011

DEDICATION

I dedicate this thesis to my mother, **Phy Leang**, a survivor of the Khmer Rouge genocide. I love you and thank you for the sacrifices that you have made in order for me to have this opportunity.

To further honor my mother, a petition for name change to **Sarom Sok Leang** was filed in the Circuit Court of Arlington, Virginia on May 16, 2011.

TABLE OF CONTENTS

CHAPTER 1. GENERAL INTRODUCTION

Introduction

The importance of electronic structure methods in the field of chemistry was underscored in 1998 with the Nobel Prize presentation to Walter Kohn and the late Sir John A. Pople for the development of computational methods in quantum chemistry. Since then, the shift towards a multi-core multi-parallel computing paradigm [1] and the development of highly efficient and highly parallel quantum chemistry codes [2,3] allow chemists to augment research with computational calculations in efforts to validate and/or predict chemical findings. The iterative process of theory validating experiment and experiment validating theory is the self-consistent procedure that has helped to evolve the science. However, much care must be taken when using quantum chemical tools to interpret or model experiments. Solvent effects are commonly omitted in quantum chemistry calculations. Most experiments are performed in the condensed phase. Solvents have been found to significantly alter the energetics associated with chemical processes [4] in addition to changing the structure [5] and the photochemistry [6-10] of the solute. Approaches are available to treat solvent effects; however, not all approaches treat solvents equally well, and care must be taken in choosing an appropriate solvent model [11]. This thesis will focus on the use of quantum chemical tools to study chemical phenomena in water, specifically the hydrolysis mechanism of 1-substituted silatranes and the solvent-induced shifts of the $\pi \rightarrow \pi^*$ charge transfer state of *p*-nitroaniline. Assessment of the performance of some of the quantum chemical tools used and the application of a new approach for the treatment of solvent effects will also be presented.

Dissertation Organization

The computational methods employed in the current body of work are described in the Introduction. The next two chapters detail the study of chemical systems in aqueous solution, while the last two chapters investigate the performance of various electronic-structure methods.

Chapter 2 describes the theoretical mechanistic study of the hydrolysis of 1-substituted silatranes. The study investigates why the hydrolysis process is experimentally

observed to proceed much faster in the presence of an acid catalyst. Chapter 3 applies the combined time-dependent density functional theory/effective fragment potential method (TDDFT/EFP) to the study of the solvent-induced shift of the lowest $\pi \rightarrow \pi^*$ charge transfer excited state of *p*-nitroaniline. The accuracy of the TDDFT/EFP calculated solvent shift in water is compared with experiment along with highly correlated *ab initio* based methods, and the source of the solvent shift is analyzed in terms of solute-solvent interaction contributions.

The performance of various density functionals for the calculation of vertically excited states within the linear response time-dependent density functional theory formalism is analyzed in a benchmark investigation presented in Chapter 4. The goal of this project is to determine if the performance of sophisticated ground state density functionals employing the kinetic energy density carries over to the excited state. In Chapter 5, the details of a combined coupled-cluster/effective fragment potential (CC/EFP) approach is presented and applied to the study of the hydrolysis process of 1-substituted silatranes from Chapter 2, the solvatochromic shift of *p*-nitroaniline from Chapter 3, and the solvation of negatively charged ions from previous works in the literature. The focus of this project is to assess the performance of the CC/EFP approach, which limits the mutual equilibration of the solvent polarization to the optimization of the reference wavefunction, for treatment of solvent effects.

Theoretical Background

The field of quantum chemistry merges the study of chemical systems with quantum theory. Because of the wave-particle duality of electrons and energy, the physics of a chemical system is governed by the laws of quantum mechanics. In quantum mechanics, the state of a physical system in the absence of a time-dependent potential is defined by a wavefunction dependent on both nuclear and electronic coordinates,

$$\Psi \qquad (1)$$

In addition, all physically measurable quantities (observables) of a system are described by an operator [12]. Quantum chemists are interested in the energy associated with a chemical system; therefore, the operator governing the total energy is the Hamiltonian and consists of five terms,

$$\hat{H} = \hat{T}_e + \hat{T}_n + \hat{V}_{en} + \hat{V}_{ee} + \hat{V}_{nn} \tag{2}$$

The first two terms in Eq. (2), in atomic units, are the kinetic energy operators of the electrons and nuclei,

$$\hat{T}_e = -\sum_{i=1}^{N} \frac{\nabla_i^2}{2} \tag{3}$$

$$\hat{T}_n = -\sum_{A=1}^{M} \frac{\nabla_A^2}{2M_A} \tag{4}$$

The summations in Eq. (3) and Eq. (4) are over the total number of electrons N and nuclei M, respectively, M_A is the mass of nucleus A and ∇^2 is the Laplacian operator,

$$\nabla^2 \equiv \frac{\partial}{\partial x^2} + \frac{\partial}{\partial y^2} + \frac{\partial}{\partial z^2} \tag{5}$$

The third term in Eq. (2) describes the electron-nuclear attraction,

$$\hat{V}_{en} = -\sum_{i=1}^{N} \sum_{A=1}^{M} \frac{Z_A}{r_{iA}} \tag{6}$$

where Z_A is the charge of nucleus A and r_{iA} is the distance between electron i and nucleus A. The last two terms in Eq. (2) describe the electron-electron and nuclear-nuclear repulsions,

$$\hat{V}_{ee} = \sum_{i<j}^{N} \frac{1}{r_{ij}} \tag{7}$$

$$\hat{V}_{nn} = \sum_{A<B}^{M} \frac{Z_A Z_B}{r_{AB}} \tag{8}$$

r_{ij} is the distance between electrons i and j, and r_{AB} is the distance between nucleus A and B. Obtaining the total energy of a chemical system requires solving the following eigenvalue problem,

$$\hat{H}\Psi = E\Psi \tag{9}$$

Eq. (9) is also referred to as the time-independent non-relativistic Schrödinger equation. The dependence of the wavefunction in Eq. (1) on both nuclear and electronic coordinates makes solving the Schrödinger equation difficult. To simplify the problem, an approximation is

made by noting the difference in mass between electrons and nuclei (protons and neutrons are ≈ 1800 times heavier than electrons) [13]. In the Born-Oppenheimer "clamped nuclei" approximation [14], the nuclei are stationary with respect to electronic motion. Or simply, electrons move in the potential of the nuclei. As a result, the Hamiltonian in Eq. (2) simplifies to

$$\hat{H} = \hat{T}_e + \hat{V}_{en} + \hat{V}_{ee} = \hat{H}_{elec} \tag{10}$$

and is referred to as the electronic Hamiltonian.

$$\hat{H}_{elec}\Psi_{elec} = E_{elec}\Psi_{elec} \tag{11}$$

The total energy of the system, E_{total}, within the Born-Oppenheimer approximation is obtained by solving for the electronic energy in Eq. (11) and adding the nuclear repulsion term from Eq. (8),

$$E_{total} = E_{elec} + E_{nucl} \tag{12}$$

Due to the inseparability of the electron-electron distance, r_{ij}, in Eq. (7), obtaining a closed solution to Eq. (11) is not possible and further approximations are made.

The crudest approximation is the independent particle model (IPM), in which a separable wavefunction can be constructed as a product of one-electron spin-orbitals $\phi_i(\boldsymbol{r}_i)$,

$$\Psi_{\text{IPM}} = \phi_1(\boldsymbol{r}_1)\phi_2(\boldsymbol{r}_2)\cdots\phi_n(\boldsymbol{r}_n) \tag{13}$$

The independent particle model, combined with the Variational Principle, results in an average treatment for electron repulsion,

$$V_{ee} \approx V_{\text{HF}} \tag{14}$$

Incorporating the required antisymmetry into the wavefunction by using Slater determinants within the variationally optimized independent particle model,

$$\Psi_{\text{HF}} = \frac{1}{\sqrt{N!}}\begin{vmatrix} \phi_1(\boldsymbol{r}_1) & \phi_2(\boldsymbol{r}_1) & \cdots & \phi_N(\boldsymbol{r}_1) \\ \phi_1(\boldsymbol{r}_2) & \phi_2(\boldsymbol{r}_2) & \cdots & \phi_N(\boldsymbol{r}_2) \\ \vdots & \vdots & \ddots & \vdots \\ \phi_1(\boldsymbol{r}_3) & \phi_2(\boldsymbol{r}_3) & \cdots & \phi_N(\boldsymbol{r}_3) \end{vmatrix} = \frac{1}{\sqrt{N!}}\det\left[\phi_1\phi_2\cdots\phi_3\right] \tag{15}$$

leads to the Hartree-Fock (HF) method [15]. In Eq. (15), N is a normalization constant. The use of (antisymmetric) Slater determinants ensures that the antisymmetry (Pauli exclusion) principle is satisfied [16]. The HF energy for a closed-shell system is,

$$E_{\mathrm{HF}} = \left\langle \Psi_{\mathrm{HF}} \left| \hat{H}_{elec} \right| \Psi_{\mathrm{HF}} \right\rangle = 2\sum_{i=1}^{N/2} h_{ii} + \sum_{i=1}^{N/2}\sum_{j=1}^{N/2} \left(2J_{ij} - K_{ij} \right) \tag{16}$$

where i and j index electrons and h_{ii} defines the one-electron integrals,

$$h_{ii} = \left(i \left| h_{ii} \right| i \right) = \int \psi_i^* \left(\boldsymbol{r}_1 \right) \left(-\frac{1}{2}\nabla_i^2 - \sum_{A=1}^{M} \frac{Z_A}{r_{iA}} \right) \psi_i \left(\boldsymbol{r}_1 \right) d\boldsymbol{r}_1 \tag{17}$$

and the two-electron integrals are,

$$J_{ij} = \left(ii \left| jj \right. \right) = \int\int \psi_i^* \left(\boldsymbol{r}_1 \right) \psi_i \left(\boldsymbol{r}_1 \right) \frac{1}{\left| \boldsymbol{r}_1 - \boldsymbol{r}_2 \right|} \psi_j^* \left(\boldsymbol{r}_2 \right) \psi_j \left(\boldsymbol{r}_2 \right) d\boldsymbol{r}_1 d\boldsymbol{r}_2 \tag{18}$$

$$K_{ij} = \left(ij \left| ij \right. \right) = \int\int \psi_i^* \left(\boldsymbol{r}_1 \right) \psi_j \left(\boldsymbol{r}_1 \right) \frac{1}{\left| \boldsymbol{r}_1 - \boldsymbol{r}_2 \right|} \psi_j^* \left(\boldsymbol{r}_2 \right) \psi_i \left(\boldsymbol{r}_2 \right) d\boldsymbol{r}_1 d\boldsymbol{r}_2 \tag{19}$$

J_{ij} and K_{ij} are referred to as the Coulomb and exchange integral, respectively. The HF energy expression in Eq. (16) can be equivalently written as,

$$E_{\mathrm{HF}} = \sum_{i=1}^{N/2} \left[2\left(i \left| h_{ii} \right| i \right) + \sum_{j}^{N/2} 2\left(ii \left| jj \right. \right) - \left(ij \left| ij \right. \right) \right] \tag{20}$$

The HF method is based on the independent particle model and does not consider the instantaneous repulsion of electrons. As such, the energy associated with the correlated motion of electrons, $E_{\mathrm{correlation}}$, is defined as the difference between the HF energy and the exact non-relativistic energy within the Born-Oppenheimer approximation,

$$E_{\mathrm{correlation}} = E_{\mathrm{HF}} - E \tag{21}$$

The HF method can normally accounts for more than 99% of the total energy; however, the energies associated with chemical phenomena, e. g., bond dissociation and electronic excitation, can only be predicted with accuracy if electron correlation is included in the calculation. Much effort in quantum chemistry has been invested in the development of computationally efficient and accurate methods for capturing the electron correlation energy.

A method that attempts to capture electron correlation is density functional theory

(DFT) [17-20]. DFT approaches the problem of calculating the electron correlation energy by noting that the energy is a functional of the electronic density,

$$\rho(\boldsymbol{r}_1) = N\int\int\left|\Psi(\boldsymbol{x}_1,\boldsymbol{x}_2,\ldots\boldsymbol{x}_N)\right|^2 ds_1 d\boldsymbol{x}_2\ldots d\boldsymbol{x}_N \tag{22}$$

a function of three variables, x, y, and z. If the exact electronic density of a chemical system is known, then the positions of the nuclei are also known from the cusps in the density. The total number of electrons of the system is obtained from,

$$\int\rho(\boldsymbol{r})d\boldsymbol{r} = N \tag{23}$$

The theoretical foundation for DFT was established in a seminal paper by Hohenberg and Kohn [19]. However, the ability to link between the electronic density and the energy of a system requires the knowledge of the universal functional. The paper by Hohenberg and Kohn established the formalism for DFT, but this paper does not provide an approach to obtaining the universal functional. It is unclear how one would go about obtaining the electronic density without prior knowledge of the wavefunction for the system. Kohn and Sham [20] introduced a formalism for density functional theory based on calculations that made use of the methods currently available in quantum chemistry codes, i.e. HF. Kohn-Sham DFT makes similar use of the independent particle model and then partially corrects for this assumption by adding an exchange-correlation contribution to the calculation of the electronic energy,

$$E_{\mathrm{DFT}} = \sum_{i=1}^{N/2}\left[2(i\,|\,h_{ii}\,|\,i) + \sum_{j}^{N/2}2(ii\,|\,jj) - (\phi_i\,|\,v_{xc}\,|\,\phi_i)\right] \tag{24}$$

Comparing Eq. (24) with Eq. (20) shows the overlap between HF and KS theory. The exchange-correlation potential is defined as the functional derivative of the exchange-correlation energy with respect to the electronic density,

$$v_{xc} = \frac{\delta E_{xc}}{\delta\rho} \tag{25}$$

The exchange-correlation energy is defined as,

$$E_{xc} = \int\rho(\boldsymbol{r})f(\rho_\alpha,\rho_\beta,\gamma_{\alpha\alpha},\gamma_{\alpha\beta},\gamma_{\beta\beta},\tau_\alpha,\tau_\beta)d\boldsymbol{r} \tag{26}$$

where f is the density functional approximation to the universal functional. The density gradient invariants are defined as,

$$\gamma_{\alpha\alpha} = \nabla\rho_\alpha \cdot \nabla\rho_\alpha, \qquad \gamma_{\alpha\beta} = \nabla\rho_\alpha \cdot \nabla\rho_\beta, \qquad \gamma_{\beta\beta} = \nabla\rho_\beta \cdot \nabla\rho_\beta, \tag{27}$$

and the kinetic energy density is given as,

$$\tau_\sigma(\boldsymbol{r}) = \sum_i^{\text{occ}} \frac{1}{2} |\nabla\phi_{i\sigma}(\boldsymbol{r}_i)|^2 \tag{28}$$

Density functional approximations may be classified according to their level of sophistication. The local density approximation (LDA) functionals depend only on the electronic spin densities,

$$f_{\text{LDA}}(\rho_\alpha, \rho_\beta) \tag{29}$$

while generalized gradient approximation (GGA) functionals include the density gradient invariants,

$$f_{\text{GGA}}(\rho_\alpha, \rho_\beta, \gamma_{\alpha\alpha}, \gamma_{\alpha\beta}, \gamma_{\beta\beta}) \tag{30}$$

Meta-generalized gradient approximation (meta-GGA) functionals include the electron spin densities, density gradient invariants, and the kinetic energy density,

$$f_{\text{meta-GGA}}(\rho_\alpha, \rho_\beta, \gamma_{\alpha\alpha}, \gamma_{\alpha\beta}, \gamma_{\beta\beta}, \tau_\alpha, \tau_\beta) \tag{31}$$

Functionals that make use of an admixture, c_{HF}, of HF exchange,

$$E_{\text{Hybrid-DFT}} = \sum_{i=1}^{N/2}\left[2(i|h_{ii}|i) + \sum_j^{N/2} 2(ii|jj) - c_{\text{HF}}(ij|ij) - (\phi_i|v_{xc}|\phi_i)\right] \tag{32}$$

are referred to as global hybrid density functionals. Functionals in which $c_{\text{HF}} = 0$ are classified as pure density functionals.

Capturing electron correlation using wavefunction based methods can be achieved through electronic excitations. Obtaining the total non-relativistic energy within the Born-Oppenheimer approximation can be achieved using the full configuration-interaction (CI) method. In full CI, the wavefunction is defined as [21],

$$\Psi_{\text{CI}} = \Phi_{\text{ref}} + \sum_i^{\text{occ}}\sum_a^{\text{virt}} C_i^a \Phi_i^a + \sum_{i<j}^{\text{occ}}\sum_{a<b}^{\text{virt}} C_{ij}^{ab}\Phi_{ij}^{ab} + \sum_{i<j<k}^{\text{occ}}\sum_{a<b<c}^{\text{virt}} C_{ijk}^{abc}\Phi_{ijk}^{abc} + \ldots \tag{33}$$

where i, j, k denote occupied (occ) orbitals and a, b, c denote virtual (virt) orbitals. The first term in Eq. (33) is the reference wavefunction, Φ_{ref}, normally taken as the HF solution. The second term in Eq. (33) denotes single excitations from the reference state. The variable C_i^a is the CI coefficient associated with the excitation, Φ_i^a. The CI coefficient measures the contribution of an excitation to the CI wavefunction. The third and fourth terms in Eq. (33) are double and triple excitation terms, respectively, up to N-fold excitations, where N is the number of electrons. Full CI scales exponentially, and performing full CI calculations is only possible for small chemical systems. In practice, the number of excitations is truncated. Truncating Eq. (33) at single excitations gives the CIS (single excitations) method but does not offer any improvement to the ground-state energy due to Brillouin's Theorem [22]. Truncation at double excitations is necessary to improve the HF ground state energy. However, the scaling of the CISD (singles and doubles excitations) method is on the order of $O\left(N^6\right)$ where N is a measure of system size [23].

A computationally efficient alternative to CISD is Møller-Plesset second order perturbation theory (MP2) [13,24] which has a formal scaling of $O\left(N^5\right)$,

$$E^{(2)} = \sum_{i<j}^{\text{occ}} \sum_{a<b}^{\text{virt}} \frac{\left[(ij \mid ab) - (ia \mid jb)\right]^2}{\varepsilon_i + \varepsilon_j - \varepsilon_a - \varepsilon_b} \tag{34}$$

Efficiently capturing electron correlation beyond MP2 can be accomplished within many-body theory with coupled-cluster (CC) theory. CC theory uses an exponential *ansatz* to convert a single-reference wavefunction, Φ_{ref}, into the exact wavefunction,

$$\Psi_{\text{CC}} = \exp\left(\hat{T}\right)\Phi_{\text{ref}} = \left(1 + \hat{T} + \frac{1}{2!}\hat{T}^2 + \frac{1}{3!}\hat{T}^3 + \ldots\right)\Phi_{\text{ref}} \tag{35}$$

The right-hand side of Eq. (35) shows the Taylor series expansion of the cluster operator, and

$$\hat{T} = \hat{T}_1 + \hat{T}_2 + \ldots + \hat{T}_n \tag{36}$$

where n is the total number of electrons in the system. Operating on the reference wavefunction (usually the HF wavefunction) yields,

$$\hat{T}_n \Phi_{\text{ref}} = \sum_{i<j<k<\ldots}^{\text{occ}} \sum_{a<b<c<\ldots}^{\text{virt}} t_{ijk\ldots}^{abc\ldots} \Phi_{ijk\ldots}^{abc\ldots} \tag{37}$$

and $t_{ijk\ldots}^{abc\ldots}$ denotes the CC amplitudes (CI-like coefficients) associated with the corresponding excitation operator, $\hat{T}_n$. Higher order excitations contribute to the CC energy indirectly through the CC amplitudes [23,25]. CC theory is a powerful tool for capturing electron correlation.

References

1. Janssen, C. J.; Nielsen, I. M. B. *Parallel Computing in Quantum Chemistry*, CRC Press, New York, **2008**.
2. Gordon, M. S.; Schmidt, M. W. Advances in Electronic Structure Theory: GAMESS: A Decade Later. In *Theory and Applications of Computational Chemistry: The First Forty Years*; Dykstra, C. E., Frenking, G., Kim, K. S., Scuseria, G. E., Eds.; Elsevier, Amsterdam, **2005**; pp. 1167.
3. Valiev, M.; Bylaska, E. J.; Govind, N.; Kowalski, K.; Straatsma, T. P.; Van Dam, H. J. J.; Wang, D.; Nieplocha, J.; Apra, E.; Windows, T. L.; Jong, W. A. *Comp. Phys. Comm.* **2010**, 181, 1477.
4. Kudo, T.; Gordon, M. S. *J. Am. Chem. Soc.* **1998**, 120, 11432.
5. Tortonda, F. R.; Pascual-Ahuir, J. L.; Silla, E.; Tunon, I. *Chem. Phys. Lett.* **1996**, 21.
6. Arora, P.; Slipchenko, L. V.; Webb, S. P.; DeFusco, A.; Gordon, M. S. *J. Phys. Chem. A* **2010**, 114, 6742.
7. Slipchenko, L. V. *J. Phys. Chem. A* **2010**, 114, 8824.
8. Kosenkov, D.; Slipchenko, L. V. *J. Phys. Chem. A* **2011**, 115, 392.
9. Yoo, S.; Zahariev, F.; Sok, S.; Gordon, M. S. *J. Chem. Phys.* **2008**, 129, 144112-1.
10. Defusco, A.; Ivanic, J.; Schmidt, M. W.; Gordon, M. S. *J. Phys. Chem. A* ASAP **April 14, 2011**.
11. Canuto, S., Eds.; *Solvation Effects in Molecules and Biomolecules: Computational Methods and Applications*, Springer Science, The Netherlands, **2008**.
12. Cohen-Tannoudji, C.; Diu, B.; Laloö, F. *Quantum Mechanics*, John Wiley & Sons, New York, **2005**.
13. Cramer, C. J. *Essentials of Computational Chemistry Theories and Models*, John Wiley & Son, New Jersey, **2004**.
14. Born, M.; Oppenheimer, R. Zur Quantentheorie der Molekeln. *Ann. Phys. (Leipzig)* **1927**, 84, 457.
15. Szabo, A.; Ostlund, N. S. *Modern Quantum Chemistry Introduction to Advanced Electronic Structure Theory*, Dover, New York, **1996**.
16. Levine, I. N. *Quantum Chemistry*, Prentice Hall, New York, **2009**.
17. Parr, R. G. *Annu. Rev. Phys. Chem.* **1995**, 46, 701.
18. Parr, R. G.; Yang, W. *Density –Functional Theory of Atoms and Molecules*, Oxford University Press, New York, **1989**.
19. Hohenberg, P.; Kohn, W. *Phys. Rev. B.* **1964**, 136, 864.
20. Kohn, W.; Sham, L. J. *Phys. Rev. A* **1965**, 140, 1133.
21. Bartlett, R. J; Stanton, J. F. Application of Post-Hartree-Fock Methods: A Tutorial. In *Rev. Comput. Chem.*; Vol. 5, Lipkowitz, K. B., Boyd, D. B., Eds.; Wiley-VCH, New York, **2000** ; pp. 65.
22. Piela, L. *Ideas of Quantum Chemistry*, Elsevier, New York, **2007**.

23. Shavitt, I.; Bartlett, R. J. *Many-Body Methods in Chemistry and Physics: MBPT and Coupled-Cluster Theory*, Cambridge University Press, New York, **2009**.
24. Jensen, F. *Introduction to Computational Chemistry*, John Wiley & Sons, New York, **1999**.
25. Crawford, D. T.; Schaefer III, H. F. An Introduction to Coupled Cluster Theory for Computational Chemist. In *Rev. Comput. Chem.*; Vol. 14, Lipkowitz, K. B., Boyd, D. B., Eds.; Wiley-VCH, New York, **2000** ; pp. 33.

CHAPTER 2. A DASH OF PROTONS: A THEORETICAL STUDY ON THE HYDROLYSIS MECHANISM OF 1-SUBSTITUTED SILATRANES AND THEIR PROTONATED ANALOGS

A paper submitted to *Computational and Theoretical Chemistry*

Sarom Sok[†] and Mark S. Gordon[†]

Abstract

A*b initio* calculations were carried out to study the hydrolysis mechanism of 1-substituted silatranes in the presence of an acid (acid-catalyzed) and an additional water (water-assisted). Compared with the neutral hydrolysis mechanism involving one water, use of an acid catalyst reduces the barrier associated with the rate-limiting step by ≈ 14 kcal/mol. A modest decrease of ≈ 5 kcal/mol is predicted when an additional water molecule is added to the neutral hydrolysis mechanism involving one water. The combination of an acid catalyst and an additional water molecule reduces the barrier by ≈ 27 kcal/mol. Bond order analysis suggests ring cleavage involving the bond breaking of a siloxane and silanol group during the neutral and acid-catalyzed hydrolysis of 1-substituted silatranes, respectively. Solvent effects, represented by the PCM continuum model, do not qualitatively alter computational gas-phase results.

[†] Department of Chemistry and Ames Laboratory, Iowa State University, Ames, IA 50011-3111

Figure 1. Structure for 1-substituted silatrane.

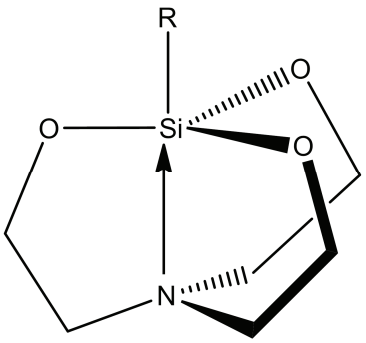

R = H, Cl, F, CH_3, NH_2, OH, PH_2, SiH_3

1. Introduction

Silatranes belong to a special class of biologically active heterocyclic pentacoordinated organosilicon compounds with no biologically active carbon analogs [1,2]. Frye *et al.* first reported the synthesis and characterization of silatranes in 1961 (initially referred to as triptych-siloxazolidines), Figure 1 [3]. The Frye *et al.* experimental observations suggest a transannular "dative bond" between silicon and nitrogen, stability against nucleophilic reactions and reluctance to neutralize in glacial acetic acid (strong acid). X-ray diffraction analysis confirms a tricyclic cage structure involving hypervalent silicon centered in a trigonal-bipyramidal arrangement, surrounded equatorially by three endocyclic oxygens and axially by a substituent group and an opposing nitrogen; with the nitrogen lone pair directed towards the positively charged silicon center in an electrostatically favorable arrangement [4]. Adding to the structural novelty of silatranes, the transannular silicon-nitrogen distance falls between the sum of their covalent and nonbonded radii, 1.89 Å and 2.69 Å, respectively, suggesting a weak transannular interaction between Si and N [5]. Since the first reported synthesis and characterization, the product of the alcoholysis of trialkoxysilanes by trialkanolamines has been the subject of many experimental [6-55] and theoretical [56-74] studies and several recent reviews [75,76].

The biological activities of silatranes (*in vivo*) are numerous. 5-*p*-chlorophenyl silatrane was successfully employed as an environmentally safe and highly acute rodenticide, due to rapid hydrolytic decay of aromatically substituted silatranes and reduction to biologically inert products [19-21]. In contrast to the highly toxic arylsilatranes, aliphatic

substituted silatranes were found to be useful organosilicon compounds for applications in medicine and agriculture [75]. Additional biological applications of 1-substituted silatranes include blocking chloride ion channels of γ-aminobutyric acid (GABA) receptors (anticonvulsants) [22], inhibiting cholesterol biosynthesis (hypocholesterolemic) [23], treating alopecia (hair growth) [1], regenerating tissue [24], fighting cancer (carcinostatic) [25], enhancing plant yield and germination [26], and many others [18,27-29,75,76].

Similarly, non-biological applications of silatranes are plentiful. Silatranes have been employed as strong reducing agents for several organic compounds [30]. *m*-chlorophenoxy-silatrane inhibits aluminum corrosion [31]. Several reports use silatranes as hydrolytically stable precursors for the sol-gel process of creating meso- and micro-porous materials [32-35]. The stability of 1-(3-amoniopropyl)silatrane at neutral pH towards aqueous solvolysis and polymerization makes it an ideal surface modifier for deoxyribonucleic acid (DNA) imaging [36]. Silatranes can convert residue generated in combustion (fly ash) into raw materials serving as precursors for silicates and aluminates [37]. Recently, silatranes have been used as solvent-induced molecular propellers [38].

All biological and non-biological applications depend on the hydrolytic stability of 1-substituted silatranes. The pronounced hydrolytic stability of 1-substituted silatranes compared to related acyclic analogs, such as Si-substituted trialkoxysilanes and tris(2-aminoalkoxy)silanes, is often noted in experimental observations [39-42]. The stability and steric hindrance of the tricyclic alkyoxy linkage ("cage effect") and the transannular interaction between silicon and nitrogen are credited with the enhanced hydrolytic stability [39,76]. The hydrolytic decomposition of 1-substituted silatrane, shown in Eq. (1), involves the addition of three units of water to produce the hydrolysis products tri-(2-hydroxyalkyl)amine and Si-substituted silanetriol. Voronkov *et al.* studied the hydrolysis of several 1-alkyl, 1-alkoxy, and 1-aryloxysilatranes [43-45] discovering that an acid catalyst significantly increases the rate of hydrolysis.

$$N(CH_2CH_2O)_3Si{-}R + 3H_2O \rightarrow N(CH_2CH_2OH)_3 + R{-}Si(OH)_3 \qquad (1)$$

The neutral hydrolysis is described by a first-order rate equation [42]. Voronkov *et al.* observed that the rate of hydrolysis increases as the electronegativity of the substituent group in the 1-position increases. Using ultraviolet spectroscopy to monitor the n→σ* absorption in the 200-220-nm region of the hydrolysis product tri(2-hydroxyalkyl)amine, Voronkov *et al.* proposed a mechanism for the neutral hydrolysis involving nucleophilic attack at the silicon center by a water molecule, forming a four-center intermediate and subsequent slow opening of the silatrane ring due to cleavage of an endocyclic siloxane bond (Si-O), Eq. (2) [45]. In 1-aryloxysilatranes, depending on steric accessibility, hydrolytic cleavage is reported to occur at the axial siloxane bond (Si-OC) [46].

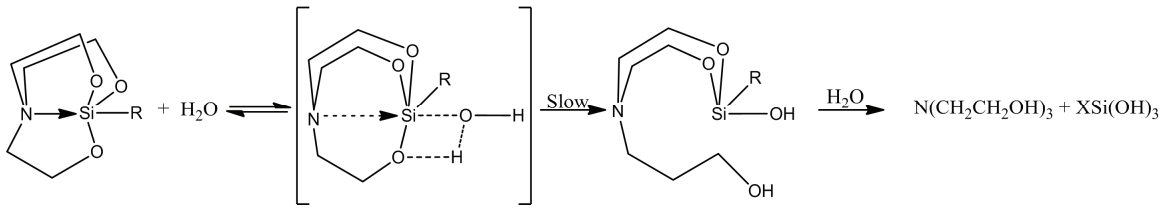

(2)

In an acid catalysis, the rate of hydrolysis of 1-substituted silatranes increases and follows second-order kinetics [42,44,47]. Voronkov *et al.* proposed that the rate determining step involves protonation of the "reaction center" with simultaneous transfer of water to the silicon atom and subsequent "very fast" cleavage of the endocyclic siloxane bond (Si-O) [42,44]. Apparently, the rate of this protonation step decreases as the electronegativity of the substituent group –R at the 1-position increases.

Many theoretical investigations offer insight into the hydrolytic stability of 1-substituted silatranes. Comparisons of structures from gas-phase calculations and experimentally obtained X-ray crystal and gas-phase electron diffraction determine that the transannular Si-N distance increases going from the crystal to the gas phase, suggesting that intermediate values might be expected in solution [5,57-62,74]. Studies focused on the nature of the Si-N bond in 1-substituted silatranes conclude that a 3-center-4-electron (3c-4e) bonding model [63] offers the best description of the transannular interaction between Si and N, highlighting the importance of the substituent group in the axial position [60,64-66].

Several studies report an equally important impact of the equatorial groups on the Si-N transannular interaction in 1-substituted silatranes [5,61,67-69]. As a result, Zabalov *et al.* proposed a different bonding model for silatranes [70]. The silatrane bonding model of Zabalov *et. al* augments the 3c-4e bonding model to consider the molecular orbitals of the equatorial substituents and accounts for the cooperativity effects observed. More specifically, the mutual effect of substituent groups (axial and equatorial) is determined by the strength of the interaction with the silicon center [64]. Weakening the interaction between one substituent group with silicon will result in a stronger interaction between other substituent groups and silicon. The ability to adapt to changes around the silicon center may play a role in the hydrolytic stability of 1-substituted silatranes and contribute to the "cage effect" [61].

Theoretical studies of the hydrolysis reaction of 1-substituted silatranes are very limited. Prieto *et al.* investigated the neutral hydrolysis mechanism of 1-triethanolaminosilatrane, using semi-empirical and molecular mechanics methods, determining that the first step in the hydrolysis mechanism involves cleavage of the apical (axial) siloxane bond (Si-OR) [71]. The findings of Prieto *et al.* are specific to large alkoxy substituents and different axial groups were not considered. Chernyshev *et al.* calculated the potential energy barrier to the hydrolysis of 1-hydroxysilatrane in the gas phase to be 21.2 kcal/mol using the Hartree-Fock (HF) method; however, solvent effects were not considered [72]. The presence of an additional water molecule can significantly alter the energetics of reaction mechanisms involving proton transfer [77,78]. The acid-catalyzed hydrolysis process was not considered in the theoretical studies of Prieto *et al.* and Chernyshev *et al*.

Despite the large number of biological and non-biological applications that are dependent on hydrolytic stability, the mechanism for neutral and acid-catalyzed hydrolysis of 1-substituted silatranes has not been the subject of many *ab initio* mechanistic studies. For a complex system still under investigation [76], like silatrane, interpretation of kinetic data is difficult and may yield several plausible explanations for the stability of 1-substituted silatranes [43,47]. A reliable theoretical analysis of stationary points along reaction pathways obtained from *ab initio* calculations may help elucidate the pronounced hydrolytic

stability of 1-substituted silatranes and the role of acid catalysis in the rate enhancement of the hydrolysis.

In the current paper, the hydrolysis mechanism of 1-substituted silatranes is studied using *ab initio* electron correlation methods. Substituent groups at the 1-position studied in this work include R = H, Cl, F, CH_3, NH_2, OH, PH_2, and SiH_3. The effect of an acid catalyst and the presence of an additional water molecule (water-assisted) on the hydrolysis mechanism is considered. Solvent effects are approximated with appropriate single-point calculations. The predicted reaction mechanism and barriers to hydrolysis are discussed and compared with experimental observations.

The outline of this paper is as follows. Section 2 describes the computational methods used to predict the hydrolysis mechanism of 1-substituted silatranes and discusses the approach taken for the mechanistic study of acid-catalyzed and water-assisted hydrolysis. Section 3 summarizes the results of the current study. Concluding remarks are given in the last section.

2. Computational Methods

Møller Plesset second-order perturbation theory (MP2) [79-81] and the 6-31G(d) basis set was used for all stationary-point calculations [82-85], denoted as MP2/6-31G(d). First-order saddle-point (transition state) searches were performed using the quadratic approximation method of Culot *et al.* [86]. Reactants, intermediates and products were characterized by a positive definite Hessian matrix (second derivative matrix of the energy with respect to nuclear coordinates). Transition state structures were characterized by a single negative value in the Hessian matrix. Intrinsic reaction coordinate (IRC) calculations [87] with the Gonzalez-Schlegel second-order algorithm and a step size of 0.05 $(amu)^{1/2}$ bohr were used to link transition state structures with corresponding reactants and products [88,89]. Partial atomic charges were calculated using the geodesic electrostatic potential derived charge method of Spackman [90]. More accurate relative energies were obtained by conducting single-point calculations using the completely renormalized left eigenvalue coupled cluster (CR-CC(2,3)) method of Piecuch *et al.* [91,92] and the 6-31G(d) basis set at

all MP2/6-31G(d) stationary point geometries, denoted CR-CC(2,3)//MP2/6-31G(d). Core orbitals were frozen for all MP2 and CR-CC(2,3) calculations.

Single-point aqueous calculations using the conductor-like polarizable continuum model (CPCM) [93] [94] with an iterative solver on all MP2/6-31G(d) stationary point structures were performed to model solvent effects, denoted MP2-CPCM//MP2/6-31G(d). For comparison, fully-optimized aqueous solvation calculations using MP2 with CPCM and the 6-31G(d) basis set were carried out for the neutral hydrolysis of 1-methylsilatrane with one water molecule, denoted MP2-CPCM/6-31G(d). In the fully optimized aqueous solvation calculations, stationary point structures and reaction pathways are obtained using CPCM. This is in contrast to the single-point aqueous calculations in which the stationary-point structures and reaction pathways are obtained in the gas phase (without CPCM).

The acid-catalyzed hydrolysis of 1-substituted silatranes is modeled by protonating an equatorial oxygen. The endocyclic oxygen (O_a) opposite a hydrolyzing water coordination site is protonated to allow unhindered proton transfer from the hydrolyzing water molecule to a neighboring siloxane bond (Si-O_c). The basal nitrogen is not protonated, because proton affinity studies, by Yoshikawa *et al.* [68], show that O-protonation is favored, concomitant with an increase in the transannular Si-N interaction (decrease in transannular Si-N distance). Evidence for equatorial protonation is provided by experimental studies on the acid-catalyzed hydrolysis of 1-hydroazasilatrane by Woning *et al.* [49]. The latter X-ray crystallographic analysis of a cationic 1-hydroazasilatrane species, show an increase in the equatorial bond distance between the atom bearing the catalytic proton and silicon, demonstrating an equatorially protonated structure. Nuclear magnetic resonance studies by Cerveau *et al.* [50] and Garant *et al.* [48] also show the propensity for equatorial protonation in 1-substituted silatranes.

Due to the increased complexity, both computationally and mechanistically, study of the addition of an extra water molecule in the hydrolysis reaction mechanism is limited to the neutral and acid-catalyzed hydrolysis of the unsubstituted 1-hydrosilatrane. Additional calculations are performed on the neutral water-assisted hydrolysis of 1-methylsilatrane, for comparisons with experimental values.

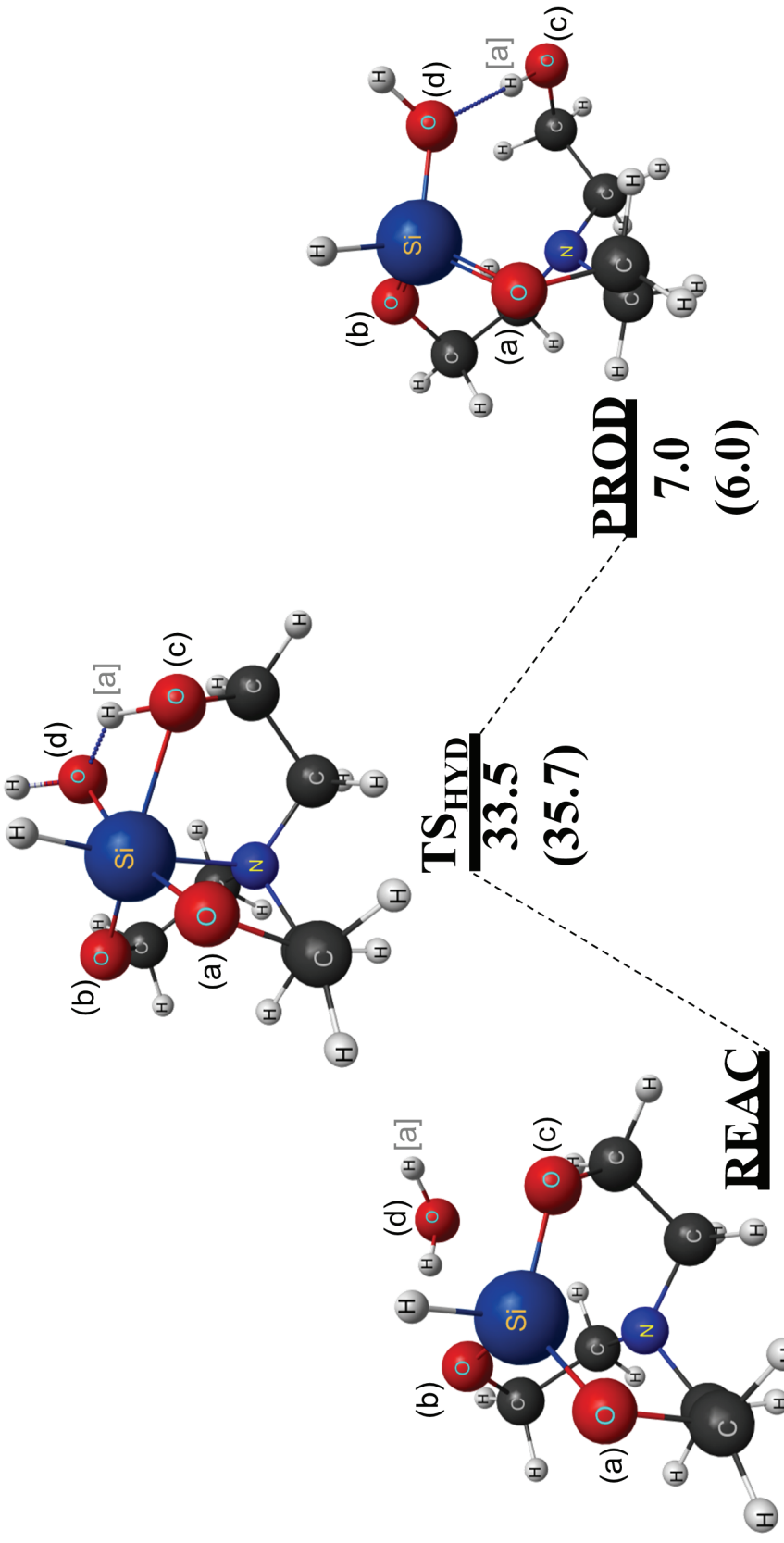

Figure 2. Reaction pathway for the neutral hydrolysis of 1-hydrosilatrane involving a four-center transition state with one water molecule. MP2/6-31G(d) energies (kcal/mol) are shown. CR-CC(2,3)//MP2/6-31G(d) values are given in parentheses. The four-center "4C-" prefix is implied in the labeling of the stationary points throughout the mechanism.

All calculations were performed using the General Atomic and Molecular Electronic Structure System (GAMESS) quantum chemistry code [95] and visualized using MacMolPlt [96].

3. Results and Discussions

References to reaction pathways, mechanisms, reactants, transition states, and intermediates for hydrolysis processes involving one water molecule and proceeding through a four-center transition state are prefixed with "4C-". Similarly, reaction pathways, mechanisms, stationary points involving two water molecules and proceeding through a six-center transition state are prefixed with "6C-".

Hydrolysis

Eq. (1) summarizes the hydrolysis of 1-substituted silatranes. Hydrolysis products, tri-(2-hydroxyalkyl)amine and Si-substituted silanetriol, are generated in three steps by successive addition of water to the silatrane framework. The initial step in the mechanism is discussed next.

Neutral hydrolysis proceeding through a four-center transition state

Reaction pathway

The MP2/6-31G(d) reaction pathway for 1-hydrosilatrane, Figure 2, is qualitatively representative of the four-center (4C-) single-step mechanism for the neutral hydrolysis of 1-substituted silatranes. Starting from a reactant (4C-REAC), the neutral hydrolysis mechanism proceeds through a barrier associated with formation of a four-center transition state (4C-TS_{HYD}) that connects the 1-substituted silatrane and a nucleophilic hydrolyzing water molecule with the hydrolysis product (4C-PROD). At the transition state, proton H_a transfers from the hydrolyzing water molecule to a neighboring endocyclic oxygen (O_c) and cleavage of the siloxane bond (Si-O_c) is observed in the generation of 4C-PROD. The MP2/6-31G(d) reaction pathway is consistent with the mechanism proposed by the Voronkov *et al.* UV spectroscopy studies [45]. The Voronkov *et al.* mechanism involves formation of a four-center transition state with "synchronous or subsequent" opening of the silatrane framework.

Figure 3. Intramolecular hydrogen bonding in the transition states for the hydrolysis of 1-substituted silatranes.

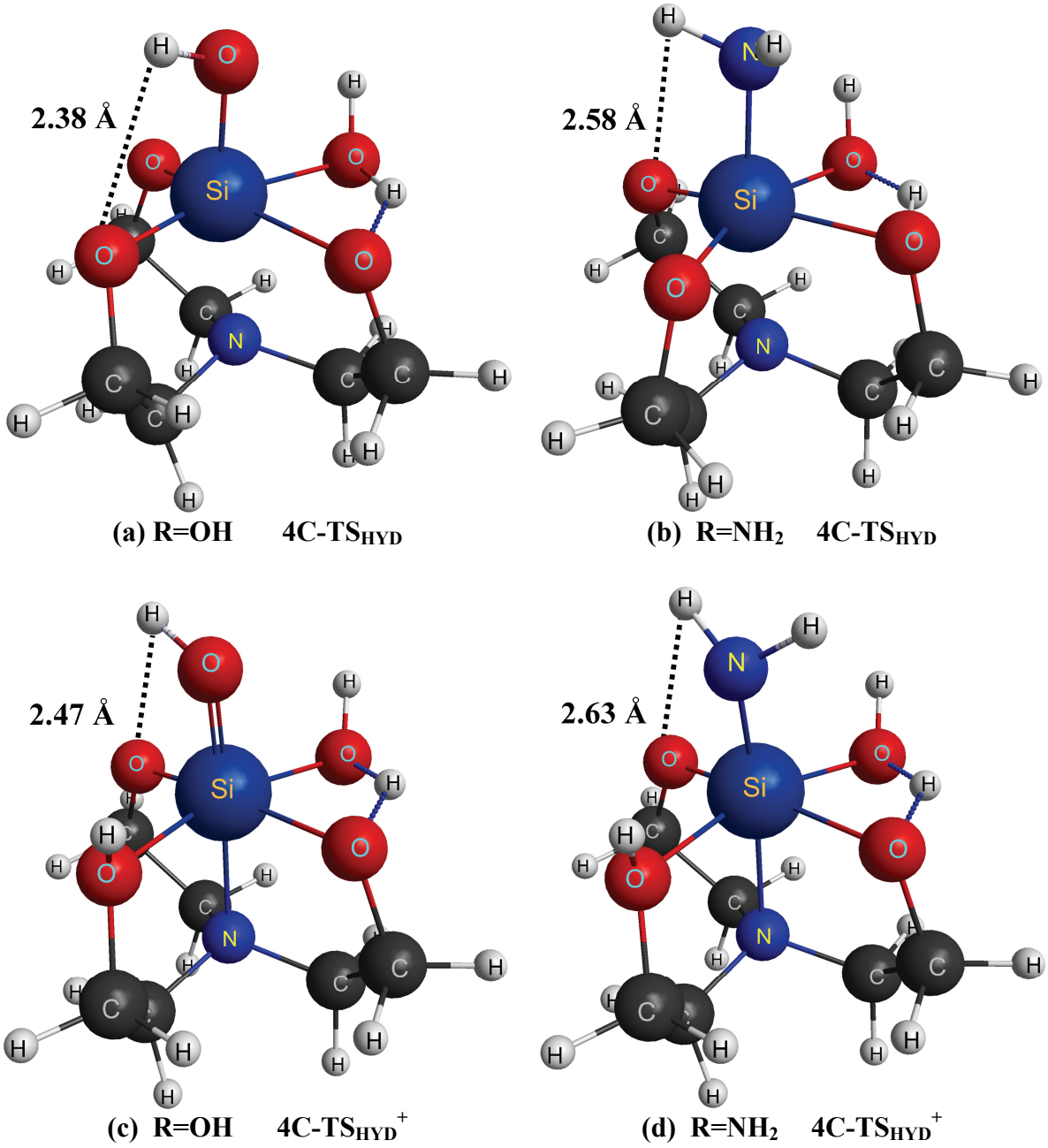

Energetics

The calculated barrier heights and relative energies between products and reactants, $\Delta E_{reaction}$, for the neutral hydrolysis of 1-substituted silatranes proceeding through a four-center transition state are summarized in the top part of Table 1. The $\Delta E_{reaction}$ energies in Table 1 indicate that the neutral hydrolysis reaction is mildly endothermic, ≈ 0.5-7 kcal/mol, and proceeds through a large barrier, ≈ 22-35 kcal/mol. The CR-CC(2,3)//MP2/6-31G(d) barrier heights are slightly, < 3 kcal/mol, higher than the MP2 values for all 1-substituted silatranes. The MP2 and CR-CC(2,3) endothermicities of the neutral hydrolysis reaction agree to within 0.5 kcal/mol. The predicted barrier heights largely decrease as the electronegativity of the substituent group at the 1-position increases. Although 1-fluorosilatrane does not seem to follow this trend, the reason may be that NH_2 and OH can stabilize their corresponding transition states by intramolecular hydrogen bonding (Figures 3a and 3b). Aside from intramolecular hydrogen bonding, the observed trend with substituent electronegativity is expected for a mechanism involving nucleophilic displacement, because the positive charge on silicon (reaction center) increases when attached to increasingly electronegative axial groups. Intramolecular hydrogen bonding of the substituent group with the silatrane framework is likely to account for the deviations in the $\Delta E^{\ddagger}(4C\text{-}TS_{HYD})$ trend with 1-hydro and 1-amino silatrane.

Table 1. MP2/6-31G(d) calculated energetics (kcal/mol) for the hydrolysis of 1-substituted silatranes. CR-CC(2,3)//MP2/6-31G(d) values are given in parentheses. MP2-CPCM//MP2/6-31G(d) single-point aqueous solvation calculations are shown in square brackets. Barriers are calculated as the difference in stationary-point total electronic energy.

		Neutral								
	-R	$\Delta E^{\ddagger}(TS_{HYD})$			$\Delta E^{\ddagger}(TS_{POST})$			$\Delta E_{reaction}$		
Four-center (4C-)										
	H	33.5	(35.7)	[32.8]				7.0	(6.0)	[10.3]
	Cl	33.4	(35.8)	[32.9]				7.3	(6.8)	[9.3]
	F	31.9	(34.2)	[31.3]				6.9	(6.5)	[8.6]
	CH_3	35.0	(37.2)	[34.7]				5.9	(4.7)	[7.9]
	CH_3[a]			[35.4]						[9.1]
	NH_2	25.7	(27.9)	[25.6]				2.3	(2.1)	[4.2]
	OH	21.7	(24.3)	[21.7]				0.3	(0.3)	[2.1]
	PH_2	34.5	(36.7)	[34.3]				7.5	(6.1)	[10.6]
	SiH_3	34.3	(36.5)	[34.7]				7.7	(6.2)	[10.2]
Six-center (6C-)										
	H	28.8	(32.2)	[28.1]	20.6	(20.8)	[21.1]	10.0	(9.7)	[13.0]
	CH_3	30.9	(34.3)	[30.8]	21.9	(22.1)	[22.5]	4.7	(3.8)	[8.1]
							[23.1]			
	CH_3[b]			[31.2]						[14.8]
		Acid-catalyzed								
	-R	$\Delta E^{\ddagger}(TS_{PRE}^{+})$			$\Delta E^{\ddagger}(TS_{HYD}^{+})$			$\Delta E_{reaction}^{+}$		
Four-center (4C-)										
	H	1.3	(1.3)	[1.7]	18.9	(21.2)	[19.6]	9.4	(9.1)	[11.3]	5.3	(5.2)	[6.7]
	Cl	0.8	(0.8)	[1.0]	19.1	(21.5)	[19.7]	7.8	(7.5)	[10.1]	3.7	(3.5)	[5.7]
	F	1.0	(1.0)	[1.2]	17.2	(19.4)	[18.1]	6.8	(6.6)	[9.2]	2.5	(2.3)	[4.5]
	CH_3				20.6	(22.8)	[21.3]	7.7	(7.5)	[9.9]	4.1	(3.9)	[9.1]
	CH_3[a]			[4.3]			[22.7]			[11.3]			[9.5]
	NH_2	5.5	(5.3)	[5.5]	15.9	(18.1)	[15.7]	12.4	(12.0)	[13.6]	11.9	(11.5)	[12.9]
	OH	0.2	(0.1)	[0.2]	8.3	(10.6)	[9.1]	5.9	(5.6)	[6.4]	-2.9	(-3.1)	[-0.6]
	PH_2	0.5	(0.7)	[1.6]	20.3	(22.6)	[20.7]	6.3	(6.0)	[6.1]	6.0	(6.2)	[8.3]
	SiH_3				20.6	(22.8)	[21.7]	6.6	(6.5)	[8.0]	5.6	(5.3)	[7.1]
Six-center (6C-)										
	H	1.4	(1.3)	[1.7]	1.6	(4.1)	[3.0]	5.4	(5.4)	[10.1]	2.3	(3.0)	[7.6]

[a] Fully-optimized aqueous solvation, see Section 2

Figure 4. Transition state for the hydrolysis of 1-substituted silatranes.

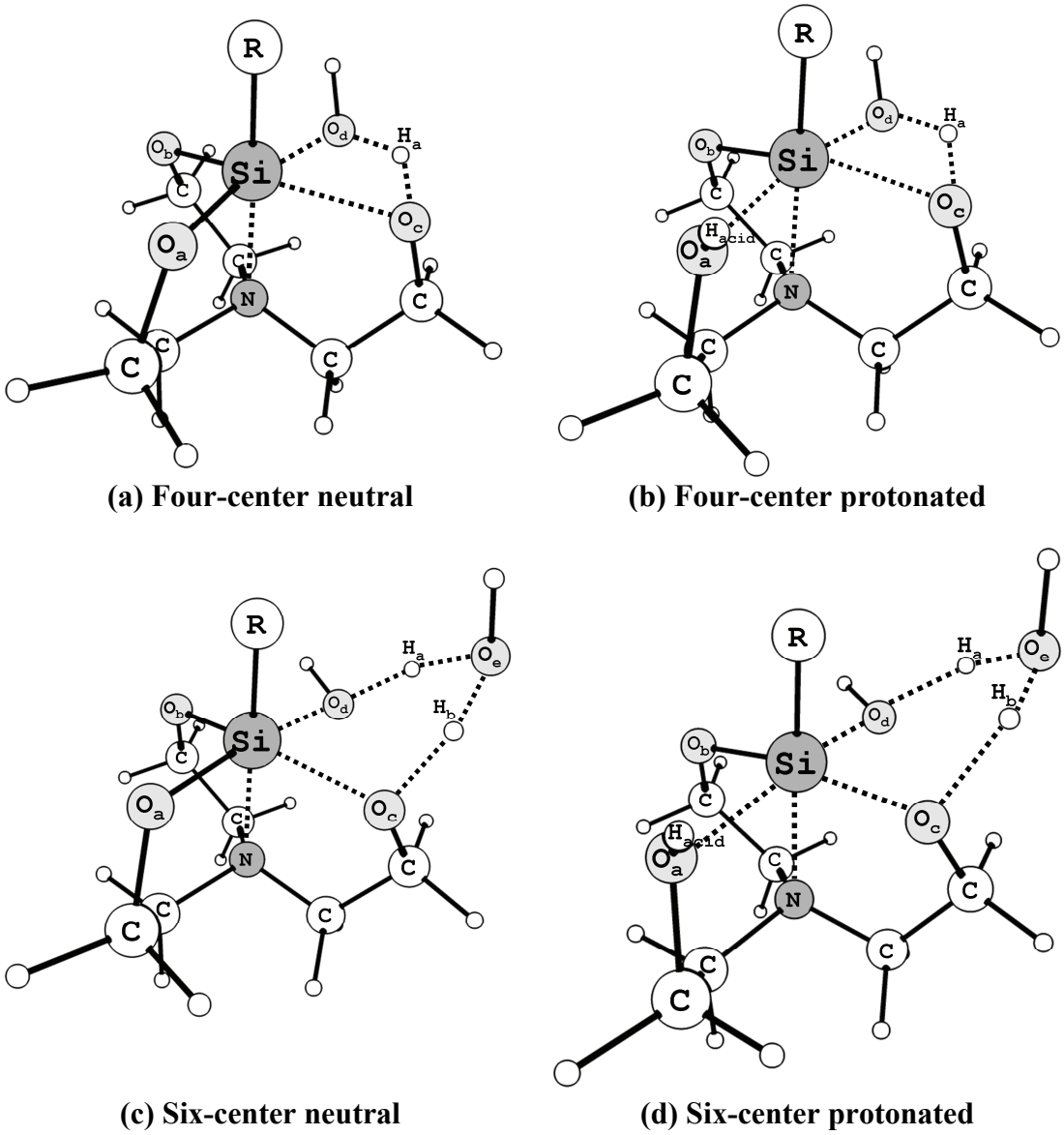

(a) Four-center neutral **(b) Four-center protonated**

(c) Six-center neutral **(d) Six-center protonated**

Geometric parameters

The geometric parameters for 4C-TS_{HYD}, Figure 4a, are listed in Table 2. The MP2/6-31G(d) calculated transition state structure shows formation of a siloxane bond (Si-O_d) with the hydrolyzing water molecule and concerted proton transfer (H_a) from the hydrolyzing water (O_d-H_a) to a neighboring endocyclic oxygen (O_c-H_a). Lengthening of the water-protonated siloxane bond distance (Si-O_c) suggests that cleavage of the silatrane ring

occurs at 4C-TS_{HYD}. MP2/6-31G(d) calculated transannular Si-N distances at the transition state range from 2.04-2.10 Å and are shorter than those reported in previous theoretical studies on 1-substituted silatranes [66,68,73,74].

Table 2. MP2/6-31G(d) calculated geometric parameters (angstroms) for the hydrolysis of 1-substituted silatranes proceeding through a four-center transition state involving one water molecule.

	Neutral – 4C-TS_{HYD} Distances							
-R	Si-N	Si-R	Si-O_a	Si-O_b	Si-O_c	Si-O_d	O_c-H_a	O_d-H_a
H	2.058	1.485	1.725	1.733	2.035	2.002	1.187	1.244
Cl	2.043	2.110	1.715	1.727	1.999	1.968	1.201	1.236
F	2.037	1.641	1.713	1.725	1.998	1.961	1.194	1.244
CH_3	2.078	1.888	1.732	1.736	2.055	2.020	1.189	1.238
CH_3[a]	2.043	1.896	1.746	1.741	2.060	1.992	1.195	1.235
NH_2	2.071	1.765	1.743	1.728	2.005	1.957	1.170	1.273
OH	2.094	1.693	1.732	1.726	2.032	1.929	1.245	1.202
PH_2	2.054	2.284	1.731	1.735	2.045	1.995	1.178	1.254
SiH_3	2.060	2.353	1.735	1.738	2.048	2.019	1.192	1.235
	Acid-catalyzed – 4C-TS_{HYD}^+ Distances							
-R	Si-N	Si-R	Si-O_a	Si-O_b	Si-O_c	Si-O_d	O_c-H_a	O_d-H_a
H	2.056	1.876	2.056	1.695	1.931	1.883	1.238	1.226
Cl	2.029	2.080	1.965	1.687	1.902	1.858	1.235	1.239
F	2.015	1.631	1.943	1.683	1.896	1.846	1.236	1.241
CH_3	2.036	1.476	2.019	1.690	1.918	1.868	1.237	1.231
NH_2	2.050	1.738	1.981	1.688	1.925	1.876	1.229	1.237
OH	2.023	1.676	1.975	1.690	1.900	1.861	1.241	1.232
PH_2	2.039	2.266	2.063	1.696	1.932	1.878	1.224	1.243
SiH_3	2.047	2.353	2.134	1.699	1.938	1.891	1.241	1.221

[a]Aqueous solvated geometric parameters obtained at the MP2-CPCM/6-31G(d) level of theory.

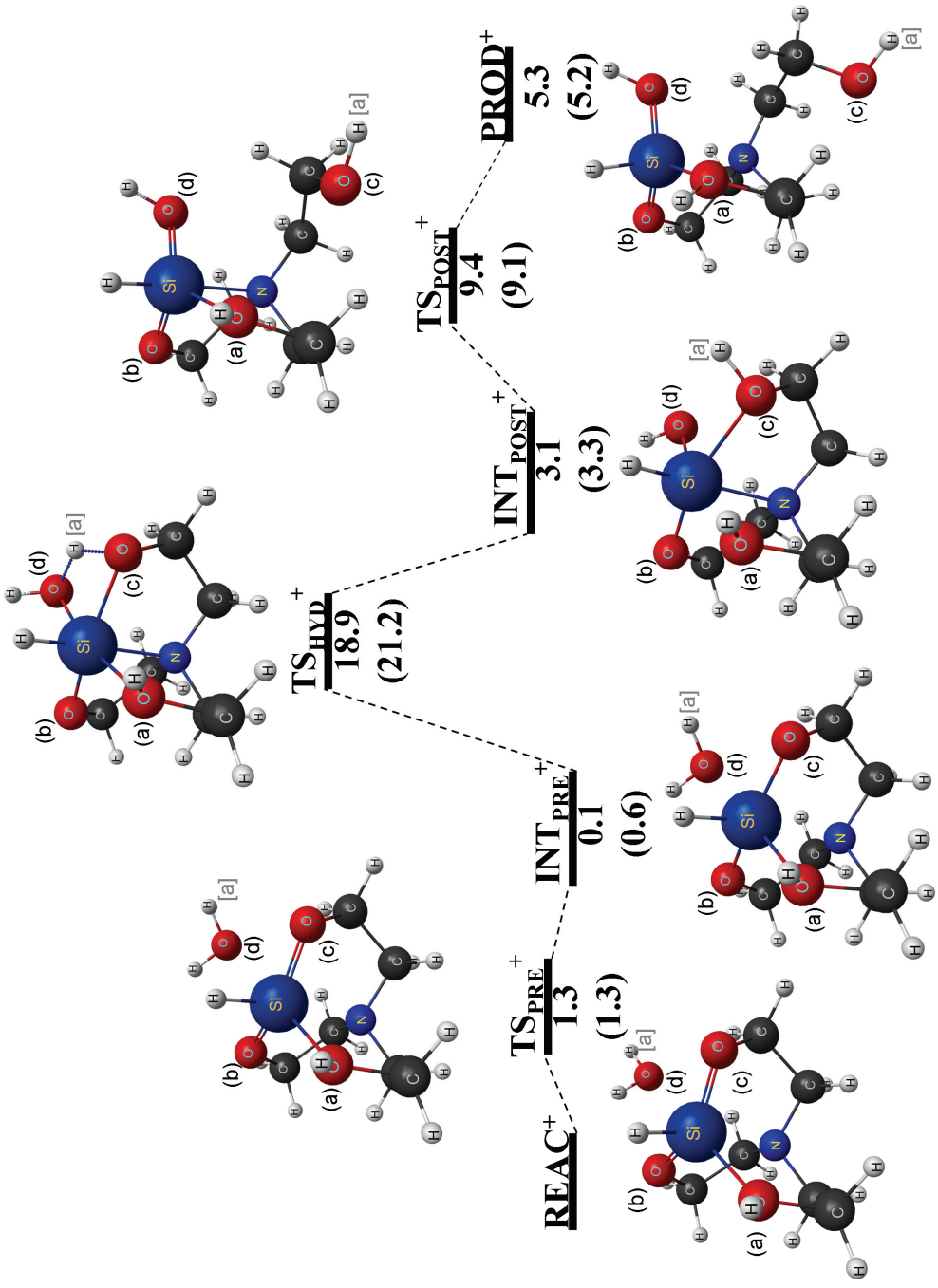

Figure 5. Reaction pathway for the acid-catalyzed hydrolysis of 1-hydrosilatrane involving a four-center transition state with one water molecule. MP2/6-31G(d) energies (kcal/mol) are relative to reactant ($REAC^+$). CR-CC(2,3)//MP2/6-31G(d) values are given in parentheses. The four-center "4C-" prefix is implied in the labeling of the stationary points throughout the mechanism.

Comparisons

In comparison to previous theoretical studies, the barrier to neutral hydrolysis for 1-hydroxysilatrane predicted by both MP2/6-31G(d) (21.7 kcal/mol) and CR-CC(2,3)//MP2/6-31G(d) (24.3 kcal/mol) agree to within ≈ 3 kcal/mol of the HF/6-31G(d) calculations of Chernyshev *et al.* [72], 21.2 kcal/mol. It appears that the only experimental activation energy available in the literature for neutral hydrolysis, of a 1-substituted silatrane species investigated in the current study, is for 1-methylsilatrane [51], 12.1 kcal/mol. The MP2/6-31G(d) and CR-CC(2,3)//MP2/6-31G(d) gas-phase activation energies for the neutral hydrolysis of 1-methylsilatrane, 35.0 kcal/mol and 37.2 kcal/mol, respectively, are much larger than the experimental value. However, the experiments were conducted in aqueous solvent, so the results are not directly comparable. This is discussed further below. Nonetheless, the calculated results are in qualitative agreement with the experimental reports that the neutral hydrolysis of 1-substituted silatranes is not kinetically favored and is unlikely to proceed in the absence of a catalyst [42-49,52-55].

Acid-catalyzed hydrolysis proceeding through a four-center transition state

Reaction pathway

As a representative example of the acid-catalyzed hydrolysis of 1-substituted silatranes, the MP2/6-31G(d) reaction pathway for 1-hydrosilatrane is shown in Figure 5. Unlike the single-step neutral hydrolysis mechanism, the acid-catalyzed hydrolysis of 1-substituted silatranes consists of a multi-step mechanism starting with a catalytically protonated reactant (4C-REAC^{+}).

Step one in the acid-catalyzed hydrolysis mechanism is formation of a stable silatrane-water complex. A pre-hydrolysis transition state (4C-TS_{PRE}^{+}) associated with step one rearranges the silatrane framework simultaneously with the approach of a nucleophilic hydrolyzing water molecule towards the silicon center. A pre-hydrolysis intermediate (4C-INT_{PRE}^{+}), produced in step one, shows a hexacoordinated silatrane-water complex. Step one is absent for 1-methyl and 1-silyl silatrane; instead, the acid-catalyzed mechanism proceeds

directly from 4C-REAC$^+$ towards formation of a four-center transition state, as in step two, summarized in the next paragraph.

Step two in the acid-catalyzed hydrolysis mechanism transfers the hydrolyzing water molecule to the silatrane framework and forms a four-center transition state (Si-O_d-H_a-O_c). The step two transition state (4C-TS_{HYD}^+) is the acid-catalyzed equivalent of the four-center transition state in the neutral hydrolysis mechanism, 4C-TS_{HYD}. Step two generates a post-hydrolysis intermediate (4C-INT_{POST}^+) in which a hydroxyl group, from the hydrolyzing water molecule, is covalently bonded to the silicon (Si-O_d), and complete proton transfer from the hydrolyzing water (H_a) to a neighboring endocyclic oxygen (O_c) has occurred. In contrast to the neutral hydrolysis mechanism, where ring cleavage occurs simultaneously with formation of 4C-TS_{HYD}, in the acid-catalyzed mechanism the ring with the water-protonated siloxane bond (Si-O_c) remains attached to the silatrane framework following the formation of 4C-TS_{HYD}^+. A separate barrier is encountered for the cleavage of the silatrane ring in the acid-catalyzed hydrolysis.

Step three in the acid-catalyzed hydrolysis mechanism of 1-substituted silatranes is cleavage of the water-protonated siloxane bond (Si-O_c) and departure of the resulting hydroxyalkyl linkage. The post-hydrolysis transition state (4C-TS_{POST}^+) displaces the cleaved silatrane ring and has a repulsive alignment of the oxygen lone pairs between the hydroxyalkyl linkage (O_c) and an endocyclic oxygen (O_a) separated by 3 Å. The final hydrolysis product (4C-$PROD^+$) displaces the hydroxyalkyl linkage from the silicon center.

Energetics

The calculated barrier heights and relative energies for the acid-catalyzed hydrolysis of 1-substituted silatranes proceeding through a four-center transition state are listed in Table 1. The largest barriers associated with the acid-catalyzed hydrolysis mechanism are, in descending order, formation of the four-center transition state, $\Delta E^{\ddagger}$(4C-TS_{HYD}^+); cleavage of the ring, $\Delta E^{\ddagger}$(4C-TS_{POST}^+); and complexation with water, $\Delta E^{\ddagger}$(4C-TS_{PRE}^+). MP2/6-31G(d) barrier heights involving formation of 4C-TS_{HYD}^+, ≈ 8-21 kcal/mol, continue to trend inversely with the axial group electronegativity, with 1-methylsilatrane possessing the largest barrier. Similar to the neutral hydrolysis mechanism, intramolecular hydrogen bonding

within the silatrane framework is likely to stabilize 4C-TS_{HYD}^{+} in the acid-catalyzed hydrolysis mechanism causing 1-hydroxy and 1-amino silatrane to deviate from the trend (Figures 3c and 3d). The MP2/6-31G(d) barriers at 4C-TS_{HYD}^{+} for the acid-catalyzed hydrolysis are smaller than the barriers in the neutral hydrolysis by ≈ 10-15 kcal/mol. Except for 1-aminosilatrane, a decrease in the MP2/6-31G(d) net reaction energy, 4C-$\Delta E_{reaction}^{+}$, in the acid-catalyzed hydrolysis mechanism is predicted to be smaller than that for the neutral hydrolysis mechanism. The increase in 4C-$\Delta E_{reaction}^{+}$ for 1-aminosilatrane is likely caused by an unfavorable arrangement in which the proton on the catalytically protonated endocyclic oxygen (O_a) is directed away from the hydroxyalkyl oxygen lone pair (O_c). The interatomic distance between the two oxygen atoms (O_cO_a) in the neutral and acid-catalyzed hydrolysis product of 1-aminosilatrane is 3.49 Å and 2.83 Å, respectively. The decrease in oxygen-oxygen interatomic distance increases the electron repulsion, raises the energy of the hydrolysis product and likely causes the increase of 4C-$\Delta E_{reaction}^{+}$ for the acid-catalyzed hydrolysis of 1-aminosilatrane. For 1-hydroxysilatrane, MP2/6-31G(d) predicts that the acid-catalyzed hydrolysis is exothermic, possibly caused by an increased stabilization due to intramolecular hydrogen-bonding. The CR-CC(2,3)//MP2/6-31G(d) calculated values for 4C-$\Delta E_{reaction}^{+}$ and $\Delta E^{\ddagger}$(4C-TS_{HYD}^{+}) are within 0.5 and 3 kcal/mol of the MP2/6-31G(d) values, respectively. Both levels of theory, MP2/6-31G(d) and CR-CC(2,3)//MP2/6-31G(d), predict formation of 4C-TS_{HYD}^{+} to be the rate-limiting step (largest barrier) in the acid-catalyzed hydrolysis of 1-substituted silatranes.

Geometric parameters

The MP2/6-31G(d) calculated geometric parameters for 4C-TS_{HYD}^{+}, Figure 4b, associated with the rate-determining step in the acid-catalyzed hydrolysis of 1-substituted silatranes are listed in Table 2. Catalytic protonation shows significant structural differences between the cationic, 4C-TS_{HYD}^{+}, and neutral, 4C-TS_{HYD}, transition states. Most notable is the increase in the siloxane bond distance bearing the catalytic proton (Si-O_a) and the concomitant decrease in the neighboring siloxane bond lengths (Si-O_b and Si-O_c) and transannular Si-N distance. Structural changes in the 4C-TS_{HYD}^{+} siloxane bond lengths and transannular Si-N distance are in line with the proton-affinity studies of Yoshikawa *et al.*

[68] and attributed to cooperativity effects [64,70]. Similar to 4C-TS_{HYD} in the neutral hydrolysis mechanism, the calculated transition state structure for 4C-TS_{HYD}^{+} in the acid-catalyzed mechanism shows the formation of a siloxane bond (Si-O_d) with a nucleophilic hydrolyzing water molecule and concerted proton transfer from the hydrolyzing water molecule (H_a) to an endocyclic oxygen (O_c). However, the siloxane bond lengths involving the water-protonated endocyclic oxygen (Si-O_c) in 4C-TS_{HYD}^{+} are shorter when compared with 4C-TS_{HYD}. The shorter siloxane bond lengths calculated for the acid-catalyzed hydrolysis suggest that cleavage of the silatrane ring at the water-protonated siloxane bond (Si-O_c) at 4C-TS_{HYD}^{+}, is not as advanced at this stage of the mechanism as predicted for the neutral hydrolysis mechanism.

Comparisons

In comparison with the neutral hydrolysis of 1-substituted silatranes, an acid catalyst manifestly alters the hydrolysis reaction mechanism. Predicted for all 1-substituted silatranes is the introduction of a separate step (4C-INT_{POST}^{+} → 4C-TS_{POST}^{+} → 4C-$PROD^{+}$) for ring cleavage involving the water-protonated siloxane bond (Si-O_c). Separation of ring cleavage from the rate-limiting step reduces the net barrier in the acid-catalyzed hydrolysis by ≈ 10-15 kcal/mol relative to the neutral hydrolysis rate-limiting barrier.

Although experimental activation energies for the acid-catalyzed hydrolysis of the systems studied in the current work have not been reported in the literature, qualitative assessments of the theoretical calculations can still be made. The MP2/6-31G(d) and CR-CC(2,3)//MP2/6-31G(d) gas-phase calculations predict a decrease in the barrier associated with the rate-limiting step in the hydrolysis of 1-substituted silatranes when an acid catalyst is used, $| \Delta E^{\ddagger}(\text{4C-TS}_{HYD}^{+}) - \Delta E^{\ddagger}(\text{4C-TS}_{HYD}) | \approx$ 10-15 kcal/mol. The reduced barrier heights suggest that the rate of acid-catalyzed hydrolysis is much faster than that for neutral hydrolysis and is consistent with experimental observations [42,44,47,52]. Furthermore, both the MP2/6-31G(d) and CR-CC(2,3)//MP2/6-31G(d) relative barrier heights, listed in Table 1, for the rate-limiting step, $\Delta E^{\ddagger}(\text{4C-TS}_{HYD}^{+})$, and ring cleavage, $\Delta E^{\ddagger}(\text{4C-TS}_{POST}^{+})$, support the proposed mechanism by Voronkov *et al.* [42], in which the rate-limiting step in

the acid-catalyzed hydrolysis process is followed by "very fast" cleavage of an endocyclic siloxane bond, $\Delta E^{\ddagger}(4C\text{-}TS_{POST}^{+}) < \Delta E^{\ddagger}(4C\text{-}TS_{HYD}^{+})$.

The agreement between the calculated reaction pathways and experimental reaction mechanisms does not preclude the existence of lower energy pathways that may be important to the overall dynamics of the chemical reaction. It has been reported that the presence of additional water molecules can have stabilizing effects on reactions involving the transfer of a proton (or hydrogen atom), *e.g.*, aqueous solvolysis [77,78]. The theoretical mechanistic studies of Kudo and Gordon on hydrolysis and condensation processes of silsesquioxanes suggest a significant decrease, ≈ 15-20 kcal/mol, in the barrier to hydrolysis by adding an extra water molecule, serving as a proton shuttle, to the reaction mechanism [77]. A decrease of similar magnitude would bring the gas-phase calculated values for the activation energy of the neutral hydrolysis of 1-methylsilatrane within range of the experimental observations.

Water-assisted hydrolysis

Water-assisted neutral hydrolysis proceeding through a six-center transition state

Reaction pathway

The MP2/6-31G(d) reaction pathway for the water-assisted six-center (6C-) neutral hydrolysis of 1-hydrosilatrane is shown in Figure 6. A similar reaction pathway is obtained for 1-methylsilatrane. MP2/6-31G(d) calculations predict a multi-step mechanism for 6C-neutral hydrolysis. The first and rate-determining step in the hydrolysis mechanism involves the formation of a six-center ($Si\text{-}O_d\text{-}H_a\text{-}O_e\text{-}H_b\text{-}O_c$) transition state ($6C\text{-}TS_{HYD}$) involving silatrane and two water molecules. $6C\text{-}TS_{HYD}$ depicts a siloxane bond formation ($Si\text{-}O_d$) simultaneous with protonation of an endocyclic oxygen (O_c), assisted by an additional water molecule serving as a proton shuttle. The post-hydrolysis intermediate ($6C\text{-}INT_{POST}$) generated following the formation of $6C\text{-}TS_{HYD}$ shows the additional water molecule hydrogen-bonding with the oxygen of the newly formed siloxane bond ($Si\text{-}O_d$) and the cleaved hydroxyalkyl linkage ($O_c\text{-}H_b$).

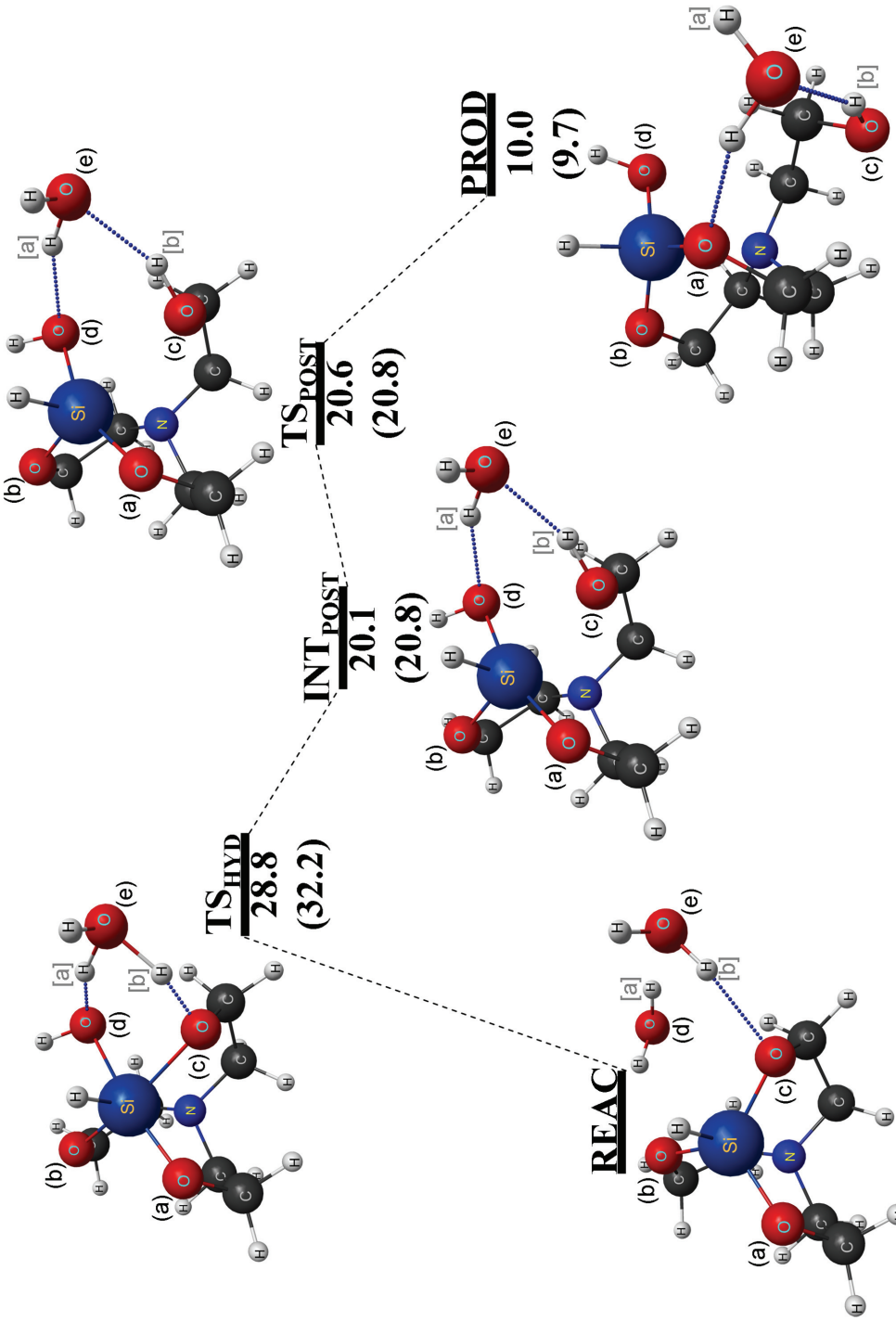

Figure 6. Reaction pathway for the neutral hydrolysis of 1-hydrosilatrane involving a six-center transition state with two water molecules. MP2/6-31G(d) energies (kcal/mol) are relative to reactant (REAC). CR-CC(2,3)//MP2/6-31G(d) values are given in parentheses. The six-center "6C-" prefix is implied in the labeling of the stationary points throughout the mechanism.

The second step involves displacement of the leaving group, hydroxyalkyl linkage. The post-hydrolysis transition state (6C-TS_{POST}) is nearly isoenergetic with the post-hydrolysis intermediate (6C-INT_{POST}), and as a result, the structures are similar. CR-CC(2,3)//MP2/6-31G(d) predicts the energies of 6C-INT_{POST} and 6C-TS_{POST} to be isoenergetic, indicating the absence of an additional barrier for 1-hydrosilatrane. Similar results (not shown) were obtained for the 6C-neutral hydrolysis of 1-methylsilatrane. The MP2/6-31G(d) energy difference between 6C-TS_{POST} and 6C-INT_{POST} in 1-methylsilatrane is 0.1 kcal/mol and the single point CR-CC(2,3)//MP2/6-31G(d) calculation predicts a negative energy difference, -0.2 kcal/mol, indicating no barrier. The higher-quality CR-CC(2,3)//MP2/6-31G(d) calculations bring into question the existence of a second barrier, and the existence of a distinct second mechanism step. Nevertheless, the final product in the 6C-neutral hydrolysis mechanism (6C-PROD) is similar to the 4C-neutral hydrolysis product 4C-PROD (Figure 2) and shows the hydroxyalkyl linkage to be far removed from the silicon center. The additional water molecule continues to participate in hydrogen bonding with the hydroxyalkyl linkage and silatrane framework in forming the hydrolysis product.

Energetics

Table 1 summarizes the effect of the additional water on the energetics of 6C-neutral hydrolysis of 1-hydrosilatrane. The presence of an extra water molecule reduces the MP2/6-31G(d) and CR-CC(2,3)//MP2/6-31G(d) barriers for formation of 6C-TS_{HYD} in the 6C-neutral hydrolysis of 1-hydrosilatrane by 4.7 kcal/mol and 3.5 kcal/mol, respectively, compared with the 4C-TS_{HYD} formation barrier. For 1-methylsilatrane, formation of 6C-TS_{HYD} is lowered by 4.1 kcal/mol and 2.9 kcal/mol for MP2/6-31G(d) and CR-CC(2,3)//MP2/6-31G(d) calculations, respectively, compared with the barrier associated with 4C-TS_{HYD}. For both MP2/6-31G(d) and CR-CC(2,3)//MP2/6-31G(d), the endothermicity of the 6C-neutral hydrolysis reaction, 6C-$\Delta E_{reaction}$, decreases by approximately 1.0 kcal/mol for 1-methylsilatrane and increases by ≈ 4.0 kcal/mol for 1-hydrosilatrane when compared with the respective 4C-$\Delta E_{reaction}$. The calculated changes in the 6C-$\Delta E_{reaction}$ are likely due to the hydrogen-bonding ability of the extra water in stabilizing the reactant, 6C-REAC, and product, 6C-PROD, as well as the expected stability of a six-center transition state compared

with a four-center transition state. Both levels of theory, MP2/6-31G(d) and CR-CC(2,3)//MP2/6-31G(d), predict that the formation of the six-center transition state 6C-TS_{HYD} is the rate-determining step in the 6C-neutral hydrolysis mechanism.

Geometric parameters

The MP2/6-31G(d) calculated geometric parameters for 6C-TS_{HYD}, Figure 4c, associated with the rate-determining step in the 6C-neutral hydrolysis of 1-hydrosilatrane are listed in Table 3. Notable 6C-TS_{HYD} structure changes are decreases in the siloxane bond lengths with the water-protonated endocyclic oxygen, Si-O_c = 1.934 Å, and hydrolyzing water, Si-O_d = 1.949 Å, compared with 4C-TS_{HYD}, Si-O_c = 2.035 Å and Si-O_d = 2.002 Å, respectively. The changes in the siloxane bond distances are likely due to the additional water molecule serving as a proton shuttle. Protonation of the endocyclic oxygen (O_c) should result in a weaker, longer siloxane bond (Si-O_c); however, the oxygen-hydrogen bond distance is discernibly longer in 6C-TS_{HYD}, O_c-H_b = 1.244 Å, when compared with 4C-TS_{HYD}, O_c-H_a = 1.187 Å, and is suggestive of delayed protonation. Aside from the six-center transition state and the aforementioned decrease in the siloxane bond distances, the geometric parameters for 6C-TS_{HYD} and 4C-TS_{HYD} differ by less than 0.03 Å and as a result, their structures are very similar.

Comparisons

In contrast to the 4C-neutral hydrolysis process, an additional water molecule stabilizes the transition state associated with the rate-determining step in the 6C-neutral hydrolysis, 6C-TS_{HYD}. The calculated decrease in the activation energies from the 4C-neutral hydrolysis to the 6C-neutral hydrolysis (water-assisted) are modest, ≈ 3.5-5.0 kcal/mol for 1-hydrosilatrane and ≈ 3.0-4.0 kcal/mol for 1-methylsilatrane. These reductions in barrier heights may be compared to the changes reported by Kudo and Gordon, in which the barrier to water-assisted hydrolysis of silsesquioxanes decrease by ~10-15 kcal/mol [77]. The presence of a second step predicted by MP2/6-31G(d) may be linked to the delayed protonation of the endocyclic oxygen (O_c). Delaying protonation of the endocyclic oxygen of the leaving group would in turn delay the process of ring cleavage. Considering the

decreased activation energy calculated for the 4C-acid-catalyzed hydrolysis of 1-substituted silatranes, where separation of the ring cleavage step from the rate-limiting step reduces the barrier to hydrolysis by 10-15 kcal/mol, delayed protonation may be the early stages of decoupling the protonation of the endocyclic oxygen from the rate-determining step in the neutral hydrolysis process. Complete decoupling of protonation from the rate-determining step may require the addition of more water molecules to the reaction mechanism.

Although the calculated barrier heights for the rate-determining step in the neutral hydrolysis of 1-substituted silatranes is reduced in the presence of an additional water molecule, the computed values are still considerably higher than the experimental value. The calculated results continue to highlight the pronounced hydrolytic stability of 1-substituted silatranes. Despite the addition of a second water molecule, the neutral hydrolysis of 1-substituted silatranes is not kinetically favored and unlikely to proceed without use of a catalyst.

Water-assisted acid-catalyzed hydrolysis proceeding through a six-center transition state

Reaction pathway

The MP2/6-31G(d) reaction pathway for the water-assisted (6C-)acid-catalyzed hydrolysis of 1-hydrosilatrane is shown in Figure 7. Similar to the 4C-acid-catalyzed hydrolysis, the 6C-acid-catalyzed hydrolysis consists of a multi-step mechanism starting from a catalytically protonated reactant (6C-REAC^{+}).

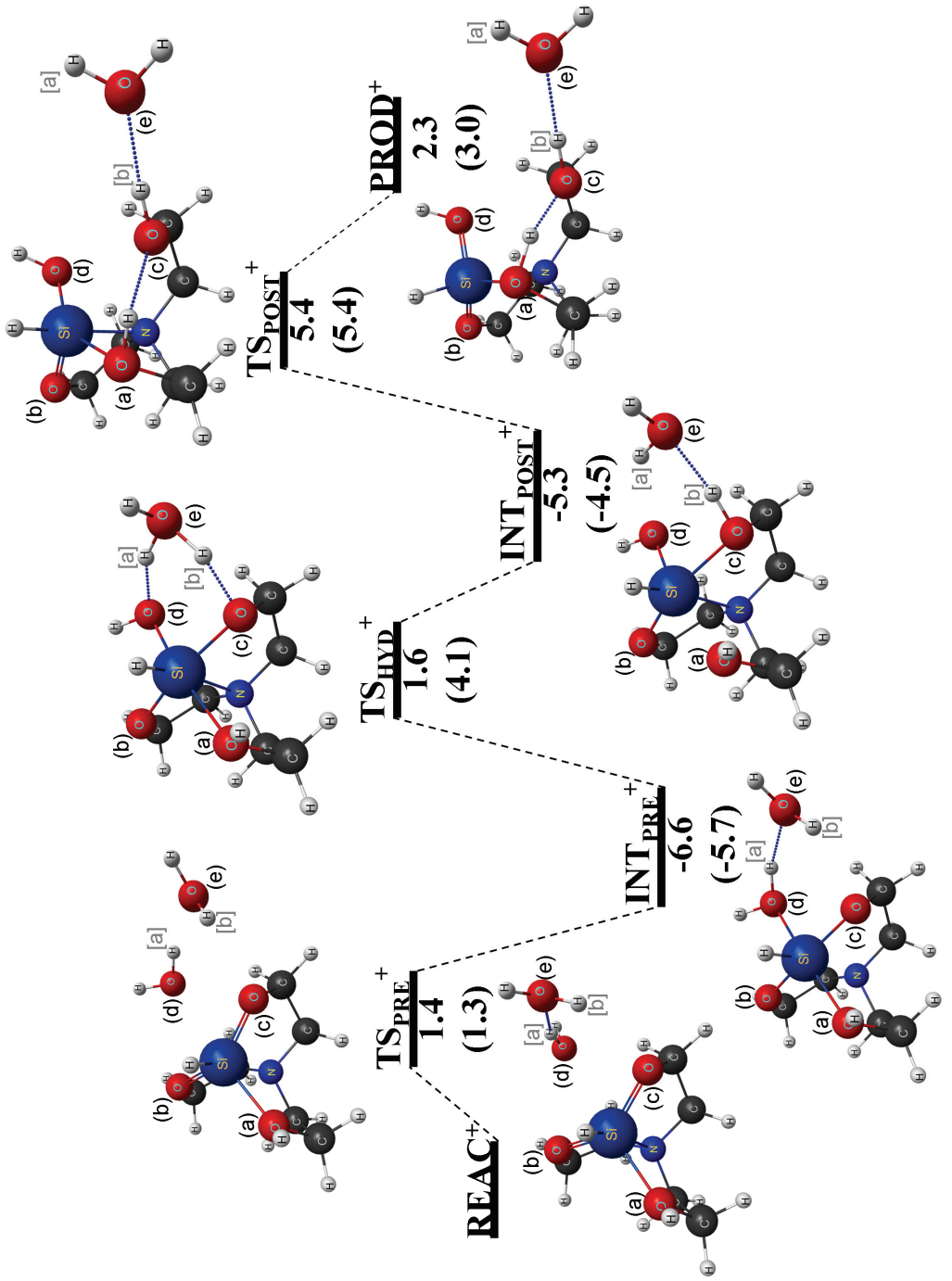

Figure 7. Reaction pathway for the acid-catalyzed hydrolysis of 1-hydrosilatrane involving a six-center transition state with two water molecules. MP2/6-31G(d) energies (kcal/mol) are relative to reactant ($REAC^+$). CR-CC(2,3)//MP2/6-31G(d) values are given in parentheses. The six-center "6C-" prefix is implied in the labeling of the stationary points throughout the mechanism.

Step one of the 6C-acid-catalyzed hydrolysis mechanism is the formation of a hexacoordinated silatrane- water complex. A pre-hydrolysis transition state (6C-TS_{PRE}^{+}) associated with the first step in the 6C-acid-catalyzed hydrolysis mechanism rearranges the silatrane framework simultaneously with the approach of a nucleophilic hydrolyzing water molecule, similar to the 4C-acid-catalyzed hydrolysis. In contrast with the 4C-acid-catalyzed hydrolysis, a pre-hydrolysis intermediate (6C-INT_{PRE}^{+}) in the 6C-acid-catalyzed hydrolysis has the nucleophilic hydrolyzing water molecule bonded to the silatrane framework (Si-O_d). In the hexacoordinated 6C-INT_{PRE}^{+} an additional water molecule participates in hydrogen-bonding with the hydrolyzing water molecule ($O_e \cdots H_a$).

Step two of the 6C-acid-catalyzed hydrolysis mechanism entails protonation of an endocyclic oxygen (O_c). The step two six-center transition state (6C-TS_{HYD}^{+}) involves proton-shuttling from the hydrolyzing water to the endocyclic oxygen, assisted by the additional water molecule. A post-hydrolysis intermediate (6C-INT_{POST}^{+}) generated in step two shows a deprotonated water molecule bonded to the silatrane framework (Si-O_d) and a water-protonated endocyclic oxygen (O_c-H_b). In contrast to 6C-INT_{POST} in the 6C-neutral hydrolysis, a siloxane bond bearing the water-protonated endocyclic oxygen (Si-O_c) is not cleaved in the intermediate 6C-INT_{POST}^{+} in the 6C-acid-catalyzed hydrolysis mechanism.

Step three of the 6C-acid-catalyzed hydrolysis mechanism comprises cleavage of the water-protonated siloxane bond (Si-O_c) and displacement of a resulting hydroxyalkyl linkage. The post-hydrolysis transition state (6C-TS_{POST}^{+}) contains a hydroxyalkyl linkage, resulting from cleavage of the water-protonated siloxane bond, displaced from the silicon center, Si-$O_c \approx 2.90$ Å. At 6C-TS_{POST}^{+}, the hydroxyalkyl linkage participates in hydrogen bonding with the catalytic proton and the additional water molecule. A final hydrolysis product (6C-$PROD^{+}$) in the 6C-acid-catalyzed hydrolysis mechanism further displaces the hydroxyalkyl linkage from the silicon center, Si-$O_c \approx 3.47$ Å.

Energetics

The calculated barrier heights and relative energies for the 6C-acid-catalyzed hydrolysis mechanism of 1-hydrosilatrane are summarized in Table 1. Use of an acid

catalyst significantly alters the energetics. In comparison with the 6C-neutral hydrolysis mechanism, catalytic protonation reduces the barrier associated with the hydrolysis step by ≈ 27 kcal/mol. Consequently, the rate-limiting step in the 6C-acid-catalyzed hydrolysis mechanism is not the formation of the six-center transition state 6C-TS_{HYD}^{+}. The MP2/6-31G(d) barrier height for 6C-TS_{HYD}^{+}, 1.6 kcal/mol, is nearly isoenergetic with the barrier height associated with the rearrangement of the silatrane framework, 6C-TS_{PRE}^{+}, 1.4 kcal/mol (See Fig. 6). The two corresponding CR-CC(2,3)//MP2/6-31G(d) barrier heights are 1.3 kcal/mol for 6C-TS_{HYD}^{+} and 4.1 kcal/mol for 6C-TS_{PRE}^{+}. The largest barrier in the 6C-acid-catalyzed hydrolysis mechanism (5.4 kcal/mol) occurs in the third step, the formation of 6C-TS_{POST}^{+}. The endothermicity of the water-assisted acid-catalyzed hydrolysis of 1-hydrosilatrane is lower compared with the neutral counterpart, $|\ 6C\text{-}\Delta E_{reaction} - 6C\text{-}\Delta E_{reaction}^{+}\ |$ ≈ 7 kcal/mol.

Geometric parameters

Table 3 lists the MP2/6-31G(d) geometric parameters for all stationary points on the reaction pathway in the 6C-acid-catalyzed hydrolysis of 1-hydrosilatrane. 6C-TS_{POST}^{+} involves cleavage of the water-protonated siloxane bond (Si-O_c), whose distance increases by ≈ 1 Å from 1.975 Å in the intermediate 6C-INT_{POST}^{+} to 2.898 Å in 6C-TS_{POST}^{+}.

Notable structural differences in 6C-TS_{HYD}^{+} compared with 6C-TS_{HYD} are in bond distances involving the hydrolyzing water molecule, Si-O_d, and the water-protonated endocyclic oxygen, Si-O_c and O_c-H_b. The siloxane bond distance of the hydrolyzing water molecule is shorter in 6C-TS_{HYD}^{+}, Si-O_d = 1.804 Å, compared with 6C-TS_{HYD}, Si-O_d = 1.949 Å, suggestive of a stronger siloxane bond in the 6C-acid-catalyzed hydrolysis mechanism. The siloxane bond length of the water-protonated endocyclic oxygen is also shorter in 6C-TS_{HYD}^{+}, Si-O_c = 1.837 Å, compared with 6C-TS_{HYD}, Si-O_c = 1.934 Å, indicative of impeded ring cleavage in the 6C-acid-catalyzed hydrolysis mechanism. The hydroxyl bond distance of the water-protonated endocyclic oxygen is longer in 6C-TS_{HYD}^{+}, O_c-H_b = 1.444 Å, compared with 6C-TS_{HYD}, O_c-H_b = 1.244 Å, suggesting delayed protonation of the hydroxyalkyl linkage.

Table 3. MP2/6-31G(d) calculated geometric parameters (angstroms) for the hydrolysis of 1-hydrosilatrane.

Four-center (4C-)

		Distances							
	IRC Point	Si-N	Si-R	Si-O_a	Si-O_b	Si-O_c	Si-O_d	O_c-H_a	O_d-H_a
Neutral	REAC	2.231	1.482	1.699	1.719	1.699	3.660	3.213	0.971
	TS_{HYD}	2.058	1.485	1.725	1.733	2.035	2.002	1.187	1.244
	PROD	2.925	1.483	1.663	1.665	4.080	1.683	0.979	1.822
Acid-catalyzed	$REAC^+$	2.091	1.475	1.953	1.667	1.664	3.527	4.119	0.972
	TS_{PRE}^+	2.109	1.475	1.959	1.673	1.675	2.790	3.027	0.973
	INT_{PRE}^+	2.123	1.476	1.993	1.698	1.706	2.149	2.604	0.978
	TS_{HYD}^+	2.036	1.476	2.019	1.690	1.918	1.868	1.237	1.231
	INT_{POST}^+	2.035	1.477	2.166	1.689	2.081	1.705	0.982	2.596
	TS_{POST}^+	2.058	1.485	1.925	1.665	3.693	1.672	0.974	4.186
	$PROD^+$	2.071	1.487	1.914	1.665	4.514	1.667	0.974	5.114

Six-center (6C-)

		Distances									
	IRC Point	Si-N	Si-R	Si-O_a	Si-O_b	Si-O_c	Si-O_d	O_c-H_b	O_d-H_a	O_e-H_a	O_e-H_b
Neutral	REAC	2.193	1.485	1.698	1.711	1.716	3.695	1.894	0.981	1.948	0.981
	TS_{HYD}	2.079	1.493	1.741	1.758	1.934	1.949	1.244	1.285	1.168	1.205
	INT_{POST}	2.103	1.495	1.740	1.743	2.170	1.811	1.004	1.783	0.995	1.714
	TS_{POST}	2.133	1.496	1.719	1.725	2.496	1.781	0.993	1.817	0.990	1.783
	PROD	2.171	1.499	1.715	1.696	4.173	1.699	0.983	4.448	0.970	1.869
Acid-catalyzed	$REAC^+$	2.068	1.477	1.953	1.656	1.678	3.805	2.155	0.983	1.843	0.974
	TS_{PRE}^+	2.070	1.476	1.957	1.660	1.679	3.279	2.134	0.983	1.839	0.973
	INT_{PRE}^+	2.081	1.481	2.026	1.710	1.742	1.967	2.107	1.019	1.613	0.979
	TS_{HYD}^+	2.051	1.487	2.097	1.710	1.837	1.804	1.444	1.459	1.076	1.086
	INT_{POST}^+	2.047	1.479	2.150	1.699	1.975	1.730	1.026	2.067	0.981	1.586
	TS_{POST}^+	2.023	1.480	2.040	1.668	2.898	1.682	0.992	4.830	0.971	1.747
	$PROD^+$	2.176	1.480	1.880	1.666	3.469	1.672	0.998	4.972	0.972	1.704

Comparisons

The 6C-acid-catalyzed hydrolysis mechanism decreases the barrier associated with the rate-determining step relative to the corresponding neutral hydrolysis mechanism. The 6C-acid-catalyzed hydrolysis mechanism barrier heights are significantly reduced compared with the 6C-neutral hydrolysis mechanism, by ≈ 27 kcal/mol. So, the catalysis causes a 90% reduction in the barrier height. A decrease in the activation energy for the rate-determining step due to the addition of a water molecule suggests that protonation of the endocyclic

oxygen is delayed, by inclusion of the extra proton shuttle, nearly decoupling the protonation and ring cleavage. Consequently, protonation is no longer part of the rate determining step in 6C-TS_{POST}^{+}. The largest barrier in the 6C-acid-catalyzed hydrolysis of 1-hydrosilatrane is predicted by both MP2/6-31G(d) and CR-CC(2,3)//MP2/6-31G(d) to be 5.4 kcal/mol suggesting that the predicted reaction mechanism is kinetically favorable.

Experimental observations reported by Voronkov *et al.* [42] propose that the rate limiting step of the acid-catalyzed hydrolysis involves transfer of water to the silatrane framework followed by "very fast" ring cleavage. The largest barrier in the 6C-acid-catalyzed hydrolysis of 1-hydrosilatrane involves cleavage of the water-protonated siloxane bond (silatrane ring), in contrast to the conclusions that were inferred from the experiments. However, the presence of an additional hydrolyzing water (required for complete hydrolysis) could alter the reaction mechanism, and preferentially lower the barrier at 6C-TS_{POST}^{+}.

Solvent effects

The calculations in the previous sections, all relate to the gas phase, with at most one extra water molecule. Solvents can potentially significantly change barrier heights or even mechanisms of complex reactions. The effect of solvent on the reaction mechanisms for the hydrolysis of 1-substituted silatranes is now considered.

Table 1 summarizes the results of aqueous bulk solvent on barrier heights and relative energies in the various reaction mechanisms discussed above for the hydrolysis of 1-substituted silatranes. As demonstrated in the table, aqueous solvation, as described by the continuum PCM solvent, does not significantly alter the gas phase calculations reported above. The identity of the rate-limiting steps is unchanged from the gas phase and the relative energies between the hydrolysis product and the reactants are not changed significantly. The small deviations from the gas phase values are likely due to enhanced stabilization of the reactants caused by a larger dipole moment in the reactants than the products. Because of the importance of hydrogen bonding in aqueous solvation, the bulk continuum solvent treatment may not capture all of the important solvent-induced modifications of the reaction mechanisms.

To evaluate the accuracy of aqueous single-point calculations on stationary points obtained from gas-phase reaction pathway calculations, fully-optimized aqueous solvation calculations at the MP2-CPCM/6-31G(d) level of theory were performed for 4C-neutral, 6C-neutral and 4C-acid-catalyzed hydrolysis of 1-methylsilatrane. Table 1 contains the fully-optimized aqueous solvation calculations. With the exception of the relative energy between hydrolysis product and reactant for the 6C-neutral hydrolysis of 1-methylsilatrane, MP2-CPCM//MP2/6-31G(d) and MP2-CPCM/6-31G(d) calculations agree to within ≈ 1.4 kcal/mol. The change in endothermicity of the 6C-neutral hydrolysis of 1-methylsilatrane is due to a slightly different geometry obtained with fully-optimized aqueous solvation calculations for the hydrolysis product. In addition, the MP2-CPCM/6-31G(d) calculations predict the existence of an additional barrier, TS_{PRE}^{+}, in the 4C-acid-catalyzed hydrolysis of 1-methylsilatrane but does not change the identity of the rate-limiting step.

The MP2-CPCM//MP2/6-31G(d) calculated activation energies for the 4C- and 6C-neutral hydrolysis of 1-methylsilatrane are 34.4 kcal/mol and 30.8 kcal/mol, respectively. More sophisticated solvent models that allow addition of explicit water molecules may be required to quantitatively reproduce the experimental activation energy for the neutral hydrolysis of 1-methylsilatrane.

Neutral vs. acid-catalyzed hydrolysis

The separation of ring cleavage from the transfer of the water to the silatrane framework is best understood in terms of cooperativity effects [70]. To augment structural analysis based on bond distances and to assist in understanding acid catalysis, MP2/6-31G(d) calculated bond orders for hydrolysis of 1-hydrosilatrane are listed in Table 4. For similar bonds within a set of related molecules at a given level of theory, qualitatively analyzing bond orders provides insight about the bonding in a system [97].

In the 4C- and 6C- acid-catalyzed hydrolysis of 1-hydrosilatrane, ring cleavage involving the water-protonated siloxane bond (Si-O_c) is separated from transfer of the water molecule to the silatrane framework, and is likely to account for the decrease in the barrier heights at 4C- and 6C- TS_{HYD}^{+}. Specifically, at 4C- and 6C- TS_{HYD}^{+} the weakening (decrease in bond order) of the siloxane bond (Si-O_a) due to the catalytic proton is mitigated

by strengthening (increase in bond order) of the neighboring siloxane bonds (Si-O_b, Si-O_c), allowing bond formation with the hydrolyzing water molecule (Si-O_d) to occur without simultaneous or subsequent cleavage of the water-protonated siloxane bond (Si-O_c).

In the 4C-acid-catalyzed hydrolysis of 1-hydrosilatrane, cleavage of the water-protonated ring occurs at INT_{POST}^+ or between INT_{POST}^+ and formation of TS_{POST}^+. Bond order analysis of 4C-acid-catalyzed hydrolysis of 1-hydrosilatrane suggests that ring cleavage involves the breaking of a silanol group (Si-O_cH_b) via a weakened siloxane bond [98]. A similar analysis is deduced for neutral and acid-catalyzed 6C- hydrolysis mechanisms. The assessments are the same: ring cleavage for 6C-neutral hydrolysis suggests bond breaking of a siloxane group, whereas, ring cleavage for 6C-acid-catalyzed hydrolysis is likely to involve bond breaking of a silanol group.

The MP2/6-31G(d) charge on the silicon atom, derived from the electrostatic potential (Table 4), offers additional insight on the hydrolysis mechanism of 1-hydrosilatrane. In 4C-neutral hydrolysis of 1-hydrosilatrane the charge on the silicon center decreases, Δq_{Si} = -0.12 e, going from 4C-REAC to formation of 4C-PROD. The decrease in positive charge on the silicon center is unlikely to favor nucleophilic attack and hydrolysis of additional units of water. Nucleophilic attack is not hindered in 6C-neutral hydrolysis because the charge on the silicon center is not affected by formation of 6C-PROD from 6C-REAC, Δq_{Si} = -0.01 e. Acid catalysis moves in the opposite direction, with nucleophilic attack being promoted for both 4C- and 6C- hydrolysis. 4C-acid-catalyzed hydrolysis of 1-hydrosilatrane increases the positive charge on the silicon center going from 4C-$REAC^+$ to 4C-$PROD^+$, Δq_{Si} = +0.06 e. A larger increase in positive charge, Δq_{Si} = +0.16 e, on the silicon center is observed, upon going from 6C-$REAC^+$ to 6C-$PROD^+$ in 6C-acid-catalyzed hydrolysis. The increase in positive charge on the silicon center in 4C- and 6C- acid-catalyzed hydrolysis of 1-hydrosilatrane favors the hydrolysis of additional units of water via nucleophilic displacement following formation of hydrolysis products and may add to the enhancement of the rate of acid-catalyzed hydrolysis.

Table 4. MP2/6-31G(d) calculated bond orders and geodesic potential derived charge (electron) on silicon for the hydrolysis of 1-hydrosilatrane. CR-CC(2,3)//MP2/6-31G(d) values are given in parentheses. Only bond order values over 0.05 are shown.

			Four-center (4C-) Bond Orders									
	IRC Point	Charge Si	Si-N	Si-R	Si-O_a	Si-O_b	Si-O_c	Si-O_d	O_c-H_a	O_d-H_a	O_a-H_{acid}	
Neutral	REAC	0.85	0.263	0.924	0.915	0.815	0.911			0.749		
	TS_{HYD}	1.02	0.376	0.908	0.865	0.812	0.416	0.420	0.363	0.338		
	PROD	0.73	0.073	0.906	0.980	0.986		0.902	0.623	0.070		
Acid-catalyzed	$REAC^+$	0.41	0.397	0.919	0.367	0.994	1.045			0.731	0.659	
	TS_{PRE}^+	0.44	0.375	0.922	0.357	0.968	0.995	0.124		0.724	0.661	
	INT_{PRE}^+	0.51	0.365	0.915	0.335	0.916	0.909	0.258		0.690	0.668	
	TS_{HYD}^+	0.58	0.432	0.907	0.312	0.936	0.546	0.549	0.335	0.337	0.670	
	INT_{POST}^+	0.57	0.431	0.899	0.231	0.926	0.292	0.898	0.672		0.686	
	TS_{POST}^+	0.50	0.434	0.899	0.391	1.021		1.004	0.714		0.662	
	$PROD^+$	0.47	0.425	0.900	0.401	1.037		1.024	0.714	0.687	0.660	

			Six-center (6C-) Bond Orders										
	IRC Point	Charge Si	Si-N	Si-R	Si-O_a	Si-O_b	Si-O_c	Si-O_d	O_c-H_b	O_d-H_a	O_e-H_a	O_e-H_b	O_a-H_{acid}
Neutral	REAC	0.77	0.290	0.923	0.923	0.855	0.825		0.077	0.662	0.092	0.628	
	TS_{HYD}	0.94	0.351	0.906	0.851	0.769	0.440	0.428	0.313	0.305	0.377	0.357	
	INT_{POST}	0.95	0.333	0.900	0.852	0.786	0.248	0.620	0.558	0.126	0.600	0.155	
	TS_{POST}	0.93	0.321	0.901	0.891	0.826	0.148	0.666	0.590	0.116	0.611	0.136	
	PROD	0.76	0.305	0.906	0.817	0.933		0.916	0.631		0.746	0.093	
Acid-catalyzed	$REAC^+$	0.43	0.416	0.918	0.365	1.055	0.971			0.628	0.079	0.680	0.660
	TS_{PRE}^+	0.38	0.408	0.921	0.358	1.027	0.969	0.082		0.629	0.092	0.687	0.661
	INT_{PRE}^+	0.51	0.390	0.913	0.319	0.892	0.794	0.374		0.518	0.151	0.662	0.673
	TS_{HYD}^+	0.57	0.405	0.906	0.279	0.890	0.582	0.613	0.230	0.222	0.448	0.429	0.680
	INT_{POST}^+	0.56	0.414	0.903	0.246	0.904	0.386	0.806	0.503	0.057	0.654	0.158	0.684
	TS_{POST}^+	0.58	0.461	0.901	0.351	0.990	0.090	0.957	0.579		0.720	0.105	0.613
	$PROD^+$	0.59	0.325	0.914	0.504	1.017		0.986	0.558		0.717	0.121	0.438

4. Conclusions

Neutral and acid-catalyzed hydrolysis mechanisms of 1-substituted silatranes (R = H, Cl, F, CH_3, NH_2, OH, PH_2, SiH_3) in the presence of one and two waters were studied at the MP2/6-31G(d) and CR-CC(2,3)//MP2/6-31G(d) level of theory. Catalytic protonation alters the rate-determining step of the reaction mechanism involved with neutral hydrolysis of 1-substituted silatranes by separating concerted events: siloxane bond formation of the hydrolyzing water with the silicon center, proton-transfer from the hydrolyzing water molecule to the endocyclic oxygen of the leaving group, and ring cleavage. The presence of an additional water molecule significantly lowers the energy barriers associated with the acid-catalyzed hydrolysis mechanism by stabilizing transition states and intermediates through hydrogen bonding, proton transfer mediation and ring strain reduction. In addition, atomic charges derived from electrostatic potentials illustrate the conjecture that formation of hydrolysis products during the acid-catalyzed mechanism increases the positive charge on the silicon center, promoting nucleophilic attack of additional waters. Bond order analysis of the hydrolysis mechanism for 1-hydrosilatrane supports the notion that ring cleavage during neutral hydrolysis involves bond breaking of a siloxane group, while ring cleavage during acid-catalyzed hydrolysis is likely to involve bond breaking of a silanol Si-OH bond. Solvent effects do not alter the qualitative findings, suggesting that the insights acquired from theoretical gas-phase calculations may be transferrable to experimental observations. Findings in this study mirror several experimental observations, including the hydrolytic stability of 1-substituted silatranes and enhanced rates of hydrolysis upon the addition of an acid catalyst.

Acknowledgements

This work was supported by funding from the Air Force Office of Scientific Research (AFOSR). MP2 calculations have been performed on CyBlue, an IBM Blue Gene /L supercomputer, located at the Department of Electrical and Computer Engineering Information Infrastructure Institute at Iowa State University in Ames, IA. The authors thank

Dr. Srinivas Aluru for providing the ISU computational resources and Leo C. DeSesso for invaluable assistance in reviewing and editing the manuscript.

References

1. P. Hencsei, L. Bihátsi, I. Kovács, Ö. Wagner, Studies on bioactive organo-silicon compounds, Periodica Polytechnoca Ser. Chem. 35 (1991) 115-121.
2. P. Hencsei, L. Párkányi, The molecular structure of silatranes, Rev. Silicon Germanium, Tin, Lead Compd. 8 (1985) 191-218.
3. C. L. Frye, G. E. Vogel, J. A. Hall, Triptych-siloxazolidines: Pentacoordinate bridgehead silanes resulting from transannular interaction of nitrogen and silicon, J. Am. Chem. Soc. 83 (1961) 996-997.
4. J. W. Turley, F. P. Boer, Structural studies of pentacoordinate silicon. I. Phenyl-(2,2',2''-nitrilotriethoxy)silane, J. Am. Chem. 90 (1968) Soc. 4026-4030.
5. G. I. Csonka, P. Hencsei, Ab initio molecular orbital study of 1-fluorosilatrane, J. Comput. Chem. 15 (1994) 385-394.
6. M. G. Voronkov, I. B. Mazheika, G. I. Zelchan, Atranes. II. Dipole moments and structures of silatranes, Khimiya Geterotsiklicheskikh Soedinenii 1 (1965) 58-63
7. L. Párkányi, L. Bihátsi, P. Hencsei, 1-methylesilatrane, $C_7H_{15}NO_3Si$, Cryst. Struct. Comm. 7 (1978) 435-440.
8. M. G. Voronkov, E. I. Broadskaya, P. Reich, S. G. Shevchenko, V. P. Baryshok, Y. L. Frolov, The influence of intermolecular interactions on the Si-H bond vibration in silatrane and its c-substituents, J. Organomet. Chem. 164 (1979) 35-40.
9. Q. Shen., R. L. Hilderbrandt, The structure of methyl silatrane (1-methyl-2,8,9-trioxa-5-aza-1-silabicyclo(3.3.3)undecane) as determined by gas phase electron diffraction, J. Mol. Struct.: (THEOCHEM) 64 (1980) 257-262.
10. L. Párkányi, P. Hencsei, L. Bihátsi, T. Müller, The molecular structure of 1-fluorosilatrane, J. Organomet. Chem. 269 (1984) 1-9.
11. M. G. Voronokv, V. P. Baryshok, L. P. Petukhov, V. I. Rakhlin, R. G. Mirshov, V. A. Pestunovich, 1-halosilatranes, J. Organomet. Chem. 358 (1988) 39-55.
12. K. Jurkschat, A. Tzscach, M. Dargatz, H. Pepermans, M. Gielen, R. Willem, In situ nucleophilic activation in the propellane 5-chloro-1-aza-5-silatricyclo[3.3.3.$0^{1,5}$]undecane and its hydrolysis in solution, Recueil des Travaux Chimiques des Pays-Bas 107 (1988) 170-174.
13. G. Forgács, M. Kolonits, I. Hargittai, The gas-phase molecular structure of 1-fluorosilatrane from electron diffraction, Struct. Chem. 1 (1990) 245-250.
14. V. Sidorkin, G. K. Balakhchi, Photoelectron spectra and orbital structure of silatranes: Organic derivatives of pentacoordinate silicon, Struct. Chem. 5 (1994) 189-195.
15. S. P. Narula, R. Shankar, M. Kumar, R. K. Chadha, C. Janaik, Structure and reactivity of 1-isothiocyanatosilatrane: The first silatrane with a direct Si-NCS bond, Inorg. Chem. 36 (1997) 1268-1273.
16. B. Trofimov, V. G. Zakrzewski, O. Dolgounitcheva, J. V. Ortiz, V. F. Sidorkin, E. F. Belogolova, M. Belogolov, V. A. Pestunovich, Silicon-nitrogen bonding in silatranes: assignment of photoelectron spectra, J. Am. Chem. Soc. 127 (2005) 986-995.

17. E. A. Ishmaeva, A. P. Timosheva, A. A. Gazizova, D. V. Chachkov, Y. A. Vershchagina, V. E. Kataev, N. V. Timosheva, Dipole moments, structure, and transannular interactions of silatranes containing planar fragments, Zhurnal Obshchei Khimii, 78 (2008) 1114-1117.
18. M. G. Voronokov, Biological activity of silatranes, Top. Curr. Chem. 88 (1979) 77-135.
19. J. H. Greaves, R. Redfern, H. Tinworth, Laboratory tests of 5-p-chlorophenyl silatrane as a rodenticide, J. Hyg. Cambridge 73 (1974) 39-43.
20. D. Rennison, Field tries of the rodenticide 5-p-chlorophenyl silatrane against wild rates(*Rattus norvegicus Berk.*), J. Hyg. Cambridge 73 (1974) 45-48.
21. F. P. Rowe, T. Swinney, A. Bradfield, Field trials of the rodenticide 5-p-chlorophenyl silatrane against wild house mice (*Mus musculus L.*), J. Hyg. Cambridge, 73 (1974) 49-51.
22. M. K. Ticku, R. W. Olsen, Cage convulsants inhibit picrotoxinin binding, Neuropharmacology 18 (1979) 315-318.
23. P. P. Mehta, T. Ramasarama, C. K. R. Kurup, Investigation on the mechanism of the hypocholesterolemic action of 1-ethoxysilatrane, Mol. And Cell. Biochem. 97 (1990) 75-85.
24. V. M. D'yakov, M. G. Voronkov, V. B. Kazimirovskaya, S. V. Loginov, M. M. Rasulov, Wound healing effects of some silocanes and silatranes, in: N. Auner, J. Weis (Eds.), Organosilicon Chemistry VI: For Molecules to Materials, Wiley-VCH Verlag GmbH, Weinheim, Germany, 2008, pp. 588-594.
25. M. G. Voronkov, V. P. Baryshok, Antitumor activity of silatranes, Pharmaceutical Chem. J. 38 (2004) 3-9.
26. M. G. Voronkov, G. Dolmaa, S. Tserenpil, O. Ugtakhbayar, A. Chimidtsogzol, Stimulation of barley seed germination by micromolar aqueous solutions of silatrane and cresacin, Doklady Akademii Nauk 404 (2005) 562-564.
27. V. D'yakov, Organosilicon compounds in medicine and cosmetics, in: Organosilicon Chemistry V: From Molecules to Materials, in: N. Auner, J. Weis (Eds.), Chapter IV. Silicon in Organic and Bioorganic Chemistry, Wiley-VCH Verlag GmbH, Weinheim, Germany, 2008, pp. 348-351.
28. E. Ofitserov, V. D'yakov, M. Rasulov, Biodegrability and silatrane effect mechanism, in: Organosilicon Chemistry V: From Molecules to Materials, in: N. Auner, J. Weis (Eds.), Chapter V. Silicon in Organic and Bioorganic Chemistry, Wiley-VCH Verlag GmbH, Weinheim, Germany, 2008, pp. 356-359.
29. V. G. Pukhalskaya, E. P. Kramarova, L. P. Kozaeva, A. A. Korlyukov, A. G. Shipov, S. Y. Bylikin, V. V. Negrebetsky, G. V. Poryadin, Y. I. Baukov, Synthesis, structure and muscarinic agonist activity of substituted N-(silatrane-1-ylmethyl)acetamides, Appl. Organomet. Chem. 24 (2009) 162-168.
30. M. T. Attar-Bashi, C. Eaborn, J. Vencl, D. R. M. Walton, Silatrane as a reducing agent, J. Organomet. Chem. 117 (1976) C87-C89.
31. K. G. Sólymos, B. Várhegyi, E. Kálman, F. H. Kárman, M. Gál, P. Hencsei, L. Bihátsi, Inhibition of aluminum corrosion in alkaline solutions by silicon and nitrogen containing compounds, Corrosion Science 25 (1993) 1455-1462.

32. O. Prieto, J. E. Haskouri, B.-P. Aurelio, B.-P. Daniel, G. Carmen, L. Julio, M. M. Dolores, A. Pedro, C. Valerio, C. Pedro, C. Saúl, Atrane route to sol gel processes: Experimental study of the hydrolysis mechanism of silatrane. Part I. Rev. Bol. Quim. 19 (2002) 94-100.
33. W. Charoenpinijkarn, M. Suwankruhasn, B. Kesapabutr, S. Wongkasemjit, A. M. Jamieson, Sol-gel processing of silatranes, Eur. Polym. J. 37 (2001) 1441-1448.
34. M. Sathupunya, E. Gulari, S. Wongkasemjit, ANA and GIS zeolite synthesis directly from alumatrane and silatrane by sol-gel process and microwave technique, J. Euro. Ceram. Soc. 22 (2002) 2305-2314.
35. L. Fernandez, P. Viruela-Martin, J. Latorre, C. Guillem, A. Beltrán, P. Amorós, Molecular precursors of mesostructured silica materials in the atrane route: A DFT/GIAO/NBO theoretical study, J. Mol. Struct.: (THEOCHEM) 822 (2007) 89-102.
36. L. S. Shlyakhtenko, A. A. Gall, A. Filonov, Z. Cerovac, A. Lushnikov, Y. L. Lyubchenko, Silatrane-based surface chemistry for immobilization of DNA, protein-DNA complexes and other biological materials, Ultramicroscopy 97 (2003) 279-287.
37. G. D. Yadav, H. G. Manyar, Converting liability into asset: novel mesoporous zeotype from fly ash using silatrane chemistry, Clean Techn. Environ. Policy 7 (2005) 162-167.
38. Martinez, L. Guy, J-P Dutasta, Reversible, solvent-induced chirality switched in atrane structure: control of the unidirectional motion of the molecular propeller, J. Am. Chem. Soc. 132 (2010) 16733-16734.
39. M. G. Voronkov, G. I. Zelchan, Atranes. I. A new method for synthesizing 1-alkyl and aryl silatranes, Khimiya Geterotsiklicheskikh Soedinenii 1 (1965) 51-57.
40. C. L. Frye, G. A. Vincent, W. A. Finzel, Pentacoordinate silicon compounds. V. Novel silatrane chemistry, J. Am. Chem. Soc. 93 (1971) 6805-6811.
41. E. Popowski, M. Michalik, H. Kelling, 2,8,9-Trioxa-5-aza-1-sila-icyclo[3.3.3]undecane-3-one, ein neuer typ von silatranen; darstellung und eigenshaften, J. Organomet. Chem. 88 (1975) 157-164.
42. M. G. Voronkov, V. M. D'yakov, S. V. Kirpichenko, Silatranes, J. Organomet. Chem. 233 (1982) 1-147.
43. M. G. Voronkov, G. I. Zelchan, Atranes XVIII. Kinetics of the hydrolysis of 1-alkyl- and 1-alkoxysilatranes, Khimiya Geterotsiklicheskikh Soedinenii 5 (1969) 450-455.
44. M. G. Voronkov, I. S. Emel'yanov, V. M. D'yakov, V. Yu. Vitkovskii, L. V. Kapranova, V. T. Baryshok, Atranes XLVIII. Kinetics and mechanism of the hydrolysis of 1-(α-chloroalkyl)silatranes, Khimiya Geterotsiklicheskikh Soedinenii 10 (1976) 1344-1346.
45. M. G. Voronkov, D-S. D. Toryashinova, V. P. Baryshok, B. A. Shainyan, É. I. Broadskaya, Kinetic of hydrolysis of silatranes in a neutral medium, Izvestiya Akademii Nauk SSSR Seriya Kimicheskaya 12 (1984) 2673-2676.
46. J. Łukasiak, Z. Jamrógiewicz, Studies on 1-aryloxysilatranes. V^{+}. Studies on the mechanism of hydrolysis of 1-aryloxysilatranes, Acta Chim. Acad. Sci. Hung. 123 (1986) 99-106.
47. M. G. Voronkov, I. S. Emel'yanov, G. I. Zelchan, V. M. D'yakov, I. G. Kuznetsov, Atranes XLII. Kinetics of the hydrolysis of 1-alkoxy- and 1-aryloxysilatranes, Khimiya Geterotsiklicheskikh Soedinenii 1 (1975) 35-39.

48. R. J. Garant, L. M. Daniels, S. K. Das, M. N. Janakiraman, R. A. Jacobson, J. G. Verkade, Lewis basicity of silatranes and the molecular structures of $EtOSi(OCH_2CH_2)_3N$, $Me_2O^+Si(OCH_2CH_2)_3N$, and $CF_3CO_2HEtOSi(OCH_2CH_2)_3N$, J. Am. Chem. Soc. 113 (1991) 5728-5735.
49. J. Woning, L. M. Daniels, J. G. Verkade, Cationic TBP silicon: A stable intermediate in the proton-assisted departure of an equatorial substituent, J. Am. Chem. Soc. 112 (1990) 4601-4602.
50. G. Cerveau, C. Chuit, R. J. P. Corriu, N. K. Nayyar, C. Reye, Pentacoordinate silicon compounds. Reactions of silatranes with nucleophiles, J. Organomet. Chem. 389 (1990) 159-168.
51. É. I. Brodskaya, M. G. Voronkov, Evaluation of the transannular Si←N bond in 1-substituted silatranes, Izvestiya akademii nauk SSSR, Seriya khimicheskaya 7 (1986) 1694.
52. A. Daneshrad, C. Eaborn, R. Eidenschink, D. R. M. Walton, The acid catalyzed solvolysis of 1-organosilatranes, J. Organomet. Chem. 90 (1975) 139-144.
53. V. F. Sidorkin, V. A. Pestunovich, M. G. Voronkov, The physical chemistry of silatranes, Uspekhi Khimii 49 (1980) 789-813.
54. J. Łukasiak, Z. Jamrógiewicz, Studies on 1-aryloxysilatranes. I. Kinetics of the hydrolysis of 1-(2',4',6'-trimethylphenoxy)silatrane, Acta Chim. Acad. Sci. Hung. 105 (1980) 19-25
55. J. Łukasiak, Z. Jamrógiewicz, Studies on 1-aryloxysilatranes. II. Hydrolytic stability of 1-aryloxysilatranes, Acta Chim. Acad. Sci. Hung. 115 (1984) 167-171.
56. S. Belyakov, L. Ignatovich, E. Lukevics, Concerning the transannular bond in silatranes and germatranes: a quantum chemical study, J. Organomet. Chem. 577 (1999) 205-210.
57. [57] Greenberg, C. Plant, C. A. Venanzi, Ab initio molecular orbital study of 1-methylsilatrane and model compounds, J. Mol. Struct.: (THEOCHEM) 234 (1991) 291-301.
58. G. I. Csonka, P. Hencsei, AM1 and PM3 semiempirical molecular orbital study of silatranes. Part 2. The 1-methylsilatrane, J. Mol. Struct.: (THEOCHEM) 283 (1993) 251-259.
59. G. I. Csonka, P. Hencsei, Prediction of geometrical parameters for silatranes: an ab initio molecular orbital and density functional theory study, J. Mol. Struct.: (THEOCHEM) 362 (1996) 199-208.
60. K. A. Lyssenko, A. A. Korlyukov, M. Y. Antipin, S. P. Knyazev, V. N. Kirin, M. V. Alexeev, E. A. Chernyshev, The nature of the intramolecular transannular Si···N interaction in crystalline 1-methylsilatrane, as found from X-ray diffraction data, Medeleev Commun. 10 (2000) 88-90.
61. A. Korlyukov, K. A. Lyssenko, M. Y. Antipin, V. N. Kirin, E. A. Chernyshev, S. P. Knyazev, Experimental and theoretical study of the transannular intramolecular interaction and cage effect in the atrane framework of boratrane and 1-methylsilatrane, Inorg. Chem. 41 (2002) 5043-5051.
62. A. Korlyukov, M. Y. Antipin, I. Bolgova, O. M. Trofimova, M. G. Voronkov, Chemical bonding in the crystal structure of 1-hydrosilatrane, Russ Chem. Bull., Intl. Ed., 58 (2009) 25-30.

63. J. I. Musher, The chemistry of hypervalent molecules, Agnew. Chem. Int. Ed. Engl. 8 (1969) 54-59.
64. M. S. Gordon, L. P. Davis, L. W. Burggraf, The structure and stability of neutral pentacoordinated silicon compounds, Chem. Phys. Lett. 163 (1989) 371-374.
65. M. S. Gordon, M. T. Carroll, J. H. Jensen, L. P. Davis, L. W. Burggraf, R. M. Guldry, Nature of the Si-N bond in silatranes, Organomet. 10 (1991) 2657-2660.
66. M. W. Schmidt, T. L. Windus, M. S. Gordon, Structural trends in silicon atranes, 117 (1995) 7480-7486.
67. T. Dahl, P. M. Skancke, Structural aspects of a possible transannular interaction in silatranes and azasilatranes: an ab initio study, Int. J. Quant. Chem. 60 (1996) 567-578.
68. Yoshikawa, M. S. Gordon, V. F. Sidorkin, V. A. Pestunovich, Proton affinities of the silatranes and their analogues, Organomet. 20 (2001) 927-931.
69. A. Milov, R. M. Minayer, V. I. Minkin, Hypervalent intramolecular X←N(X=C, Si, Ge) coordination in atranes: quantum chemical study, Zhurnal Organicheskoi Khimii, 39 (2003) 372-279.
70. M. V. Zabalov, S. S. Karlov, G. S. Zaitseva, D. A. Lemenovskii, The molecular and electronic structure features of silatranes, germatranes, and their carbon analogs, Russ. Chem. Bull., Intl. Ed., 55 (2006) 464-476.
71. O. Prieto, J. E. Haskouri, A. Pedro, C. Valerio, R. Pujro, C. Pedro, C. Saúl, Atrane route to sol gel processes: Theoretical study of the hydrolysis mechanism of silatrane. Part II. Rev. Bol. Quim. 19 (2002) 101-107.
72. E. A. Chernyshev, S. P. Knyazev, V. N. Kirin, I. M. Vasilev, N. V. Alekseev, Structural features of silatranes and germatranes, Zhurnal Obshchei Khimii, 74 (2004) 65-73.
73. J. E. Boggs, C. Peng, V. A. Pestunovich, V. F. Sidorkin, Structure and bonding of 1-methylsilatrane and 1-fluorosilatrane, J. Mols. Struct.: (THEOCHEM) 357 (1995) 67-73.
74. F. Shishkov, L. V. Khristenko, F. M. Rudakov, A. B. Golubinskii, L. V. Vilkov, S. S. Karlov, G. S. Zaitseva, S. Samdal, Molecular structure of silatrane determined by gas electron diffraction and quantum-mechanical calculations, Struct. Chem. 15 (2004) 11-16.
75. M. G. Voronkov, V. P. Baryshok, Atranes as a new generation of biologically active substances, Vestnik Rossiiskoi Akademii Nauk 80 (2010) 985-992.
76. J. K. Puri, R. Singh, V. K. Chanal, Silatranes: a review on their synthesis, structure, reactivity and applications, Chem. Soc. Rev. 40 (2011) 1791-1840.
77. T. Kudo, M. S. Gordon, Theoretical studies on the mechanism for the synthesis of silsesquioxanes. 1. Hydrolysis and initial condensation, J. Am. Chem. Soc. 120 (1998) 11432-11438.
78. M. Cypryk, Y. Apeloig, Mechanism of the acid-catalyzed Si-O bond cleavage in siloxanes and siloxanols. A theoretical study, Organomet. 21 (2002) 2165-2175
79. Chr. Møller, M. S. Plesset, Note on an approximate treatment for many-electron systems, Phys. Rev. 46 (1934) 618-622.
80. G. D. Fletcher, M. W. Schmidt, M. S. Gordon, Developments in parallel electronic structure theory, in I. Prigogine, S. A. Rice, (Eds.), Advances in Chemical Physics, Vol. 110, John Wiley & Sons, Inc., Hoboken, New Jersey, 1999, pp. 267-294.

81. C. M. Aikens, S. P. Webb, R. L. Bell, G. D. Fletcher, M. W. Schmidt, M. S. Gordon, A derivation of the frozen-orbital unrestricted open-shell and restricted closed-shell second-order perturbation theory analytic gradient expressions, Theoret. Chem. Acc., 110 (2003) 233-253.
82. R. Ditchfield, W. J. Hehre, J. A. Pople, Self-consistent molecular-orbital methods. IX. An extended Gaussian-type basis for molecular-orbital studies of organic molecules, J. Chem. Phys. 54 (1971) 724-728.
83. W. J. Hehre, R. Ditchfield, J. A. Pople, Self-consistent molecular-orbital methods. XII. Further extensions of Gaussian-type basis for molecular-orbital studies of organic molecules, J. Chem. Phys. 56 (1972) 2257-2261.
84. M. S. Gordon, Chem. Phys. Lett. 76 (1980) 163-168.
85. M. M. Francl, W. J. Pietro, W. J. Hehre, J. S. Binkley, M.S. Gordon, D. J. DeFrees, J. A. Pople, Self-consistent molecular-orbital methods. XXIII. A polarization-type basis set for second-row elements, J. Chem. Phys.77 (1982) 3654-3665.
86. P. Culot, G. Dive, V. H. Nguyen, J. M. Ghuysen, A quasi-Newton algorithm for first-order saddle-point location, Theor. Chim. Acta 82 (1992) 189-205.
87. K. Fukui, The path of chemical reactions – the IRC approach, Acc. Chem. Res. 14 (1981) 363-368.
88. C. Gonzalez, H. B. Schlegel, An improved algorithm for reaction path following, J. Chem. Phys. 90 (1989) 2154-2161.
89. C. Gonzalez, H. B. Schlegel, Reaction path following in mass-weighted internal coordinates, J. Chem. Phys. 94 (1990) 5523-5527.
90. M. A. Spackman, Potential derived charges using a geodesic point selection scheme, J. Comput. Chem. 17 (1996) 1-18.
91. P. Piecuch, S. A. Kucharski, K. Kowalski, M. Musial, Efficient computer implementation of the renormalized coupled-cluster methods: The R-CCSD[T], R-CCSD(T), CR-CCSD[T], and CR-CCSD(T) approaches, Comput. Phys. Commun. 149 (2002) 71-96.
92. P. Piecuch, M. Włoch, Renormalized coupled-cluster methods exploiting left eigenstates of the similarity-transformed Hamiltonian, J. Chem. Phys. 123 (2005) 224105/1-10.
93. V. Barone, M. Cossi, Quantum calculation of molecular energies and energy gradients in solution by a conductor solvent model, J. Phys. Chem. A. 102 (1998) 1995-2001.
94. M. Cossi, N. Rega, G. Scalmani, V. Barone, Energies, structures, and electronic properties of molecules in solution with the C-PCM solvation model, J. Comput. Chem. 24 (2003) 669-681.
95. M. S. Gordon, M. W. Schmidt, Advances in electronic structure theory: GAMESS: A decade later, in C. E. Dykstra, G. Frenking, K. S. Kim, G. E. Sucseria, (Eds.), Theory and Applications of Computational Chemistry: The First Forty Years, Elsevier, Amsterdam, 2005, pp. 1167-1189.
96. B. M. Bode, M. S. Gordon, Macmolplt: A graphical user interface for GAMESS, J. Mol. Graphics Mod., 16 (1998) 133-138.
97. I. Mayer, Charge, bond order and valence in the *ab initio* SCF theory, Chem. Phys. Lett. 97 (1983) 270-274.

98. M. G. Voronkov, V. P. Mileshkevich, Yu. A. Yuzhelevskii, The Siloxane Bond, first ed., Consultants Bureau, New York, 1978.

CHAPTER 3. SOLVENT-INDUCED SHIFT OF *p*-NITROANILINE IN WATER: AN APPLICATION OF THE TDDFT/EFP METHOD

A paper submitted to *The Journal Physical Chemistry A*

Sarom Sok[†], Soohaeng Y. Willow[‡], Federico Zahariev[†], Mark S. Gordon[†]

Abstract

The combined time-dependent density functional theory/effective fragment potential method (TDDFT/EFP1) is applied to a study of the solvent-induced shift of the lowest singlet $\pi\rightarrow\pi^*$ charge-transfer excited state of *p*-nitroaniline (*p*NA) from the gas to the condensed phase in water. Molecular dynamics simulations of *p*NA with 150 EFP1 water molecules are used to model the condensed-phase and generate a simulated spectrum of the lowest singlet charge-transfer excitation. The TDDFT/EFP1 method successfully reproduces the experimental condensed-phase $\pi\rightarrow\pi^*$ vertical excitation energy and solvent-induced red shift of *p*NA in water. The largest contribution to the red shift comes from Coulomb interactions, between *p*NA and water, and solute relaxation. The solvent shift contributions reflect the increase in zwitterionic character of *p*NA upon solvation.

1. Introduction

The ability to interpret, guide and model experiments is one of the major goals of quantum chemistry. Several computational methods are available to calculate the electronic properties of small- and medium-sized gas phase molecules in the excited state. Examples include time-dependent density functional theory (TDDFT), singly excited configuration interaction with perturbative doubles (CIS(D)), equation-of-motion coupled cluster with single and double excitations (EOM-CCSD), and multi-reference (MR) methods such as MR

[†] Department of Chemistry and Ames Laboratory, Iowa State University, Ames, IA 50011-3111
[‡] Center for Superfunctional Materials, Department of Chemistry, Pohang University of Science and Technology, San 31, Hyojadong, Namgu, Pohang 790-784, Korea

configuration interaction and MR perturbation theory [1]. However, most experiments occur in solution and the effect of the surrounding environment (solvent) needs to be taken into account in order to accurately describe a molecular system in the condensed phase [2,3].

The approaches for modeling environmental effects can be divided into three categories:

1. "Supermolecular solvation" models environmental effects by explicitly including the solvent molecules and treating the entire system with the same level of quantum mechanics (QM). The treatment of long-range solvent effects and the applicability to extended systems is limited because the computational scaling of supermolecular QM methods is dependent on the level of theory employed; e.g., N^4 scaling for TDDFT, N^5 scaling for CIS(D), and N^6 scaling for EOM-CCSD where N is a measure of the system size [4].
2. "Continuum solvation" places the solute in a molecular cavity and replaces the solvent with a homogeneous medium represented by a dielectric constant. Continuum methods are computationally efficient, reasonably accurate for bulk properties, and able to treat large molecules [5]. However, the weaknesses of the continuum solvation approach are the sensitivity to cavitation properties [6,7] and the inability to treat specific solute-solvent interactions, such as hydrogen bonding [8,9], due to the lack of explicit solvent molecules.
3. "Discrete solvation" treats each component of the environment explicitly and specific solute-solvent interactions are taken into account. The computational complexity and accuracy of discrete methods are dependent on the level of sophistication and empiricism of the potentials used. Bulk characteristics of the solvent are frequently obtained using molecular dynamics or Monte Carlo simulations through a hybrid quantum mechanics/molecular mechanics (QM/MM) approach [10-14]. Sufficient sampling of configurations becomes a bottleneck with QM/MM methods as the size of the environment increases [15], thereby driving the need for accurate and computationally efficient discrete solvation approaches.

Of the three different solvation approaches, the discrete method offers an appealing compromise between accuracy and computational scalability, especially when the solvent-solute interactions include hydrogen bonding.

The effective fragment potential (EFP) method is a discrete QM-based approach for modeling environmental effects [16-20]. The original EFP method, EFP1, was developed to describe the condensed-phase of water and has been successfully applied to the study of water clusters [21-24], chemical reactions in aqueous solution [25,26], environmental effects on biomolecular systems [27-30], and solvent effects on electronic excitations [31-35]. The EFP1 method consists of three terms that represent the important intermolecular (nonbonded) interactions that are added as one-electron contributions to the quantum mechanical Hamiltonian of the solute: Coulomb (electrostatic), induction (polarization), and a remainder term to account for all interactions not captured by the first two terms. In the Hartree-Fock (HF) based EFP1 method, the remainder term contains exchange repulsion and charge transfer [16]. In the density functional theory (DFT) based EFP1 method, the remainder term also includes short-range electron correlation [17]. In EFP1, the remainder term is fitted to two separate functional forms depending on whether one is considering solute-solvent or solvent-solvent interactions. Because the EFP1 solute-solvent interaction potentials consist of only one-electron integrals, the computational overhead for including environmental effects is small compared to the QM method used. The EFP1 method for water has been interfaced with HF [16], DFT [17,19], multi-configurational self-consistent field (MCSCF) [26], singly excited configuration interaction (CIS) [31], EOM-CCSD [32], and CIS(D) [33]. Recently, the EFP1 method has been interfaced with TDDFT for excited states, permitting the study of optical properties of chromophores in aqueous media [34,35].

Figure 1. Neutral and zwitterionic resonance structures of *p*-nitroaniline.

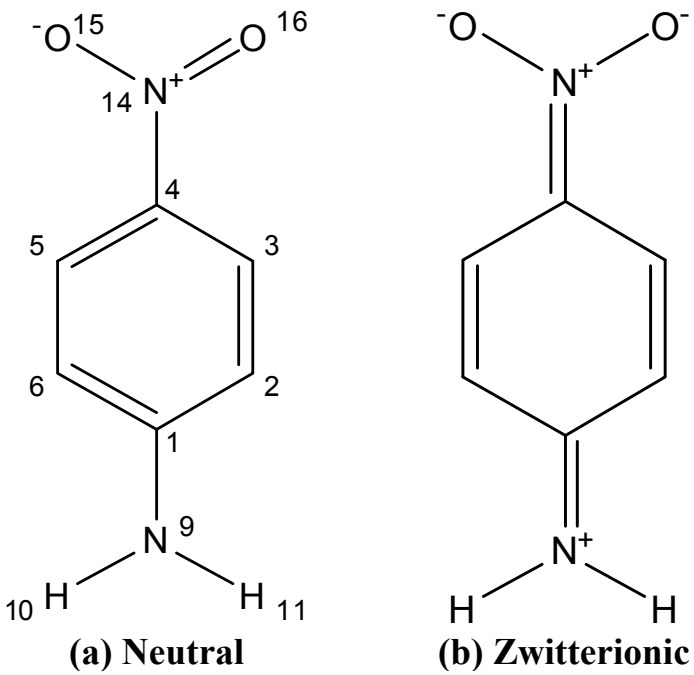

p-nitroaniline (*p*NA), Figure 1, is an important prototypical organic push-pull (donor-π-acceptor) chromophore and has been the subject of many theoretical [32,33,36-46] and experimental [47-54] studies. *p*NA can be represented by two mesomeric structures: neutral and zwitterionic [47]. Changes within the conjugated molecular framework of the neutral form (Figure 1a), through transfer of charge or distortions caused by solvent interactions, can increase the importance of the zwitterionic form (Figure 1b). The degree of zwitterionic character reflects the amount of charge separation. For donor-π-acceptor molecules, the increase in zwitterionic character and the subsequent increase in dipole moment are stabilized in polar solvents through solvent interactions such as hydrogen bonding [2]. *p*NA possesses a strong $\pi \rightarrow \pi^*$ absorption band in the near-ultraviolet to visible spectral region [36]. The low lying singlet excited state is associated with an intramolecular charge transfer from the amino group to the nitro group across the phenyl ring, leading to a change in the dipole moment of *p*NA [37,38]. The peak of the $\pi \rightarrow \pi^*$ absorption band is strongly dependent on the solvent polarity due to the increase in the dipole moment upon photoexcitation [39,48]. Twisting of the nitro group relative to the conjugated framework lowers the energy of the

charge-transfer excited state and increases the dipole moment [37-50]. An experimental -0.98 eV red shift of the charge-transfer excited state is observed upon going from the gas phase, 4.24 eV [48], to the aqueous phase, 3.26 eV [49,50].

Recently, Slipchenko used the EFP method for water and EOM-CCSD for *p*NA to investigate the solvent-induced shift of the singlet $\pi\rightarrow\pi^*$ charge-transfer excited state of *p*NA-water$_n$ complexes (n = 2, 4, 6) [32]. Slipchenko observed that the polarization response of the solvent to the excited state electron density contributes less than ≈ 5% to the total solvent-induced red shift. The largest contributions to the solvent shift come from "indirect" contributions, where "indirect" contributions refer to the orbital relaxation of the ground state of the solute in the presence of the electrostatic field of the solvent. The largest "indirect" contribution to the solvent shift, about 80%, is from the Coulomb interactions between *p*NA and water.

In a related study, Kosenkov and Slipchenko investigated the solvent-induced shift of *p*NA in water using a QM/MM (CIS(D)/EFP) approach [33]. Molecular dynamics (MD) simulations of *p*NA and 64 EFP solvent molecules using periodic boundary conditions, in which the *p*NA geometry was frozen, were used to model the condensed phase. These calculations reproduced the red shift of the lowest singlet $\pi\rightarrow\pi^*$ charge-transfer excited state in water to within 0.02 eV of experiment and the spectral line width in the condensed-phase to within 0.14 eV of experiment. However, the experimental gas and condensed phase vertical excitation energies for the singlet charge transfer state were overestimated by 0.41 eV and 0.39 eV, respectively.

In the current work, the TDDFT/EFP1 method is used to study the lowest singlet $\pi\rightarrow\pi^*$ charge-transfer excited state of *p*NA in water. MD simulations of *p*NA with 150 EFP1 water molecules are used to model the condensed phase. The solvent-induced (solvatochromic) shift from the gas to the condensed phase is calculated and compared with experiment. The density functional dependence of the calculated solvent shifts is investigated and the accuracy and computational efficiency of the TDDFT/EFP1 method is discussed.

The structure of this paper is as follows. The next section briefly describes the TDDFT/EFP1 method. This is followed by a summary of the computational details, the

results, and a discussion of the calculations. Concluding remarks are given in the last section.

3. The TDDFT/EFP1 Method

The formulation of the TDDFT/EFP1 method has been described by Yoo *et al.* [34] and Minezawa *et al.* [35]; therefore, the method is only briefly summarized here. In the TDDFT/EFP1 method the solvent is treated with EFP1/DFT [16,17,19] and the interaction energy is a sum of three terms,

$$E_{\text{Interaction}}^{\text{EFP1}} = \sum_{\eta} \left[\sum_{k=1}^{K} E_k^{\text{Coul}}(\eta) + \sum_{l=1}^{L} E_l^{\text{pol}}(\eta) + \sum_{m=1}^{M} E_m^{\text{rem}}(\eta) \right] \quad (1)$$

where η sums over the solvent molecules. For the ηth solvent molecule, these contributions are expanded over a number (K, L, and M) of expansion points.

The first term in Eq. (1) represents the Coulomb interaction and is expressed using a distributed multipolar expansion of the fragment molecular density, carried out through octopole moments. For water, $K = 5$ expansion points are used (atom centers and bond midpoints). The Coulomb term is scaled by a distance dependent damping term to account for overlapping charge densities at small intermolecular distances.

The second term in Eq.(1) represents the polarization interaction energy and is represented using localized molecular orbital (LMO) polarizability tensors. For water, $L = 4$ expansion points are used, centered at the two O-H bonds and the two oxygen lone pairs. The polarization term is iterated within the Kohn-Sham iterations until self-consistency is reached.

The last term in Eq. (1) is a remainder term containing interaction energy components not captured by the Coulomb and polarization terms. The remainder term is fitted to a functional form by first computing the water dimer potential energy and then subtracting the first two terms in Eq. (1) from the quantum mechanical (QM) water dimer potential. If a HF based water dimer potential is used, the remainder term will contain the exchange repulsion and charge transfer interaction energies. If a DFT based water dimer potential is used, the remainder term will also include some short-range electron correlation.

The EFP1 water molecules are allowed to rotate and translate, but the internal geometry is fixed. The bond length and bond angle of an EFP1/DFT water molecule is 0.9468 Å and 106.70º, respectively.

In the TDDFT/EFP1 method, the linear response formulation of the TDDFT equations is used [55-59],

$$\begin{bmatrix} \mathbf{A} & \mathbf{B} \\ \mathbf{B} & \mathbf{A} \end{bmatrix} \begin{bmatrix} \mathbf{X} \\ \mathbf{Y} \end{bmatrix} = \omega \begin{bmatrix} 1 & 0 \\ 0 & -1 \end{bmatrix} \begin{bmatrix} \mathbf{X} \\ \mathbf{Y} \end{bmatrix} \tag{2}$$

Solutions to the non-Hermitian eigenvalue problem in Eq. (2) yields the transition energy, ω, and the corresponding bi-orthonormal transition vectors $\mathbf{X}$ and $\mathbf{Y}$. The matrices $\mathbf{A}$ and $\mathbf{B}$ in Eq. (2) are defined as

$$A_{ia\mu,jb\nu} = \delta_{ij}\delta_{ab}\delta_{\mu\nu}\left(\varepsilon_a - \varepsilon_i\right) + K_{ia\mu,jb\nu} \tag{3}$$

and

$$B_{ia\mu,jb\nu} = K_{ia\mu,bj\nu} \tag{4}$$

where indices i, j and a, b label occupied and virtual orbitals, respectively, while the indices μ, ν denote spin. ε_a and ε_i are orbital energies for Kohn-Sham orbitals ϕ_a and ϕ_i, respectively. The coupling matrix [60] $K_{ia\mu,jb\nu}$ is given by

$$K_{ia\mu,jb\nu} = \iint \phi^*_{i\mu}(\mathbf{r})\phi_{a\mu}(\mathbf{r})\left(\frac{1}{|\mathbf{r}-\mathbf{r}'|} + \frac{\delta^2 E_{\mathrm{xc}}}{\delta\rho_\mu(\mathbf{r})\delta\rho_\nu(\mathbf{r}')}\right)\phi_{j\nu}(\mathbf{r}')\phi^*_{b\nu}(\mathbf{r}')\,d\mathbf{r}d\mathbf{r}' \tag{5}$$

where E_{xc} is the exchange-correlation energy. ρ_μ and ρ_ν are electron spin densities.

The only EFP1 term that contributes to the coupling matrix $\mathbf{K}$, after taking the second functional derivative with respect to the electron density, is the polarization, so that the EFP1-modified coupling matrix $\mathbf{K}$ becomes,

$$\begin{aligned} K_{ia\mu,jb\nu} = & \iint \phi^*_{i\mu}(\mathbf{r})\phi_{a\mu}(\mathbf{r})\left(\frac{1}{|\mathbf{r}-\mathbf{r}'|}\right)\phi_{j\nu}(\mathbf{r}')\phi^*_{b\nu}(\mathbf{r}')\,d\mathbf{r}d\mathbf{r}' \\ & + \iint \phi^*_{i\mu}(\mathbf{r})\phi_{a\mu}(\mathbf{r})\left(\frac{\delta^2 E_{\mathrm{xc}}}{\delta\rho_\mu(\mathbf{r})\delta\rho_\nu(\mathbf{r}')}\right)\phi_{j\nu}(\mathbf{r}')\phi^*_{b\nu}(\mathbf{r}')\,d\mathbf{r}d\mathbf{r}' \\ & + \iint \phi^*_{i\mu}(\mathbf{r})\phi_{a\mu}(\mathbf{r})\left(\frac{\delta^2 E^{\mathrm{pol}}}{\delta\rho_\mu(\mathbf{r})\delta\rho_\nu(\mathbf{r}')}\right)\phi_{j\nu}(\mathbf{r}')\phi^*_{b\nu}(\mathbf{r}')\,d\mathbf{r}d\mathbf{r}' \end{aligned} \tag{6}$$

The EFP1 solvent molecules affect the TDDFT excited state calculation directly through the polarization term in the modified coupling matrix **K** and indirectly through changes in the solute geometry (solute relaxation) and ground state electron density due to the presence of the effective fragments. Previous works [31,35,83] have shown that consideration of the excited state electron density with respect to the response of the solvent polarization makes a very small contribution to the calculated excitation energies; therefore, it is not taken into account in the current study.

3. Computational Methods

Solvatochromic shift values are calculated as the differences between the gas and condensed phase vertical excitation energies of the solute. The statistically averaged condensed phase vertical excitation energy is obtained in a two-step process. First, a molecular dynamics simulation is used to obtain a set of representative configurations (snapshots) of the solute-solvent system. Then, the lowest singlet $\pi \rightarrow \pi^*$ TDDFT vertical excitation energy is calculated for each configuration. The condensed phase vertical excitation energy of the solute is taken as the central value of a Gaussian function fitted to the histogram of calculated vertical excitation energies.

Molecular Dynamics Simulation

A Born-Oppenheimer *ab initio* MD simulation was performed on a non-periodic system consisting of *p*NA surrounded by 150 water molecules, within the canonical ensemble (NVT) at a fixed temperature of 300 K using a Nosé-Hoover thermostat [61]. The 150 water molecules (MM region) were treated as DFT-based EFP1 fragments, called EFP1/DFT [17,19]. The *p*NA molecule (QM region) was treated with DFT using the Becke 3-parameter (exchange) [62] and Lee-Yang-Parr (correlation) [63] (B3LYP) hybrid functional [64] and the Dunning-Hay basis set [65] with *d* polarization functions on oxygen and *p* polarization functions on hydrogen atoms (DH(d,p)), to be consistent with the functional and basis set used to develop EFP1/DFT. The isolated system was equilibrated for 20 picoseconds with a 1.0 femtosecond time step. Snapshots were collected every 10 time steps from a 20 picosecond production run giving a total of 2000 configurations.

Vertical Excitations

Both gas and condensed phase vertical excitation energies were calculated using TDDFT with the B3LYP functional (TD-B3LYP) and the DH(d,p) basis set. The structure of the solute used in the gas phase excited state calculation was obtained from the optimized ground state geometry of *p*NA calculated at the B3LYP/DH(d,p) level of theory, in C_1 symmetry. Structures used in the condensed phase vertical excitation energy calculations were obtained from snapshots of the QM/MM (B3LYP/EFP1) MD simulation production run.

Additional TDDFT calculations with the Perdew-Berke-Ernzerhof hybrid [66,67] (TD-PBE0) and the Coulomb-attenuated method B3LYP [68] functional (TD-CAM-B3LYP) and the DH(d,p) basis set were performed to investigate the density functional dependence of the solvatochromic shift. In the TD-PBE0 and TD-CAM-B3LYP calculations, the optimized gas phase structure of *p*NA obtained at the B3LYP/DH(d,p) level of theory and the 2000 condensed phase snapshots of *p*NA with 150 EFP1 water molecules obtained from the QM/MM (B3LYP/EFP1) MD simulation production run were used.

Both ground state DFT and excited state TDDFT calculations were carried out using the (96, 1202) Euler-MacLaurin radial [69] and Lebedev angular [70] grid. For computational efficiency, the MD simulation employed a smaller (96, 590) Euler-MacLaurin radial and Lebedev angular grid.

Lambda Diagnostic

The lambda diagnostics of Peach *et al.* [71] quantifies the degree of orbital overlap between occupied-virtual pairs (transition vectors) contributing to an excited state. Λ is calculated as the sum of spatial overlaps, O_{ia}, between transition vectors involved in an excited state weighted by the square of the transition amplitude κ_{ia},

$$\Lambda = \frac{\sum_{ia} \kappa_{ia}^2 O_{ia}}{\sum_{ia} \kappa_{ia}^2} \tag{7}$$

where the spatial overlap is given as the inner product of the moduli of occupied and virtual Kohn-Sham orbitals, ϕ_i and ϕ_a,

$$O_{ia} = \left\langle \left|\phi_i\right| \left|\phi_a\right| \right\rangle = \int \left|\phi_i(\mathbf{r})\right| \left|\phi_a(\mathbf{r})\right| d\mathbf{r} \quad (8)$$

and,

$$\kappa_{ia} = \mathbf{X}_{ia} + \mathbf{Y}_{ia} \quad (9)$$

X and Y are the transition vectors defined in Eq. (2). Lambda values range from 0 to 1 with small lambda values indicating low-overlap/long-range excitations (e.g. Rydberg excited states) and large lambda values signifying high-overlap/short-range excitations (e.g. low-lying valence excited states). Charge-transfer excited states possess intermediate lambda values. Several studies have demonstrated errors in calculated excitation energies for small lambda values and large charge-transfer character [71-76]. Excitation energies with lambda values < 0.3 for hybrid density functionals are most likely to be significantly underestimated. The lambda diagnostic of Peach *et al.* is used in the current study to assess the degree of charge transfer for the lowest singlet $\pi \rightarrow \pi^*$ intramolecular charge-transfer excited state of *p*NA.

Partial atomic charges were calculated using the geodesic electrostatic potential derived charge method of Spackman [77]. All calculations were performed using the General Atomic and Molecular Electronic Structure System (GAMESS) quantum chemistry code [78] and visualized using MacMolPlt [79].

4. Results and Discussions

Calculations in the Gas-phase

Geometric parameters for the B3LYP/DH(d,p) optimized gas-phase structure of *p*NA are summarized in Table 1. The gas-phase structure of *p*NA in the ground state is nearly planar with a dihedral angle on the amino group of ≈ ±20°. The predicted bond lengths are in reasonable agreement with the MP2 calculations of Sim *et al.* using a double-ξ quality basis set [40] and the experimental crystallography data of Trueblood *et al.* [51]. The calculated dipole moment of 7.3 Debye is comparable to the experimental measurement of Breitung *et al.* [52] in dilute benzene solution, 7.6 Debye, and CIS(D) studies of Kosenkov and Slipchenko, 7.7 Debye [33].

Table 1. Ground state structural parameters (in angstroms and degrees) calculated for *p*-nitroaniline (see Figure 1).

	Gas-phase			Condensed-phase
	B3LYP[a]	MP2[b]	Exptl.[c]	B3LYP-EFP1[d]
$R(C_2\text{-}C_1)$	1.416	1.411	1.41	1.434
$R(C_3\text{-}C_2)$	1.391	1.394	1.37	1.380
$R(C_4\text{-}C_3)$	1.403	1.398	1.39	1.421
$R(C_1\text{-}N_9)$	1.355	1.379	1.35	1.346
$R(C_4\text{-}N_{14})$	1.461	1.465	1.45	1.412
$R(N_{14}\text{-}O_{15})$	1.240	1.247	1.23	1.264
$\theta(C_2C_1N_9H_{10})$	±19.9			±10.0
$\theta(C_5C_4N_{14}O_{15})$	0.0			±7.9

[a](This work) From an optimized gas-phase structure obtained at the B3LYP/DH(d,p) level of theory.
[b](Ref. 40)
[c](Ref. 51)
[d]From an average of 2000 snapshots of *p*-nitroaniline with 150 EFP1 water molecules during the QM/MM (B3LYP/EFP1) MD simulation.

Figure 2. Kohn-Sham molecular orbitals of dominant linear response TD-B3LYP/DH(d,p) transition vector for the lowest singlet π→π* charge transfer excitation of *p*-nitroaniline in the gas phase.

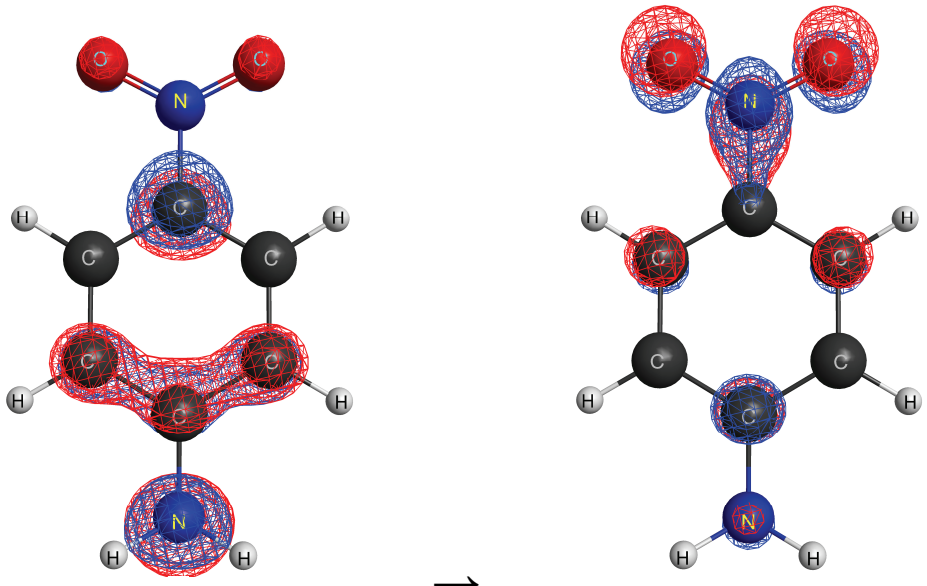

For the optimized gas phase structure of *p*NA, TD-B3LYP/DH(d,p) predicts a vertical excitation energy of 3.97 eV for the lowest singlet $\pi \rightarrow \pi^*$ transition; a lambda diagnostic value of 0.593 indicates that this transition has charge-transfer character. The calculated gas phase dipole moment of *p*NA is found to increase in the excited state to 12.5 Debye. The dominant transition vector contributing to the description of the singlet charge-transfer excited state of *p*NA in the gas phase involves excitation from the highest occupied molecular orbital (HOMO) to the lowest unoccupied molecular orbital (LUMO). These orbitals are illustrated in Figure 2. The predicted value for the excitation energy of the singlet charge-transfer excited state is underestimated by 0.27 eV, compared to the experimental gas-phase value of 4.24 eV [48]. The CIS(D) calculations of Kosenkov and Slipchenko overestimates the gas phase charge-transfer excitation energy of *p*NA by 0.41 eV [33]. Kosenkov and Slipchenko attribute the discrepancy in the calculated gas phase value to the use of a small basis set. Improvement in the TDDFT calculated vertical excitation energy can be achieved by increasing the basis set, as shown by Scalmani *et al.* [41] using the 6-311G(d,p) basis set and the B3LYP functional, 4.07 eV, or using a density functional designed to have a proper long-range (asymptotic) behavior of the exchange-correlation potential.

Calculations in Aqueous Solution

Figure 3. An example of a single configuration (snapshot) of *p*-nitroaniline (ball and stick) with 150 EFP1 water molecules (wire frame) during the QM/MM (B3LYP/EFP1) MD simulation. Atoms on *p*-nitroaniline are labeled.

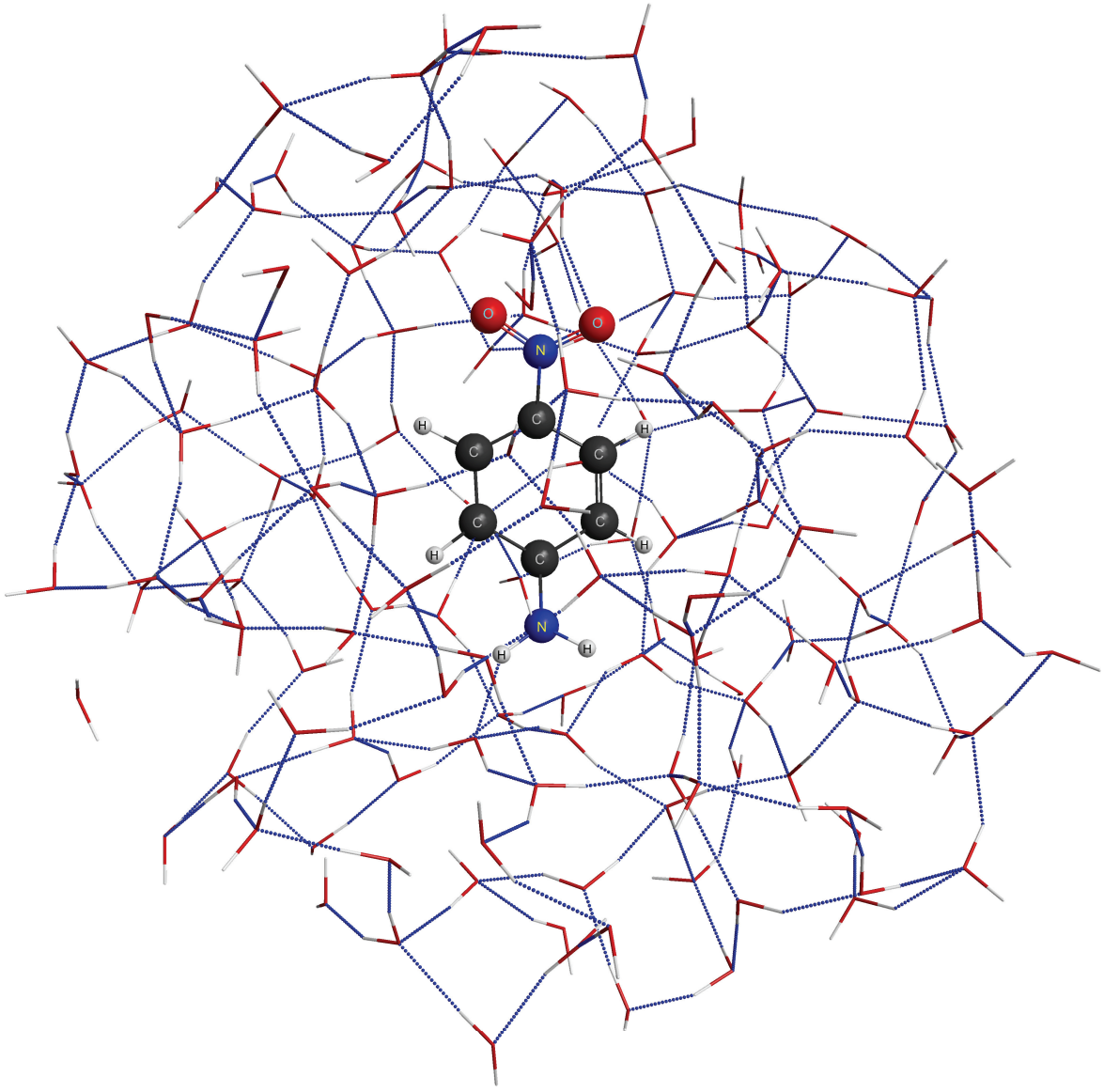

MD simulations of *p*NA with 150 EFP1 water molecules were performed to model the condensed phase. During an MD simulation, the solute geometry and hydrogen-bonding arrangement of the solvent cage is allowed to fluctuate, producing a distribution of configurations. A representative structure is illustrated in Figure 3. Averaged values are reported for all condensed phase properties calculated.

The averaged geometric parameters for the condensed phase structure of *p*NA in the ground state are summarized in Table 1. Structural changes of *p*NA upon solvation are marked by a modest increase in the nitro N_{14}-O_{15} bond and a small shortening of the phenyl C_2-C_3 and nitro C_4-N_{14} bond. The change in bond lengths is accompanied by a decrease in the dihedral angles of the amino and nitro groups of $\approx \pm 10°$ and $\approx \pm 7°$, respectively. The calculated ground state dipole moment of *p*NA in the aqueous phase is 16.2 Debye. The significant increase in the dipole moment of *p*NA in the condensed phase is in qualitative agreement with the semiempirical calculations of Farztdinov *et al.* [39] and of Kovalenko *et al.* [50]. Table 1S in the supporting information presents B3LYP/DH(d,p) calculated gas and condensed phase partial atomic charges on the nitrogens in the amino and nitro groups of *p*NA, exhibiting an increase in negative and positive charge, respectively. This reflects an increase in the charge separation upon solvation. The observed structural changes, increase in dipole moment, and charge separation are indicative of an increase in the zwitterionic character of the ground-state structure of *p*NA in the condensed-phase.

The simulated spectrum of the lowest singlet $\pi \rightarrow \pi^*$ charge-transfer excited state of *p*NA in the condensed-phase is shown in Figure 4. The TD-B3LYP/EFP1 calculated charge-transfer band is centered at 3.37 eV with a lambda diagnostic value of 0.677. The calculated excited state dipole moment of *p*NA in the condensed phase is 17.0 Debye. The predicted value for the singlet $\pi \rightarrow \pi^*$ excitation is in good agreement (within 0.11 eV) with the experimental value of 3.26 eV [49,50]. However, the TD-B3LYP/EFP predicted spectral full line width at half maximum (FWHM), 0.23 eV, underestimates the experimental value of 0.6 eV [50]. Predicting spectral line widths that are in agreement with experiment may require the use of periodic boundary conditions, as was done by Kosenkov and Slipchenko [33].

Figure 4. Simulated condensed-phase spectrum for the π→π* excitation of *p*-nitroaniline (dashed line). Gaussian function centered at 3.37 eV fitted to the histogram of calculated π→π* vertical excitation energies from QM/MM (B3LYP/EFP1) MD simulation.

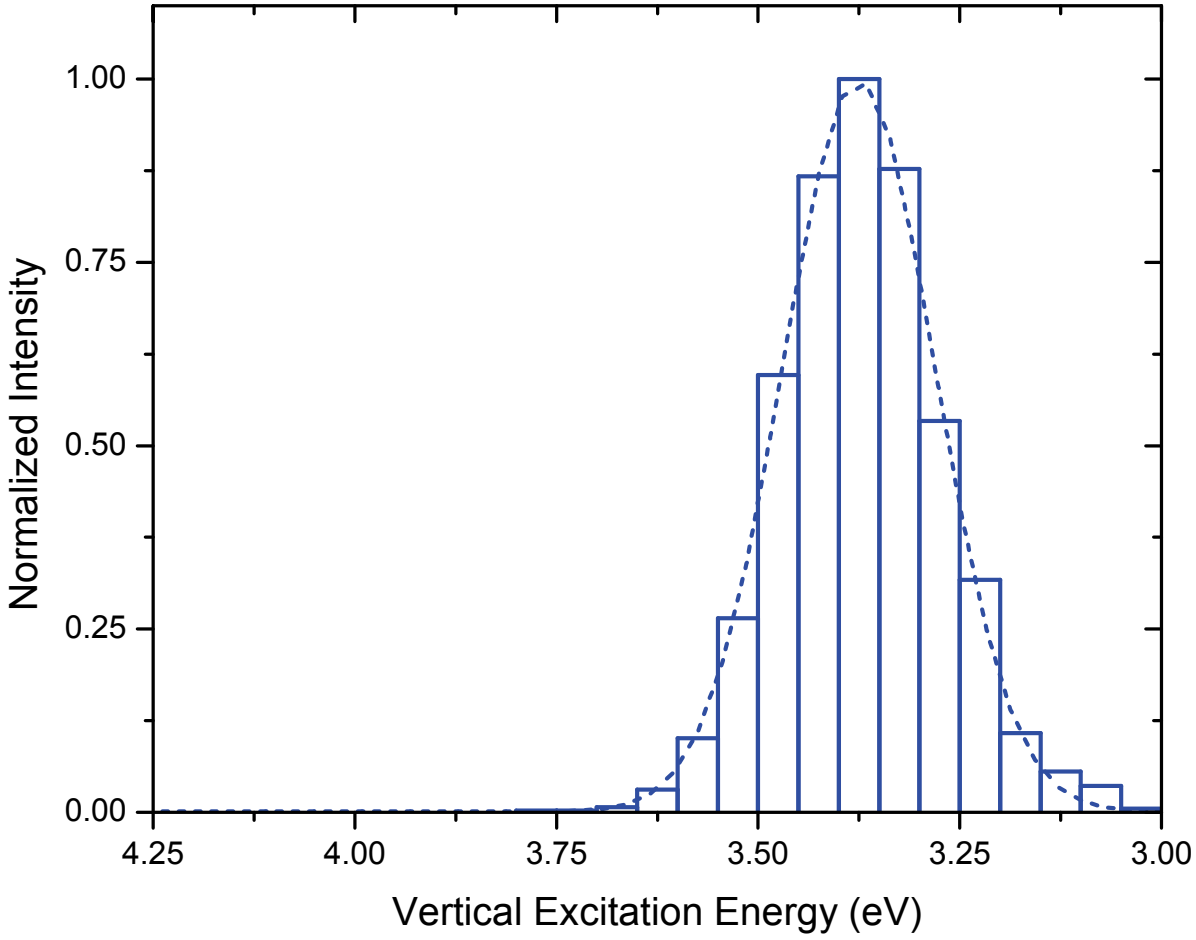

Solvent Shift

Table 2 compares the calculated and experimental solvent-induced shifts for the lowest singlet π→π* charge-transfer excited state of *p*NA. Going from the gas to the condensed phase, TD-B3LYP/EFP1 predicts a red shift for the lowest singlet π→π* excitation energy in agreement with previous theoretical [33,39] and experimental [49,50] observations. The magnitude of the calculated solvent shift, -0.60 eV, is underestimated by 0.38 eV compared to the experimental value of -0.98 eV.

Table 2. Calculated and experimental solvent-induced shifts (in eV) for the π→π* charge-transfer excited state of *p*-nitroaniline.

π→π*	Experimental	Calculated
Gas phase	4.24[a]	3.97[c]
Condensed phase	3.26[b]	3.37[d]
Shift	-0.98	-0.60

[a](Ref. 48)
[b](Ref. 49,50)
[c]From an optimized B3LYP/DH(d,p) gas phase structure.
[d]From an average of 2000 snapshots of p-nitroaniline with 150 EFP1 water molecules during the QM/MM (B3LYP/EFP1) MD simulation

Approximately 70% of the error in the predicted solvent shift is due to the underestimation of the calculated gas phase value of the π→π* excitation energy. The error in the gas phase value is likely to be due to the charge-transfer nature of the lowest singlet π→π* excited state of *p*NA and the incorrect long-range behavior of the exchange functional used in the TDDFT calculation [80-82]. Intramolecular charge-transfer excitations using the B3LYP functional possess intermediate lambda values for *p*NA in the gas-phase, 0.593 for the lowest singlet π→π* charge-transfer excited state. In the condensed phase, the lambda value increases to 0.677. Improvement in the description of charge-transfer excited states in both the gas and condensed phase may be achieved by using, or increasing the amount of, non-local exchange as suggested in the literature [80].

Table 3 summarizes the density functional dependence of the calculated solvent shift. The CIS(D) calculated solvent-induced shift of Kosenkov and Slipchenko [33] is provided in Table 3 for comparison. The quality of the calculated solvent-shift improves slightly upon going from TD-B3LYP to TD-PBE, and more significantly when TD-CAM-B3LYP is employed. The improvement mirrors the amount of non-local (HF) exchange used in the description of the density functionals. The amount of HF exchange in B3LYP, PBE0, and CAM-B3LYP is 20%, 25%, and 19-65%, respectively. The range for CAM-B3LYP arises because this exchange functional is divided into a short-range (19% HF exchange) and a long-range (65 % HF exchange) term. The flexibility in the treatment of short-range and

long-range effects improves the TD-CAM-B3LYP description of charge-transfer and Rydberg excited states. The TD-CAM-B3LYP solvent shift, -0.90 eV, is in good agreement with the experimental solvent shift, -0.98 eV, and the CIS(D) calculated solvent shift, -1.00 eV, predicted by Kosenkov and Slipchenko [33].

Table 3. Comparison of calculated solvent-induced shifts (in eV) for the π→π* charge-transfer excited state of *p*-nitroaniline in water.

	Calculated			
π→π*	TD-B3LYP/ DH(d,p)	TD-PBE0/ DH(d,p)	TD-CAM-B3LYP/DH(d,p)	CIS(D)[g]
Gas phase	3.97[a]	4.11[c]	4.40[e]	4.65
Condensed phase	3.37[b]	3.44[d]	3.50[f]	3.65
Shift (condensed - gas)	-0.60	-0.67	-0.90	-1.00

[a]From an optimized gas phase structure obtained at the B3LYP/DH(d,p) level of theory.
[b]From an average of 2000 snapshots of p-nitroaniline with 150 EFP1 water molecules during the QM/MM (B3LYP/EFP1) MD simulation.
[c]From TD-PBE0/DH(d,p) calculation on an optimized gas phase structure obtained at the B3LYP/DH(d,p) level of theory.
[d]From an average of TD-PBE0-EFP1/DH(d,p) calculations performed on 2000 snapshots of p-nitroaniline with 150 EFP1 water molecules during the QM/MM (B3LYP/EFP1) MD simulation.
[e]From TD-CAM-B3LYP/DH(d,p) calculation on an optimized gas phase structure obtained at the B3LYP/DH(d,p) level of theory.
[f]From an average of TD-CAM-B3LYP-EFP1/DH(d,p) calculations performed on 2000 snapshots of p-nitroaniline with 150 EFP1 water molecules during the QM/MM (B3LYP/EFP1) MD simulation.
[g]Ref. 33

Contributions to the Solvent Shift

Solvatochromic shifts of vertical excitation energies may be caused by changes in the solute geometry due to solvation (solute relaxation) and specific solute-solvent interactions. In order to understand the contributions of the solute relaxation and solute-solvent interactions to the calculated solvent shift, the QM-EFP intermolecular interaction energy analysis of DeFusco *et al.* [83] is used to partition the predicted solvent shift into four terms: solute relaxation, Coulomb, polarization, and remainder. The solute relaxation energy is

defined as the contribution to the solvent shift from the changes in the solute geometry as a result of solvation. The Coulomb, polarization, and remainder terms correspond to the QM-EFP intermolecular interactions that are summarized in Eq. (1).

Figure 5. Contributions to the TD-B3LYP-EFP1/DH(d,p) solvent-induced shift of *p*-nitroaniline. Each energy term is obtained from an average of 2000 snapshots of *p*-nitroaniline with 150 EFP1 water molecules during the QM/MM (B3LYP/EFP1) MD simulation.

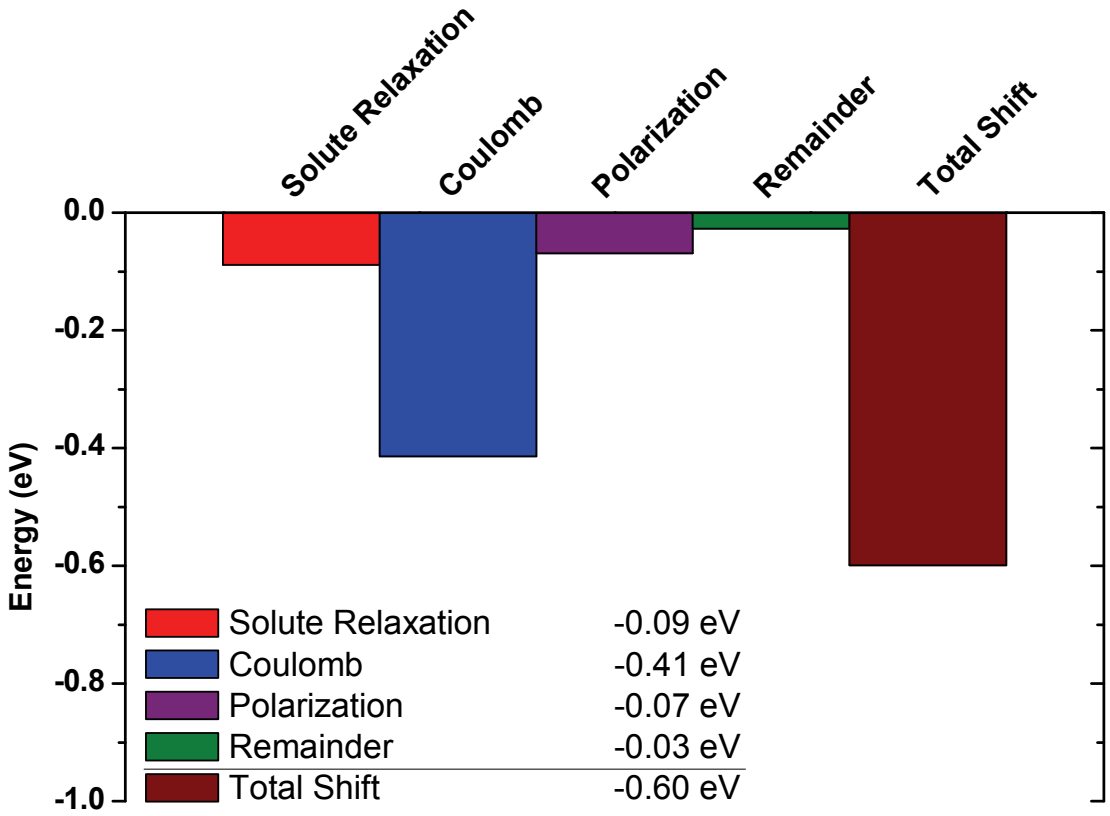

The energy decomposition for the TD-B3LYP/EFP1 calculated solvent-induced shift of the lowest singlet $\pi \rightarrow \pi^*$ charge-transfer excited state of *p*NA is illustrated in Figure 5. The largest contribution to the calculated red shift, ≈ 65% (-0.41 eV), comes from the Coulomb interactions between *p*NA and water. To explore the source of the large electrostatic contribution to the solvent-induced shift, consider the dipole moments summarized in Table 4. The Coulomb contribution can be interpreted in terms of the increase in dipole moment of *p*NA going from the gas phase to the condensed phase. This

dipole moment increase is about twice as large in the ground state (~8.6 D) as in the excited state (~4.5 D). This difference arises because the large zwitterionic charge separation in the excited state is ameliorated somewhat by the polar solvent [2,84]. In water, the stabilization of the increased dipole moment of *p*NA is likely achieved through hydrogen bonding. Indeed, on average, *p*NA is hydrogen bonded to three EFP1 water molecules. The second largest contribution to the calculated red shift, -0.09 eV ≈ 15%, is due to solute relaxation, reflecting the increase in zwitterionic character of the solvated geometry inferred from the calculated structural changes and partial atomic charges of *p*NA, listed in Table 1 and in Table 1S in the supporting information, respectively. The sum of the solute-solvent polarization interactions and remainder terms contribute the remaining -0.10 eV of the TD-B3LYP/EFP1 calculated solvent-shift.

Table 4. Calculated dipole moments (in Debye) of *p*-nitroaniline. Excited state values correspond to the lowest singlet $\pi \rightarrow \pi^*$ charge transfer state.

	Ground State	Excited State
Gas phase[a]	7.6	12.5
Condensed phase[b]	16.2	17.0

[a]From an optimized gas phase structure obtained at the B3LYP/DH(d,p) level of theory.
[b]From an average of 2000 snapshots of p-nitroaniline with 150 EFP1 water molecules during the QM/MM (B3LYP/EFP1) MD simulation

Table 5 summarizes the functional dependence of the contributions to the calculated solvent shift. Improving the functional results in increases in the solute relaxation and polarization contributions, whereas the Coulomb and remainder term are almost unchanged. Since the CAM-B3LYP functional is in excellent agreement with the experimental solvent shift, it is likely that one source of the poorer agreement between B3LYP and experiment is the inability of this functional to correctly capture the solute relaxation and polarization effects. The largest contribution to the calculated solvent shift is still from the Coulomb interaction between *p*NA and water, but these other two contributions are now comparable in

magnitude. The increase in the solute relaxation and polarization is likely due to an improved description of the singlet charge-transfer excited state.

Table 5. Contributions (eV) to the calculated solvent-induced shift of the lowest singlet π→π* charge-transfer excited state of *p*-nitroaniline in water. Each energy term is obtained from an average of 2000 snapshots of *p*-nitroaniline with 150 EFP1 water molecules during the QM/MM (B3LYP/EFP1) MD simulation.

Contribution	TD-B3LYP/DH(d,p)	TD-PBE0/DH(d,p)	TD-CAM-B3LYP/DH(d,p)
Solute Relaxation	-0.09	-0.12	-0.22
Coulomb	-0.41	-0.42	-0.39
Polarization	-0.07	-0.10	-0.26
Remainder	-0.03	-0.03	-0.03
Total Shift	-0.60	-0.67	-0.90

Performance of the TDDFT/EFP1 Method

To assess the accuracy and computational efficiency of the TD-DFT/EFP1 method, the lowest singlet π→π* charge-transfer excited state of a single snapshot from the QM/MM (B3LYP/EFP1) MD simulation of *p*NA with 150 EFP1 water molecules was calculated with the TD-B3LYP/EFP1 method and compared to a supermolecular TD-B3LYP calculation with the 150 EFP1 water molecules replaced with DFT waters. The calculations were performed on a Microsoft Windows® HPC Server 2008 R1 cluster consisting of dual 2.93 GHz quad core X5570 i7 (Nehalem) processors with 24 GB of memory per node interconnected by an Infiniband QDR, 8 Gbit/s, network. Table 6 summarizes the calculated π→π* vertical excitation energy, total wall clock time, and replicated memory requirements. The supermolecular TD-B3LYP singlet π→π* vertical excitation energy for *p*NA with 150 DFT water molecules is 3.33 eV, in excellent agreement with the TD-B3LYP/EFP1 value of 3.49 eV. Further, the total wall time for the TD-B3LYP/EFP1 calculation, 7.6 minutes, is three orders of magnitude smaller than the total wall time required for the supermolecular TD-B3LYP calculation, 25783.6 minutes. The computational efficiency of the TD-B3LYP/EFP1 method is further underscored by the replicated memory requirements, 57.9 megabytes for TD-B3LYP/EFP1 compared to 19.8 gigabytes for TD-B3LYP.

Table 6. Comparison of supermolecular TD-B3LYP/DH(d,p) and TD-B3LYP-EFP1/DH(d,p) values for a single QM/MM (B3LYP/EFP1) MD snapshot of *p*-nitroaniline with 150 waters. Calculations performed on a cluster consisting of dual 2.93 GHz quad core X5570 (Nehalem) nodes with 24 GB of memory per node interconnected by an Infiniband QDR (8 Gbit/s) network.

Single MD Snapshot (Figure 3)	TD-B3LYP/ DH(d,p) (150 DFT Waters)	TD-B3LYP-EFP1/ DH(d,p) (150 EFP1 Waters)
$\pi \rightarrow \pi^*$ Vertical Excitation Energy (eV)	3.33	3.49
Total Wall Clock Time (CPUs/Nodes)	25783.6 minutes (4/4)	7.6 minutes (4/4)
Replicated Memory	19.8 GB	57.9 MB

5. Conclusions

In this study the solvent-induced shift for the lowest singlet $\pi \rightarrow \pi^*$ charge-transfer excited state of *p*NA in water was investigated using the TD-DFT/EFP1 method. The condensed phase was modeled using QM/MM (B3LYP/EFP1) MD simulations with 150 EFP1/DFT water molecules. Upon going from the gas to the condensed phase in water, an increase in the zwitterionic character of the ground state geometry of *p*NA is predicted. The increase in zwitterionic character is reflected in the structural changes in the molecular framework and an increase in the dipole moment and charge separation of *p*NA in water.

The TD-B3LYP/EFP1 method reproduces the experimentally observed red shift in water. The largest contributions to the calculated solvent shift are from solute-solvent electrostatic interactions and solute relaxation reflecting the observed increase in dipole moment and zwitterionic character of *p*NA.

The discrepancy between the calculated and experimental solvent shift is due in part to the error in the calculated gas phase vertical excitation energy for the lowest singlet $\pi \rightarrow \pi^*$ charge-transfer excited state of *p*NA. However, the TD-B3LYP/EFP1 calculated condensed phase vertical excitation energy of the charge-transfer excited state agrees with experiment [48-50] to within ≈ 0.1 eV. Using a density functional with an improved description of long-range effects, an improvement in the calculated solvent shift is obtained.

For a single snapshot, the TD-B3LYP/EFP1 method reproduces the supermolecular TD-B3LYP value of the singlet $\pi \rightarrow \pi^*$ charge-transfer excitation energy of *p*NA with 150 water molecules to within ≈ 0.16 eV with a 3000-fold decrease in the total wall clock time.

The TD-DFT/EFP1 method is shown to be an accurate and efficient discrete approach to modeling environmental effects for the study of optical properties of organic chromophores in aqueous media.

Acknowledgements

This work was supported by a grant from the Air Force Office of Scientific Research and by a grant from the Microsoft Corporation. Supermolecular TD-B3LYP calculations were performed on the Rhiannon cluster located at the Microsoft® Enterprise Engineering Center (EEC) in Redmond, WA. The authors thank Microsoft® for computational resources, Dr. Albert DeFusco for many helpful discussions, and Mr. Leo C. DeSesso for invaluable assistance in reviewing and editing the manuscript.

Supporting Information

Table 1S. Ground state gas- (B3LYP/DH(d,p)) and condensed-phase (B3LYP-EFP1/DH(d,p)) calculated geodesic potential derived charge (electron) on the amino and nitro group of *p*-nitroaniline (see Figure 1).

	Charge					
	N_9	H_{10}	H_{11}	N_{14}	O_{15}	O_{16}
Gas phase	-0.64	0.32	0.32	0.58	-0.40	-0.40
Condensed phase	-1.02	0.54	0.54	0.65	-0.56	-0.56

References

1. *Theory and Applications of Computational Chemistry: The First Forty Years*; Dykstra, C. E., Frenking, G., Kim, K. S., Scuseria, G. E., Eds.; Elsevier, Amsterdam, **2005**.
2. Reichardt, C. *Solvents and Solvent Effects in Organic Chemistry*, 3rd Ed., Wiley-VCH, Weinheim, **2003**.
3. *Solvation Effects in Molecules and Biomolecules: Computational Methods and Applications*; Canuto, S., Eds.; Springer, **2008**.
4. Chiba, M.; Federov, D. G.; Kitaura, K. The Fragment Molecular Orbital-Based Time-Dependent Density Functional Theory for Excited States in Large Systems. In *The Fragment Molecular Orbital Method: Practical Applications to Large Molecular Systems*; Federov, D. G., Kitaura, K., Eds.; CRC Press, Boca Raton, Fl., **2009**; pp. 91-118.
5. *Continuum Solvation Models in Chemical Physics: From Theory to Applications*; Mennucci, B., Cammi, R., Eds.; Wiley, Hoboken, **2007**.

6. Santoro, F.; Barone, V.; Gustavsson, T.; Improta, R. *J. Am. Chem. Soc.* **2006**, 128, 16312-16322.
7. Improta, R.; Barone, V. *J. Mol. Struct.: THEOCHEM* **2009**, 914, 87-93.
8. Besley, N. A.; Hirst, J. D. *J. Am. Chem. Soc.* **1999**, 121, 8559-8566.
9. Tomasi, J.; Mennucci, B.; Cammi, R. *Chem. Rev.* **2005**, 105, 2999-3093.
10. Warshell, A.; Levitt, M. *J. Mol. Biol.* **1976**, 103, 227-249.
11. Singh, U. C.; Kollman, P. A. *J. Comput. Chem.* **1986**, 7, 718-730.
12. Field, M. J.; Bash, P. A.; Karplus, M. *J. Comput. Chem.* **1990**, 11, 700-733.
13. Gao, J.; Luque, F. J.; Orozco, M. *J. Chem. Phys.* **1993**, 98, 2975-2982.
14. Gao, J. Methods and Applications of Combined Quantum Mechanical and Molecular Mechanical Potentials. In *Reviews in Computational Chemistry*, Vol. 7, Lipkowitz, K. B., Boyd, D. B., Eds.; Wiley-VCH, Weinheim, **1995**, pp. 119-185.
15. Coutinho, K.; Rivelino, R.; Georg, H. C.; Canuto, S. The Sequential QM/MM Method and Its Application to Solvent Effects in Electronic and Structural Properties of Solutes. In *Solvation Effects in Molecules and Biomolecules: Computational Methods and Applications*; Cantuo, S., Eds.; Springer, **2008**, pp. 159-189.
16. Day, P. N.; Jensen, J. H.; Gordon, M. S.; Webb, S. P.; Stevens, W. J.; Krauss, M.; Garmer, D.; Basch, H.; Cohen, D. *J. Chem. Phys.* **1996**, 105, 1968-1986.
17. Adamovic, I.; Freitag, M. A.; Gordon, M. S. *J. Chem. Phys.* **2003**, 118, 6725-6732.
18. Gordon, M. S.; Freitag, M. A.; Bandyopadhyay, P.; Jensen, J. H.; Kairys, V.; Stevens, W. J. *J. Phys. Chem. A* **2001**, 105, 293-307.
19. Adamovic, I.; Gordon, M. S. *J. Phys. Chem. A* **2005**, 109, 1629-1636
20. Gordon, M. S.; Slipchenko, L.; Li, H.; Jensen, J. H. *Annu. Rep. Comput. Chem.* **2007**, 3, 177-193.
21. Merrill, G. N.; Gordon, M. S. *J. Phys. Chem. A* **1998**, 102, 2650-2657.
22. Day, P. N.; Pachter, R.; Gordon, M. S.; Merrill, G. N. *J. Chem. Phys.* **2000**, 112, 2063-2073.
23. Netzloff, H. M.; Gordon, M. S. *J. Chem. Phys.* **2004**, 121, 2711-2714.
24. Kemp, D. D.; Gordon, M. S. *J. Phys. Chem. A* **2008**, 112, 4885-4894.
25. Chen, W.; Gordon, M. S. *J. Chem. Phys.* **1996**, 105, 11081-11090.
26. Webb, S. P.; Gordon, M. S. *J. Phys. Chem. A* **1999**, 103, 1265-1273.
27. Krauss, M. *Computers & Chem.* **1994**, 19, 33-38.
28. Krauss, M.; Webb, S. P. *J. Chem. Phys.* **1997**, 107, 5771-5775.
29. Krauss, M.; Wladowski, B. D. *Int. J. Quantum Chem.* **1998**, 69, 11-19.
30. Minikis, R. M.; Kairys, V.; Jensen, J. H. *J. Phys. Chem. A*, **2001**, 105, 3829-3837.
31. Arora, P.; Slipchenko, L. V.; Webb, S. P.; DeFusco, A.; Gordon, M. S. *J. Phys. Chem. A* **2010**, 114, 6742-6750.
32. Slipchenko, L. V. *J. Phys. Chem. A* **2010**, 114, 8824-8830.
33. Kosenkov, D.; Slipchenko, L. V. *J. Phys. Chem. A* **2011**, 115, 392-401.
34. Yoo, S.; Zahariev, F.; Sok, S.; Gordon, M. S. *J. Chem. Phys.* **2008**, 129, 144112-1-144112-8.
35. Minezawa, N.; Silva, N. D.; Zahariev, F.; Gordon, M. S. *J. Chem. Phys.* **2011**, 134, 054111-1-054111-12.
36. Benjamin, I. *Chem. Phys. Lett.* **1998**, 287, 480-486.
37. Sinha, H. K.; Yates, K. *Can. J. Chem.* **1991**, 69, 550-557.

38. Sinha, H. K.; Yates, K. *J. Am. Chem. Soc.* **1991**, 113, 6062-6067.
39. Farztdinov, V. M.; Schanz, R.; Kovalenko, S. A.; Ernsting, N. P. *J. Phys. Chem. A* **2000**, 104, 11486-11496.
40. Sim, F.; Chin, S.; Dupuis, M.; Rice, J. E. *J. Phys. Chem.* **1993**, 97, 1158-1163.
41. Scalmani, G.; Frisch, M. J.; Mennucci, B.; Tomasi, J.; Cammi, R.; Barone, V. *J. Chem. Phys.* **2006**, 124, 094107-1-094107-15.
42. Das, G. P.; Dudis, D. S. *J. Phys. Chem. A* **2000**, 104, 4767-4771.
43. Moran, A. M.; Kelley, A. M.; Tretiak, S. *Chem. Phys. Lett.* **2003**, 367, 293-307.
44. Cammi, R.; Frediani, L.; Mennucci, B.; Ruud, K. *J. Chem. Phys.* **2003**, 119, 5818-5827.
45. Rashid, A. N. *J. Mol. Struct.* **2004**, 681, 57-63.
46. Wang, C.-K.; Wang, Y.-H. *J. Chem. Phys.* **2005**, 119, 4409-4412.
47. Moran, A. M.; Kelley, A. M. *J. Chem. Phys.* **2001**, 115, 912-924.
48. Millefiori, S.; Favini, G.; Millefiori, A.; Grasso, D. *Spectrochim. Acta* **1977**, 33A, 21-27.
49. Thomsen, C. L.; Thøgersen, J.; Keiding, S. R. *J. Phys. Chem. A* **1998**, 102, 1062-1067.
50. Kovalenko, S. A.; Schanz, R.; Farztdinov, V. M.; Hennig, H.; Ernsting, N. P. *Chem. Phys. Lett.* **2000**, 323, 312-322.
51. Trueblood, K. N.; Goldfish, E.; Donohue, J. *Acta Crystallogr.* **1961**, 14, 1009-1017.
52. Breitung, E. M.; Vaughan, W. E.; McMahon, R. J. *Rev. Sci. Instrum.* **2000**, 71, 224-227.
53. Arnett, E. M.; Hufford, D.; McKelvey, D. R. *J. Am. Chem. Soc.* **1966**, 88, 3142-3143.
54. Kaatz, P.; Shelton, D. P. *J. Chem. Phys.* **1996**, 105, 3918-3929.
55. Runge, E.; Gross, E. K. U. *Phys. Rev. Lett.* **1984**, 52, 997-1000.
56. Gross, E. K. U.; Kohn, W. *Adv. Quantum. Chem.* **1990**, 21, 255-291.
57. van Leeuwen, R. *Int. J. Mod. Phys. B* **2001**, 15, 1969-2023.
58. Casida, M. E., Time-dependent density-functional response theory for molecules. In *Recent Advances in Density Functional Methods*, Chong, D. P. Eds.; Recent Advances in Computational Chemistry; World Scientific: Singapore, 1995; 1, pp. 155-192.
59. Casida, M. E., Time-Dependent Density Functional Response Theory of Molecular Systems: Theory, Computational Methods, and Functionals. In *Recent Developments and Applications of Modern Density Functional Theory, Theoretical and Computational Chemistry*, Seminario, J. M. Eds.; Elsevier: Amsterdam, 1996, pp. 391-439.
60. Hirata, S.; Head-Gordon, M. *Chem. Phys. Lett.* **1999**, 314, 291-299.
61. Martyna, G. J.; Tuckerman, M. E.; Tobias, D. J.; Klein, M. L. *Mol. Phys.* **1996**, 87, 1117-1157.
62. Becke, A. D. *J. Chem. Phys* **1993**, 98, 5648-5652.
63. Lee, C.; Yang, W.; Parr, G. R. *Phys. Rev. B* **1988**, 37, 785-789.
64. Stephens, P. J.; Devlin, F. J.; Chadalowski, C. F.; Frisch, M. J. *J. Phys. Chem.* **1994**, 98, 11623-11627.
65. Dunning, T. H. Jr.; Hay, P. J. Gaussian Basis Sets for Molecular Calculations. In *Methods of Electronic Structure Theory*; Vol. 3, Schaefer, H. F. III, Eds.; Plenum, New York, **1977** ; pp. 1-27.
66. Perdew, J. P.; Burke, K.; Ernzerhof, M. *Phys. Rev. Lett.* **1996**, 77, 3865-3868.
67. Adamo, C.; Barone, V. *J. Chem. Phys.* **1999**, 110, 6158-6170.

68. Yanai, T.; Tew, D. P.; Handy, N. C. *Chem. Phys. Lett.* **2004**, 393, 51-57.
69. Murray, C. W.; Handy, N. C.; Laming, G. J. *Mol. Phys.* **1993**, 78, 997-101.
70. Lebedev, V. I.; Laikov, D. N. *Dokl. Math.* **1999**, 59, 477-481.
71. Peach, M. J. G.; Benfield, P.; Helgaker, T.; Tozer, D. J. *J. Chem. Phys.* **2008**, 128, 044118-1-044118-8.
72. Peach, M. J. G.; Sueur, C. R. L.; Ruud, K.; Guillaume, M.; Tozer, D. J. *Phys. Chem. Chem. Phys.* **2009**, 11, 4465-4470.
73. Peach, M. J. G.; Tozer, D. J. *J. Mol. Struct.: THEOCHEM* **2009**, 914, 110-114.
74. Wiggins, P.; Williams, J. A. G.; Tozer, D, J. *J. Chem. Phys.* **2009**, 131, 091101-1-091101-4.
75. Dwyer, A. D.; Tozer, D. J. *Phys. Chem. Chem. Phys.* **2010**, 12, 2816-2818.
76. Plötner, J.; Tozer, D. J.; Dreuw, A. *J. Chem. Theory Comput.* **2010**, 6, 2315-2324.
77. Spackman, M. A. *J. Comput. Chem.* **1996**, 17, 1-18.
78. Gordon, M. S.; Schmidt, M. W. Advances in Electronic Structure Theory: GAMESS: A Decade Later. In *Theory and Applications of Computational Chemistry: The First Forty Years*; Dykstra, C. E., Frenking, G., Kim, K. S., Scuseria, G. E., Eds.; Elsevier, Amsterdam, **2005**; pp. 1167-1189.
79. Bode, B. M.; Gordon, M. S. *J. Mol. Graphics Mod.* **1998**, 16, 133-138.
80. Dreuw, A.; Weisman, J. L.; Head-Gordon, M. *J. Chem. Phys.* **2003**, 119, 2943-2946.
81. Zhao, Y.; Truhlar, D. G. *J. Phys. Chem. A* **2006**, 110, 13126-13130.
82. Autschbach, J. *Chem. Phys. Chem.* **2009**, 10, 1757-1760.
83. Defusco, A.; Ivanic, J.; Schmidt, M. W.; Gordon, M. S. *J. Phys. Chem. A* **2011**, 115, 4574-4582.
84. Bandyopadhyay, P.; Gordon, M. S.; Mennucci, B.; Tomasi, J. *J. Chem. Phys.* **2002**, 116, 5023-5032.

CHAPTER 4. BENCHMARKING THE PERFORMANCE OF TIME-DEPENDENT DENSITY FUNCTIONAL METHODS

A paper to be submitted to *The Journal of Chemical Physics*

Sarom Sok[†], Federico Zahariev[†], Soohaeng Yoo[‡], Mark S. Gordon[†]

Abstract

The performance of 24 density functionals, including 14 meta-generalized gradient approximation (meta-GGA) functionals, is assessed for the calculation of vertically excited states against an experimental benchmark set comprising 14 small- to medium-sized compounds with 101 total excited-states. The experimental benchmark set consists of singlet, triplet, valence, and Rydberg excited states. The global-hybrid (GH) GGA version of the Perdew-Burke-Ernzerhoff (PBE0) exchange-correlation functional is found to offer the best overall performance with a mean absolute error (MAE) of 0.28 eV. The GH Minnesota 2006 density functional with 54% Hartree-Fock exchange (M06-2X) gave a lower MAE of 0.26 eV, but this functional encounters some convergence problems in the ground state. The local density approximation functional consisting of the Slater exchange and Volk-Wilk-Nusair correlation functional (SVWN) outperformed all non-GH GGAs tested. The best pure density functional performance is obtained with the local version of the Minnesota 2006 density functional (M06-L) with an MAE of 0.41 eV.

1. Introduction

Time-dependent density functional theory (TDDFT) [1-5] is a computationally attractive alternative approach [6] to highly correlated single-reference *ab initio* methods, e.g., equations-of-motion coupled-cluster, for the calculation of excited states of large molecules. Most implementations of TDDFT utilize the adiabatic approximation where, in the limit of a slowly varying electron density, ground-state density functionals are used in the calculation of the time-dependent exchange-correlation potential. As a result, many

[†] Department of Chemistry and Ames Laboratory, Iowa State University, Ames, IA 50011-3111
[‡] Chemical and Materials Science Division, Pacific Northwest National Laboratory, Richland, WA 99352

applications in the literature employ either the popular global-hybrid (GH) generalized-gradient approximation (GGA) B3LYP functional [7-9]or the GH version of the Perdew-Burke-Ernzerhoff (PBE0) exchange-correlation functional [10-12]. With the maturity of density functional theory (DFT) for the ground state, many new and more sophisticated density functionals have been [13-25] and continue to be developed [26]. Further, with the aid of automatic code generators [27], these sophisticated density functionals can be integrated into excited-state TDDFT codes. However, without a systematic approach towards improving the description of ground state density functionals, it is unclear if the progression towards more sophisticated density functionals (climbing up Jacob's ladder [28]) in the ground state necessarily correlates with an improved description in the excited state.

Several benchmark studies [29-42] have explored the performance of using ground-state density functionals within the adiabatic approximation for the calculation of vertically excited states using TDDFT. The scope of the previous benchmark studies has been limited to either valence [40,42,34] or singlet [39] excited states with very few benchmarks considering triplet [32,33] and Rydberg excited states. Furthermore, the approach taken with previous benchmark studies is to perform ground state geometry optimizations using a single level of theory (PBE0 functional or Møller Plesset second-order perturbation theory) followed by vertical excited-state calculations with varying density functionals. However, in practice, the ground-state density functionals used in the TDDFT vertical excited state calculations are also employed in the optimization of the ground state geometry. At minimum, ground state density functionals should be able to describe ground state properties, such as geometries. In addition, very few benchmark studies have investigated the performance of meta-GGA density functionals for the calculation of vertical excitation energies with TDDFT [29-31,37,41]. A benchmark assessing the performance of density functionals comprising recently developed meta-GGA functionals for the vertical excitation energy calculation of singlet, triplet, valence, and Rydberg excited states using TDDFT is therefore very desirable.

In the current study, the performance of 24 density functionals listed in Table 1, including 14 meta-GGA density functionals, is assessed for the calculation of vertically excited states within the TDDFT formalism against a benchmark set consisting of 14 small-

to medium-sized compounds with 101 total experimental excited state energies. The excited state benchmark set consists of 63 singlet and 38 triplet states. The benchmark set can also be broken down into 60 valence and 41 Rydberg states. Of the 60 valence states, 30 are $\pi\rightarrow\pi^*$, 26 are $n\rightarrow\pi^*$, 3 are $n\rightarrow\sigma^*$, and 1 is $\sigma\rightarrow\pi^*$ in nature.

Table 1. List of density functionals used in this work.

Functional	Year	Type	% HF EXCH	References
SVWN	1980	LDA		[99,100]
BLYP	1988	GGA		[101,102]
PW91	1992	GGA		[103,104]
PBE	1997	GGA		[10,11]
OLYP	2001	GGA		[102,105]
BHHLYP	1993	GH-GGA	50	[106]
B3LYP	1994	GH-GGA	20	[4,8]
PBE0	1997	GH-GGA	25	[10,11,12]
X3LYP	2004	GH-GGA	21.8	[4,102,104,107]
CAM-B3LYP	2004	RSH-GGA or RSH	19 – 65	[108]
VS98	1998	mGGA		[13]
PKZB	1999	mGGA		[14]
TPSS	2004	mGGA		[15,16]
M06-L	2006	mGGA		[17]
TPSSm	2007	mGGA		[18]
revTPSS	2009	mGGA		[19]
TPSSh	2004	GH-mGGA	10	[20]
M05	2005	GH-mGGA	28	[22]
M05-2X	2006	GH-mGGA	56	[23]
M06	2006	GH-mGGA	27	[24]
M06-2X	2006	GH-mGGA	54	[24]
M06-HF	2006	GH-mGGA	100	[25]
M08-HX	2008	GH-mGGA	52.23	[26]
M08-SO	2008	GH-mGGA	56.79	[26]

The structure of the paper is as follows. The computational methods employed in the benchmark study are detailed in Section 2. The results and discussion of the general trends of the benchmark calculations are covered in Section 3 and concluding remarks and recommendations for density functional usage are given in Section 4.

2. Computational Methods

Linear Response Time-dependent Density Functional Theory

The linear response formulation of the TDDFT equations is used for the calculation of vertical excited states [4,5],

$$\begin{bmatrix} \mathbf{A} & \mathbf{B} \\ \mathbf{B} & \mathbf{A} \end{bmatrix} \begin{bmatrix} \mathbf{X} \\ \mathbf{Y} \end{bmatrix} = \omega \begin{bmatrix} 1 & 0 \\ 0 & -1 \end{bmatrix} \begin{bmatrix} \mathbf{X} \\ \mathbf{Y} \end{bmatrix} \tag{1}$$

Solutions to the non-Hermitian eigenvalue problem in Eq. (1) yields the transition energy, ω, and the corresponding bi-orthonormal transition vectors $\mathbf{X}$ and $\mathbf{Y}$. The matrices $\mathbf{A}$ and $\mathbf{B}$ in Eq. (1) are defined as,

$$A_{ia\mu,jb\nu} = \delta_{ij}\delta_{ab}\delta_{\mu\nu}\left(\varepsilon_a - \varepsilon_i\right) + K_{ia\mu,jb\nu} \tag{2}$$

and,

$$B_{ia\mu,jb\nu} = K_{ia\mu,bj\nu} \tag{3}$$

where the indices i, j and a, b label occupied and virtual orbitals, respectively, while the indices μ, ν denote spin. ε_a and ε_i are orbital energies for Kohn-Sham orbitals ϕ_a and ϕ_i, respectively. The coupling matrix [43] $K_{ia\mu,jb\nu}$ is given by,

$$K_{ia\mu,jb\nu} = \iint \phi^*_{i\mu}(\mathbf{r})\phi_{a\mu}(\mathbf{r})\left(\frac{1}{|\mathbf{r}-\mathbf{r}'|} + \frac{\delta^2 E_{\mathrm{xc}}}{\delta\rho_\mu(\mathbf{r})\delta\rho_\nu(\mathbf{r}')}\right)\phi_{j\nu}(\mathbf{r}')\phi^*_{b\nu}(\mathbf{r}')\,d\mathbf{r}d\mathbf{r}' \tag{4}$$

where E_{xc} is the exchange-correlation energy. ρ_μ and ρ_ν are electron spin densities.

Within the adiabatic approximation the exchange-correlation energy is defined as,

$$E_{xc} = \int f\left(\rho_\mu, \rho_\nu, \gamma_{\mu\mu}, \gamma_{\mu\nu}, \gamma_{\nu\nu}, \tau_\mu, \tau_\nu\right) \tag{5}$$

where f is the ground state exchange-correlation functional. The density gradient invariants, γ, are defined as,

$$\gamma_{\mu\mu} = \nabla\rho_\mu \cdot \nabla\rho_\mu, \qquad \gamma_{\mu\nu} = \nabla\rho_\mu \cdot \nabla\rho_\nu, \qquad \gamma_{\nu\nu} = \nabla\rho_\nu \cdot \nabla\rho_\nu, \tag{6}$$

and

$$\tau_\sigma(\mathbf{r}) = \sum_i^{\text{occupied}} \frac{1}{2}|\nabla\phi_{i\sigma}(\mathbf{r})|^2 \tag{7}$$

is the kinetic energy density for the occupied Kohn-Sham orbital $\phi_{i\sigma}$ of spin σ. The classification of density functionals is as follows. Local density approximation (LDA) exchange-correlation functionals are dependent only on the electron spin densities. Generalized gradient approximation (GGA) exchange-correlation functionals are dependent on both the electron spin densities and the density gradient invariant. Density functionals that depend on the electron spin densities, density gradient invariant, and kinetic energy density define the meta-generalized gradient approximation (mGGA). Density functionals that include a fixed amount of Hartree-Fock (HF) exchange are identified as global hybrid (GH) density functionals. Density functionals with varying amounts of HF exchange at different interatomic distances are labeled as range separated hybrid (RSH) density functionals. Pure density functionals do not make use of HF exchange and avoid the calculation of the two electron exchange integrals. As a result, pure density functionals are computationally more efficient.

The density functionals studied in the current benchmark study are listed in Table 1. The molecules and excited states in the benchmark set are given in Table S3 of the Supporting Information section.

All ground-state molecular structures have been optimized with the Pople split-valence triple-ζ 6-311++G(3df,3pd) basis set [44-48] with the same density functional that is used for the calculation of the vertical excitation energies. Ground-state structures were characterized by a positive definite Hessian matrix (second derivative matrix of the energy with respect to the nuclear coordinates). Vertical excitation calculations were performed from the optimized ground-state geometry for the lowest 15 singlet and triplet excited states for each molecule using the linear response TDDFT implementation [49]. The vertical excited state symmetry labels, oscillator strengths, and lambda diagnostic values were used to identify valence states for comparisons with experiment. Identification of Rydberg states was accomplished by analyses of the linear-combination of atomic orbital (LCAO) coefficients of the Kohn-Sham molecular orbitals that contribute to the dominant transition vectors of an excited state. In some cases, visualization of the Kohn-Sham molecular orbitals assisted in the identification of excited states. Both ground state DFT and excited state

TDDFT calculations were carried out using the (96, 1202) Euler-MacLaurin radial [50] and Lebedev angular [51] grid.

Lambda Diagnostic

The lambda diagnostic of Peach *et al.* [52] quantifies the degree of orbital overlap between occupied-virtual pairs (transition vectors) contributing to an excited state. Lambda, Λ, is calculated as the sum of spatial overlaps, O_{ia}, between transition vectors involved in an excited state weighted by the square of the transition amplitude κ_{ia},

$$\Lambda = \frac{\sum_{ia} \kappa_{ia}^2 O_{ia}}{\sum_{ia} \kappa_{ia}^2} \tag{8}$$

where the spatial overlap is given as the inner product of the moduli of occupied and virtual Kohn-Sham orbitals, ϕ_i and ϕ_a,

$$O_{ia} = \left\langle |\phi_i||\phi_a| \right\rangle = \int |\phi_i(\mathbf{r})||\phi_a(\mathbf{r})| d\mathbf{r} \tag{9}$$

and,

$$\kappa_{ia} = \mathbf{X}_{ia} + \mathbf{Y}_{ia} \tag{10}$$

where X and Y are the transition vectors defined in Eq. (1). Lambda values range from 0 to 1 with small lambda values indicating low-overlap/long-range excitations (i.e. Rydberg excited states) and large lambda values signifying high-overlap/short-range excitations (i.e. low-lying valence excited states). Several studies have demonstrated errors in calculated excitation energies for small lambda values and large long-range character [35,52-56].

The mean signed error (MSE), mean absolute error (MAE) and root-mean-square (RMS) error with respect to experimental values are used as estimators of density functional performance for vertically excited states. All calculations were performed using the General Atomic and Molecular Electronic Structure System (GAMESS) quantum chemistry code [57] and visualized using MacMolPlt [58].

3. Results and Discussions

In light of the numerous detailed theoretical studies [59-95] that are available in the literature for the various molecules used in the current benchmark set, the analysis of density

functional performance for vertical excited states will be focused on the general trends. The calculated errors in vertical excitation energies and statistical results obtained for each molecule and density functional in the benchmark are available in the Supporting Information.

The total number of excited states examined for LDA, GGA, GH-GGA, and RSH functionals is 101, the entire benchmark set. However, due to convergence issues in the ground state geometry optimization, the number of excited states examined for the mGGA and GH-mGGA functionals is 60. Switching to a smaller basis and removing diffuse functions resolved the convergence problem but was not pursued as a viable solution due to the improper treatment of Rydberg states. Instead, molecules with convergence problems were removed from the benchmark set for the mGGA and GH-mGGA functionals.

Performance for Singlet and Triplet Excited States

The benchmark set of 101 excited states can be broken down into 63 singlet and 38 triplet states. Figure 1 shows a graphical representation of the MAE for singlet and triplet excited states, as well as the overall MAE for the benchmark set. The corresponding data to Figure 1 is summarized in Tables S4 and S5 in the Supporting Information section.

For singlet excited states, the PBE0 (MAE = 0.25 eV) functional offers the best performance among LDA, GGAs, and GH-GGAs. The CAM-B3LYP (MAE = 0.28 eV) functional is nearly equivalent in performance. OLYP (MAE = 0.89 eV) gives the poorest performance among the LDA, GGA, and GH-GGA functionals. Among the mGGA and GH-mGGA functionals, the M06-2X (MAE = 0.21 eV) and M06 (MAE = 0.81 eV) functionals offer the best and worst performance, respectively, for singlet vertical excited states. Surprisingly, the SVWN functional (MAE = 0.56 eV), an LDA, outperforms all GGAs as well as a few mGGAs (M06, PKZB, TPSSm) for singlet excited states. The performance of the SVWN functional suggests that, for the singlet excited states within the benchmark set of the current study, climbing up Jacob's ladder in the ground state may not necessarily correspond to an improved performance in the excited state [28].

Figure 1. Comparison of density functional mean absolute errors (MAE) for singlet and triplet excited states.

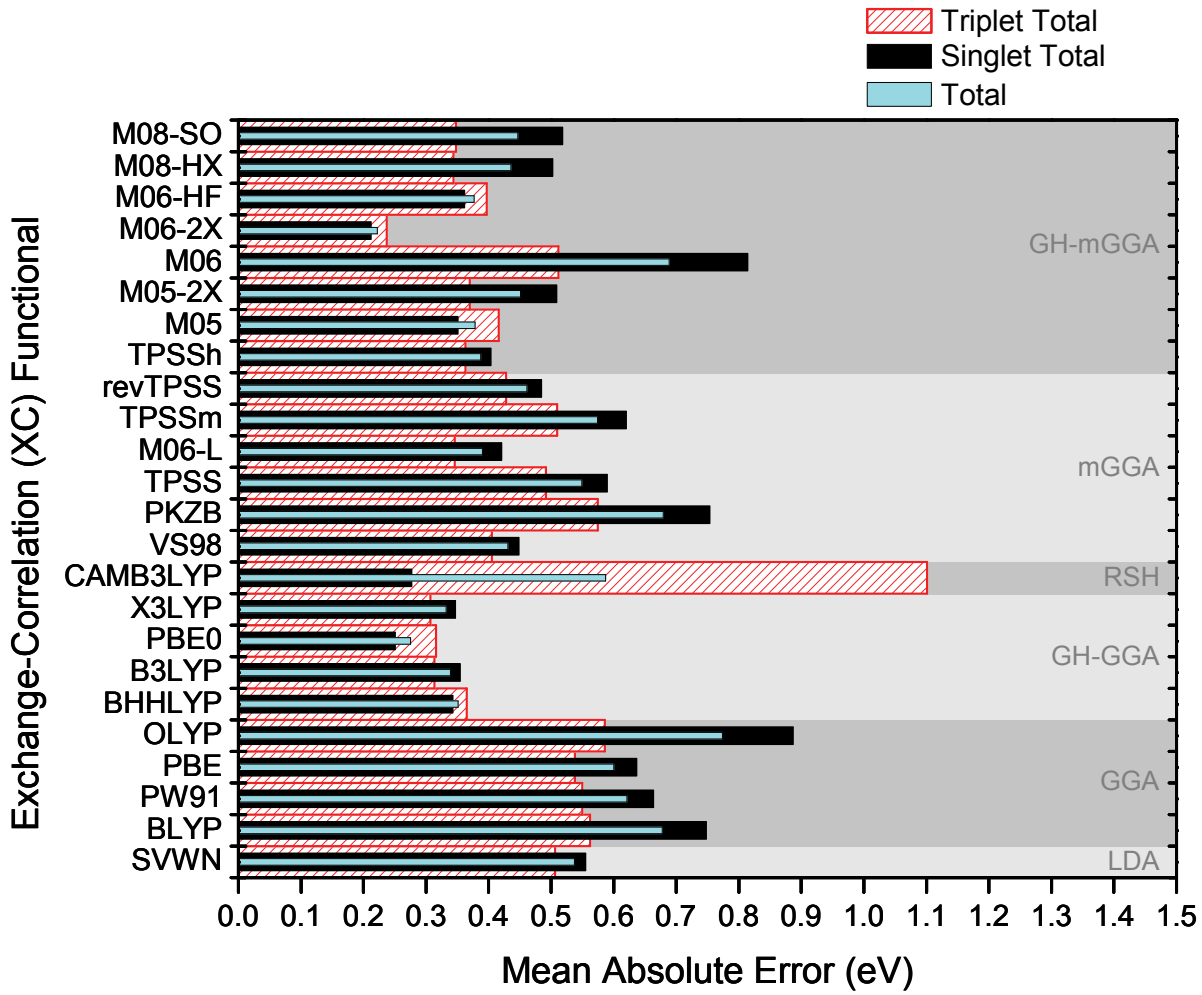

For triplet excited states, the B3LYP (MAE = 0.31 eV) , X3LYP (MAE = 0.31 eV), and PBE0 (MAE = 0.32 eV) functionals offer the best performance among LDA, GGAs, and GH-GGAs. Between mGGAs and GH-mGGAs, the M06-2X (MAE = 0.24 eV) demonstrates the best performance for triplet excited states while the PKZB (MAE = 0.57 eV) functional gives the worst. The SVWN functional (MAE = 0.51 eV) continues to outperform all GGAs. With the exception of the CAM-B3LYP (MAE = 1.10 eV) functional, the errors associated with triplet excited states are near or below the errors for singlet excited states. These results from the triplet excited states are different from the work of Jacquemin *et al.* [33], which suggests MAE values larger than 0.40 eV for PBE0 and B3LYP. The

discrepancy between the results of the current study and the work of Jacquemin *et al.* may be due to the nature of the benchmark set used. In the current study, reference data points are obtained from experiment while wavefunction-based data is used in the work of Jacquemin *et al.* In agreement with the Jacquemin *et al.* study, the M06-2X functional performs best overall and the CAM-B3LYP performs the worst for triplet states.

Performance for Valence and Rydberg Excited States

The benchmark set can also be divided into 60 valence and 41 Rydberg states. Figure 2 shows a graphical representation of the MAE for valence and Rydberg excited states compared to the overall MAE for the benchmark set. The corresponding data is summarized in Tables S6 and S7 in the Supporting Information section. For valence excited states, the B3LYP (MAE = 0.26 eV), X3LYP (MAE = 0.26 eV), and PBE0 (MAE = 0.30 eV) functionals continue to give the best overall performances among LDA, GGA, and GH-GGA functionals. The CAM-B3LYP (MAE = 0.84 eV) functional performs the worst among LDA, GGA, and GH-GGA functionals. The SVWN (MAE = 0.48 eV) functional and all GGA functionals perform at the same level for valence excited states. Between mGGA and GH-mGGA the M06 (MAE = 0.25 eV) functional offers the best performance. The worst performing density functional among the mGGA and GH-mGGA functionals is the M06-HF (MAE = 0.48 eV) functional, consisting of 100% HF exchange. The M06-L (MAE = 0.29 eV) functional, which contains no HF exchange, is the second best performing density functional among the mGGA and GH-mGGA functionals for vertically excited valence states. The latter result suggests that the addition of too much HF exchange can have a detrimental impact on the performance of density functionals for the vertical excitation energy calculation of low-lying valence states.

Figure 2. Comparison of density functional mean absolute errors (MAE) for valence and Rydberg excited states.

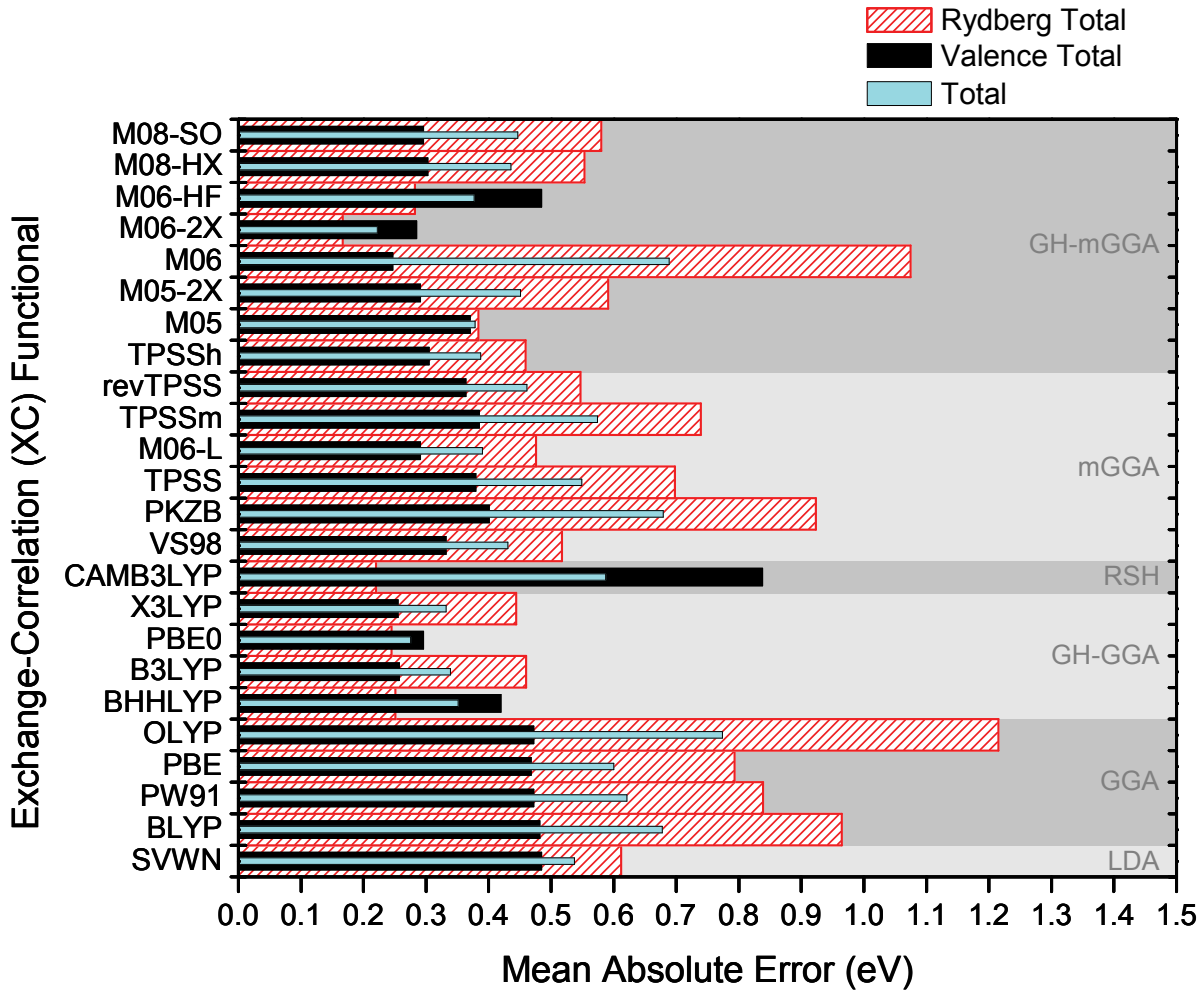

For Rydberg states, the CAM-B3LYP (MAE = 0.22 eV) functional offers the best performance among LDA, GGAs, and GH-GGAs. The SVWN (MAE = 0.61 eV) density functional performs better than all GGA functionals for Rydberg states, and the OLYP (MAE = 1.21 eV) functional performs the worst among LDA, GGA, and GH-GGA functionals. Among the mGGAs and GH-mGGAs, density functionals with large amounts of HF exchange give the best performance for Rydberg states. The best performing functional for valence states, M06, is the worst performing functional for Rydberg states. Similarly, the worst performing functional for valence states, M06-HF, is within 0.08 eV of the best

performing density functional between mGGAs and GH-mGGAs for Rydberg states, M06-2X (MAE = 0.17 eV). An accurate description of the exchange-correlation potential at long-range, facilitated through the inclusion of HF exchange, is essential for the proper treatment of Rydberg excited states.

Possessing a balanced description of valence and Rydberg excited states is a desirable trait for density functionals with respect to the calculation of vertical excitation energies. The trends mentioned above for valence and Rydberg excited states are visualized using the lambda diagnostic of Peach *et al*. [52]. Figure 4 plots lambda values against errors in TDDFT calculated vertical excitations for LDA, GGAs, and GH-GGAs. Similarly, Figure 5 plots the lambda diagnostic for mGGAs and GH-mGGAs. For all density functionals, Rydberg excited states are associated with lambda values less than 0.6 while valence excited states produce lambda values varying from 0.2 to 0.9. Observed for all density functionals is the trend towards negative errors with decreasing lambda values. The best performing density functionals possess lambda plots with data points clustered near the origin at y=0 for both valence and Rydberg excited states. For the CAM-B3LYP functional, Figure 4j, clustering of data points near the origin is only observed for Rydberg excited states. The lambda diagnostic plot for the M08-HX and M08-SO functionals, Figure 5m and 5n, respectively, show a well behaved trend between lambda values and errors in calculated vertical excitation energies with respect to the benchmark set offering a less sporadic spread of errors among valence and Rydberg excited states.

Figure 4. Lambda diagnostics for non-metaGGAs. × (red online) label Rydberg excited states and △ (green online) label valence excited states: (a) SVWN, (b) BLYP, (c) PW91, (d) PBE, (e) OLYP, (f) BHHLYP, (g) B3LYP, (h) PBE0, (i) X3LYP, (j) CAM-B3LYP.

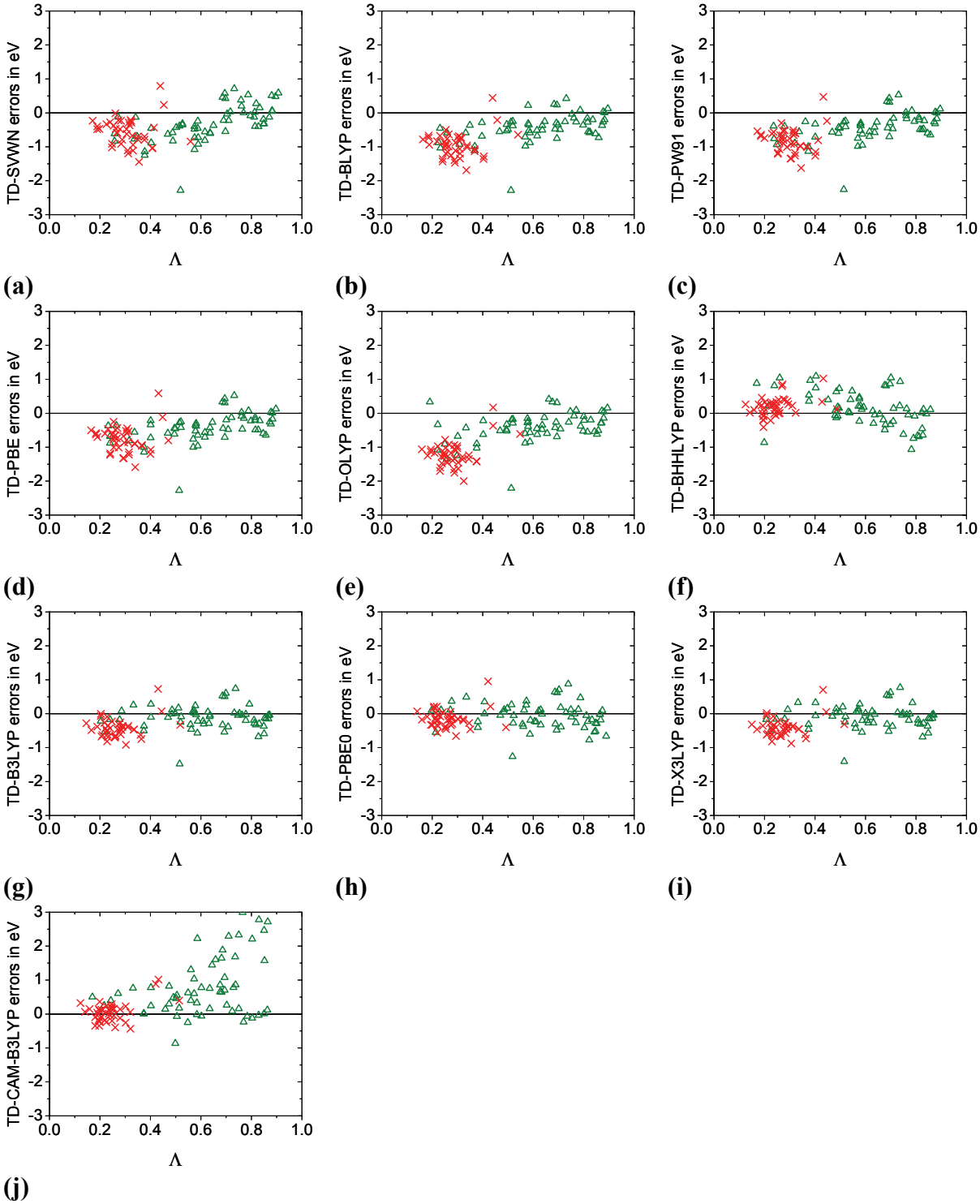

Figure 5. Lambda diagnostics for metaGGAs × (red online) label Rydberg excited states and △ (green online) label valence excited states: (a) VS98, (b) PKZB, (c) TPSS, (d) M06-L, (e) TPSSm, (f) revTPSS, (g) TPSSh, (h) M05, (j) M06, (k) M06-2X, (l) M06-HF, (m) M08-HX, (n) M08-SO.

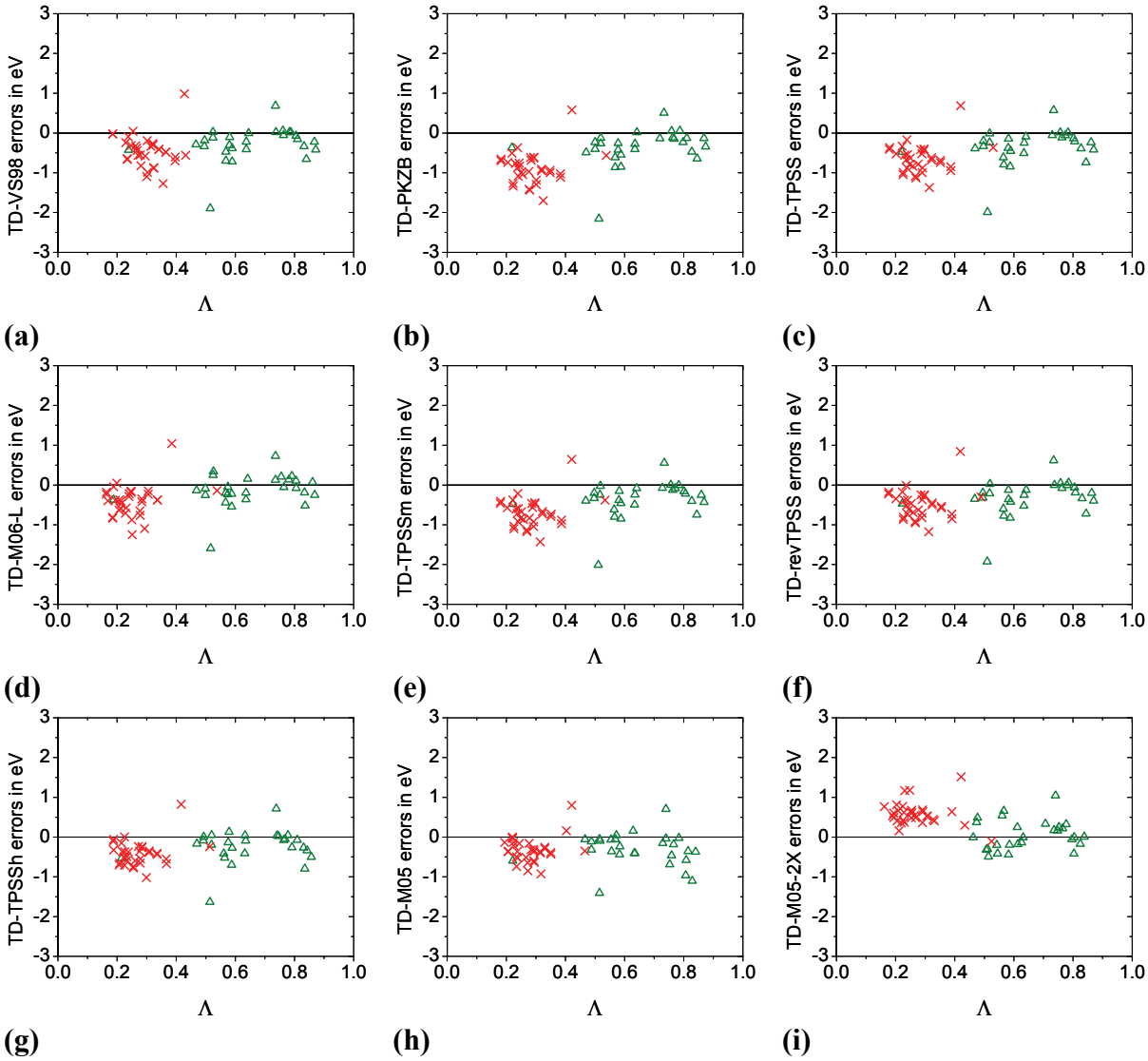

Figure 5. continued.

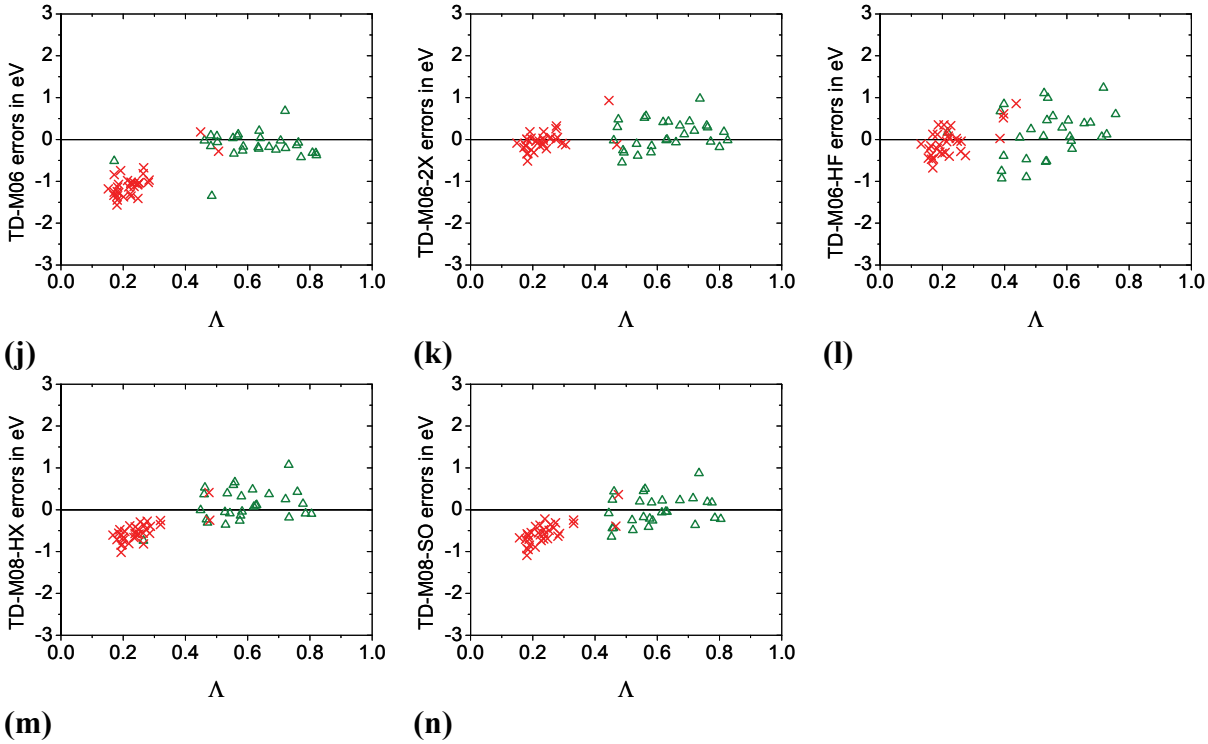

Performance for n→π and π→π* Excited States*

The 60 valence states within the benchmark set can be divided into 30 π→π*, 26 n→π*, 3, n→σ*, and a single σ→π* excitation. Due to the small number of n→σ* and σ→π* excited states, the breakdown for valence states was limited to π→π* and n→π* excitations. Figure 3 shows a graphical representation of the MAE for n→π* and π→π* excited states compared to the total valence MAE for the benchmark set. The corresponding data to Figure 3 is summarized in Tables S8 and S9 in the Supporting Information section. The description of n→π* valence excited states is significantly worse for pure density functionals compared to GH functionals. The inclusion of HF exchange appears to improve the description of n→π* excited states with one exception, M06-HF (MAE = 0.58 eV). Among LDA, GGA, and GH-GGA functionals, all GH-GGAs out perform the others and offer near equivalent treatments of n→π* valence states with MAE values ranging from 0.25-0.32 eV. Between mGGAs and GH-mGGAs, the M06 (MAE = 0.22 eV) functional offers the best performance. The M06-HF (MAE = 0.58 eV) functional performs the worst.

Figure 3. Comparison of density functional mean absolute errors (MAE) for π→π* and n→π* valence excited states.

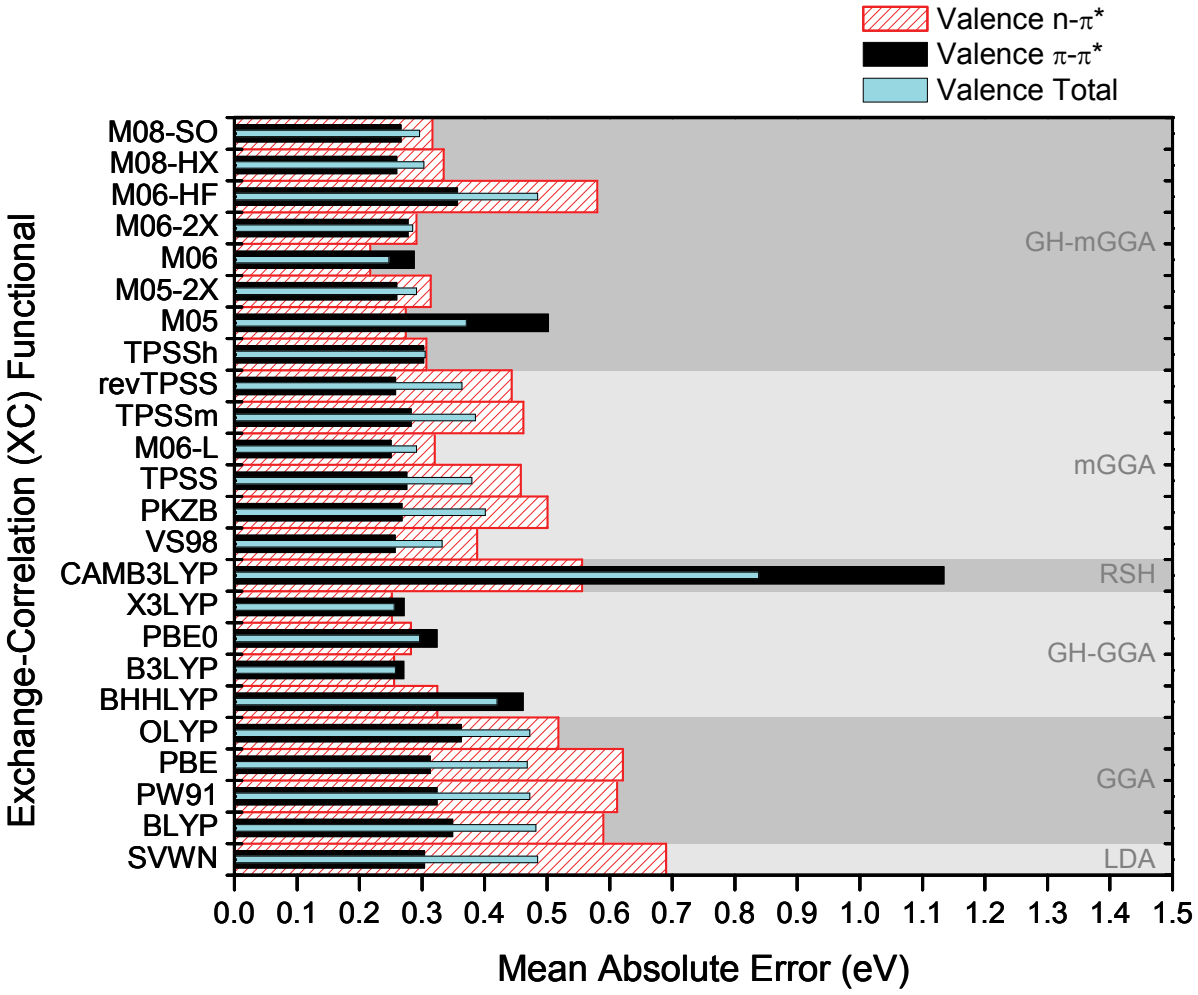

For the π→π* valence excited states, almost all LDA, GGA, and GH-GGA functionals offer equivalent performance with MAE values ranging from 0.27-0.36 eV. The CAM-B3LYP (MAE = 1.14 eV) functional offers the largest error, likely due to the fact that half of the π→π* excited states are triplet states. The CAM-B3LYP functional has been reported to have difficulty in treating triplet excited states [32]. Among the mGGAs and GH-mGGAs, the pure mGGA density functional M06-L (MAE = 0.25 eV) performs the best for π→π* excited states. The poorest performing density functional between mGGAs and GH-mGGAs is the M05 (MAE = 0.50 eV) functional. With the exception of the M05 and M06-

HF functional, the rest of the mGGA and GH-mGGA functionals are within 0.05 eV of the M06-L density functional performance for $\pi \rightarrow \pi^*$ excited states in the benchmark set.

Overall Performance

Table 2 summarizes the calculated MSE, MAE, RMS, largest positive, and largest negative errors for each density functional with respect to the total number of excited states calculated using the linear response TDDFT approach. All density functionals with more than 50% HF exchange possess a positive MSE value, with the exception of the M08-HX (MSE = -0.23 eV) and M08-SO (MSE = -0.30 eV) GH-mGGAs. The underestimation of excitation energies has been ascribed to the incorrect long-range behavior of the exchange-correlation potential (asymptotic vs. $-1/r$ decay) [59]. A reduction in MSE is observed in transitioning from LDA and GGA functionals to GH-GGA functionals. The addition of HF exchange causes the exchange-correlation potential to decay as $-a/r$, where a is a constant other than unity [60][61], i.e., the asymptotic behavior of the exchange-correlation potential offers a better description at long-range compared to pure LDA and GGA density functionals. A larger increase in the percentage of HF exchange brings the MSE closer to positive values. The trend in the MSE is graphically illustrated in Figures 6 and 7, where accuracy plots show the deviation of calculated TDDFT values (points) from experimental values (line at y = x) for vertically excited states.

The MSE values by themselves cannot be used as estimators of density functional performance because they average over positive and negative values and do not offer insight into the magnitude of the errors. Both MAE and RMS estimators offer metrics that take into consideration the magnitude of an error.

Table 2. The overall performance of density functionals for TD-DFT excited state calculations.

Excited States (count)	Functional	MSE	MAE	RMS	Max (–)	Max (+)
All (101)						
	SVWN	-0.41	0.54	0.65	-2.28	0.79
	BLYP	-0.64	0.68	0.79	-2.29	0.44
	PW91	-0.58	0.62	0.73	-2.26	0.53
	PBE	-0.55	0.60	0.71	-2.27	0.59
	OLYP	-0.73	0.77	0.93	-2.21	0.42
	BHHLYP	0.16	0.35	0.47	-1.07	1.09
	B3LYP	-0.24	0.34	0.42	-1.48	0.74
	PBE0	-0.10	0.28	0.36	-1.26	0.95
	X3LYP	-0.22	0.33	0.41	-1.41	0.77
	CAM-B3LYP	0.48	0.59	0.92	-0.86	2.99
All (60)						
	VS98	-0.37	0.43	0.56	-1.89	0.98
	PKZB	-0.64	0.68	0.81	-2.15	0.58
	TPSS	-0.51	0.55	0.66	-1.99	0.69
	M06-L	-0.27	0.39	0.50	-1.59	1.04
	TPSSm	-0.53	0.57	0.69	-2.01	0.64
	revTPSS	-0.41	0.46	0.57	-1.93	0.84
	TPSSh	-0.32	0.39	0.49	-1.63	0.82
	M05	-0.32	0.38	0.48	-1.41	0.80
	M05-2X	0.34	0.45	0.54	-0.49	1.51
	M06	-0.64	0.69	0.85	-1.56	0.68
	M06-2X	0.03	0.22	0.30	-0.55	0.98
	M06-HF	0.04	0.38	0.48	-0.93	1.24
	M08-HX	-0.23	0.44	0.50	-1.02	1.08
	M08-SO	-0.30	0.45	0.51	-1.09	0.79

Figure 6. Accuracy plots for TD-DFT calculated excitation energies for non-metaGGAs: (a) SVWN, (b) BLYP, (c) PW91, (d) PBE, (e) OLYP, (f) BHHLYP, (g) B3LYP, (h) PBE0, (i) X3LYP, (j) CAM-B3LYP. Points above the line indicate positive errors while points below the line indicate negative errors.

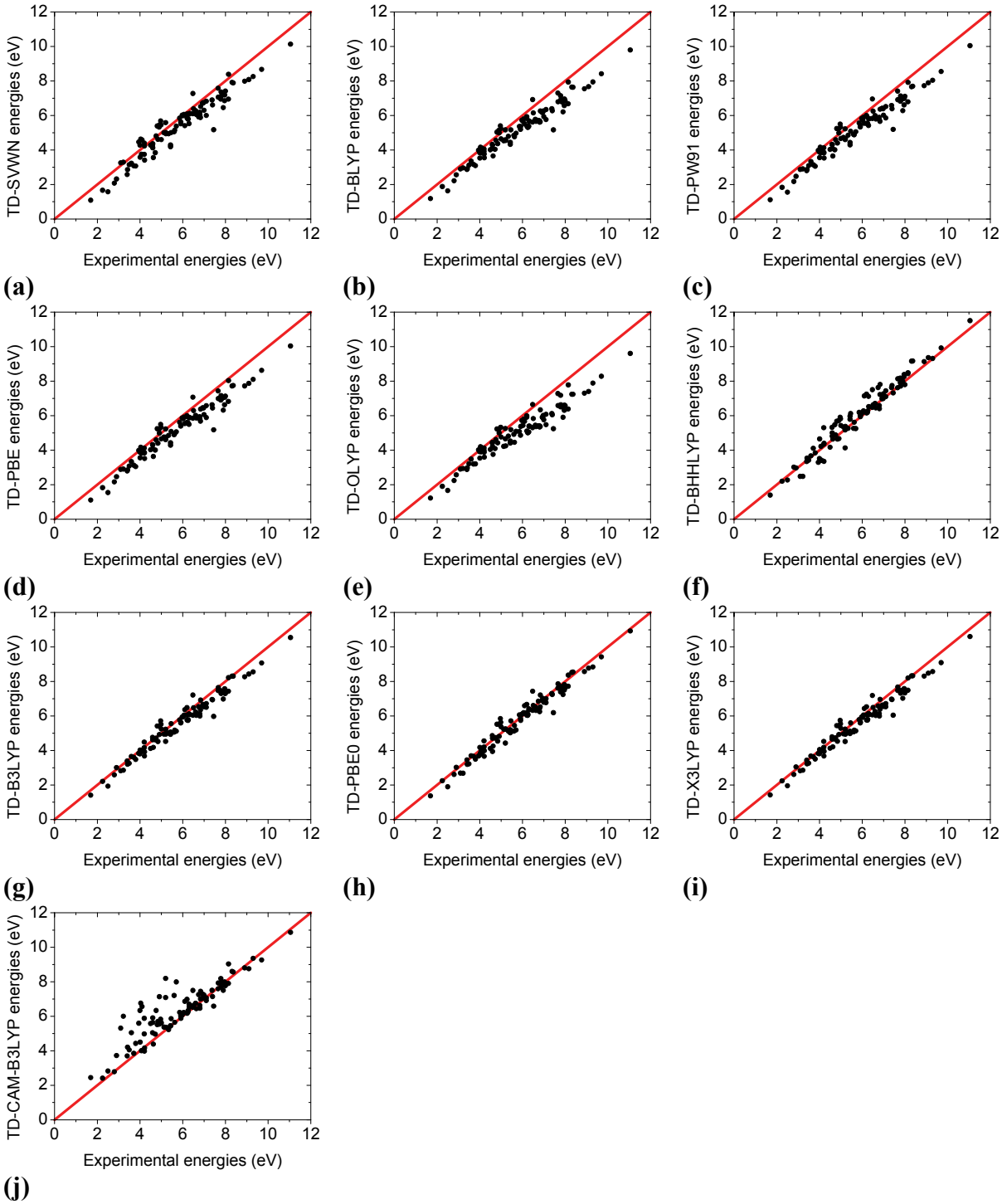

Figure 7. Accuracy plots for TD-DFT calculated excitation energies for metaGGAs: (a) VS98, (b) PKZB, (c) TPSS, (d) M06-L, (e) TPSSm, (f) revTPSS, (g) TPSSh, (h) M05, (j) M06, (k) M06-2X, (l) M06-HF, (m) M08-HX, (n) M08-SO. Points above the line indicate positive errors while points below the line indicate negative errors.

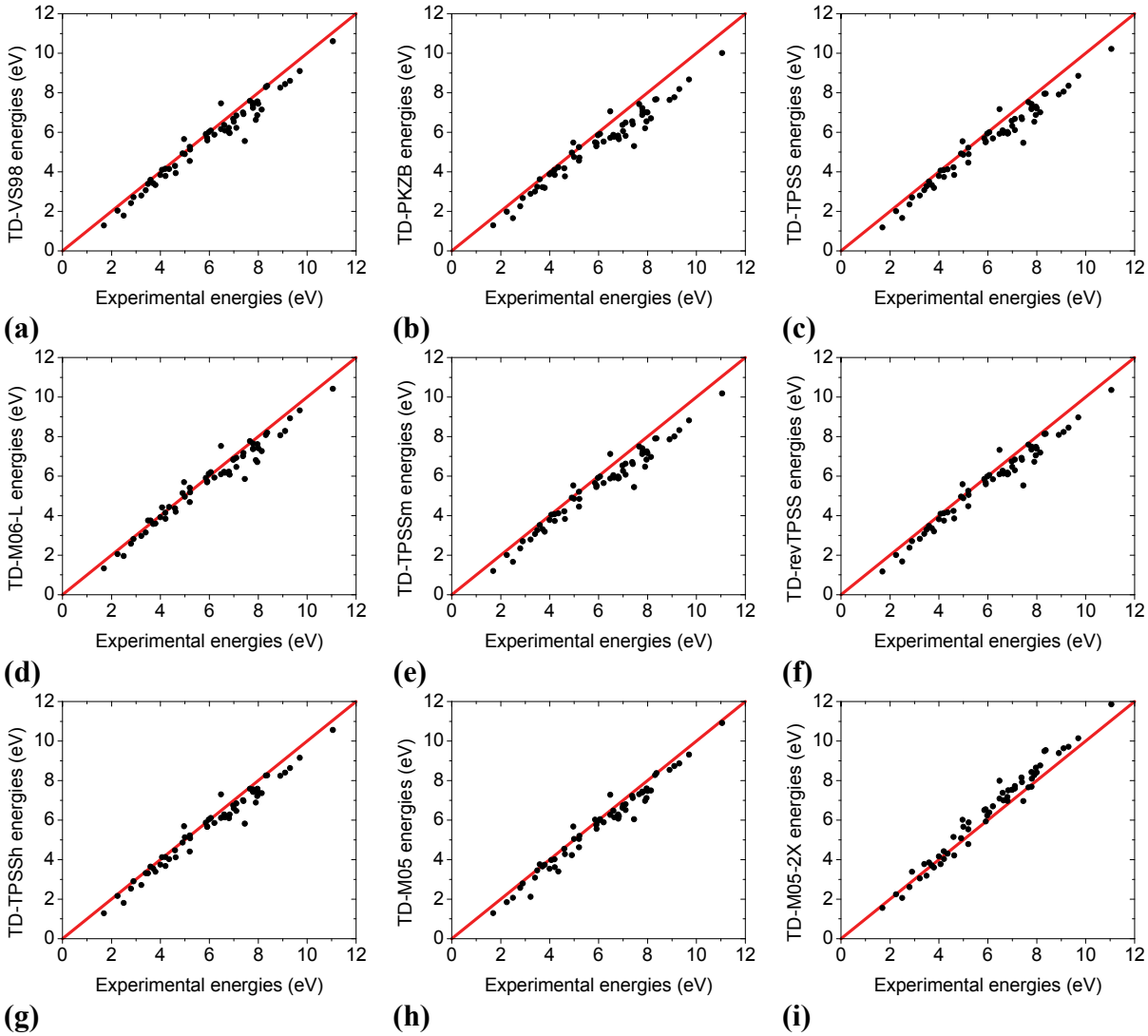

Figure 7. continued.

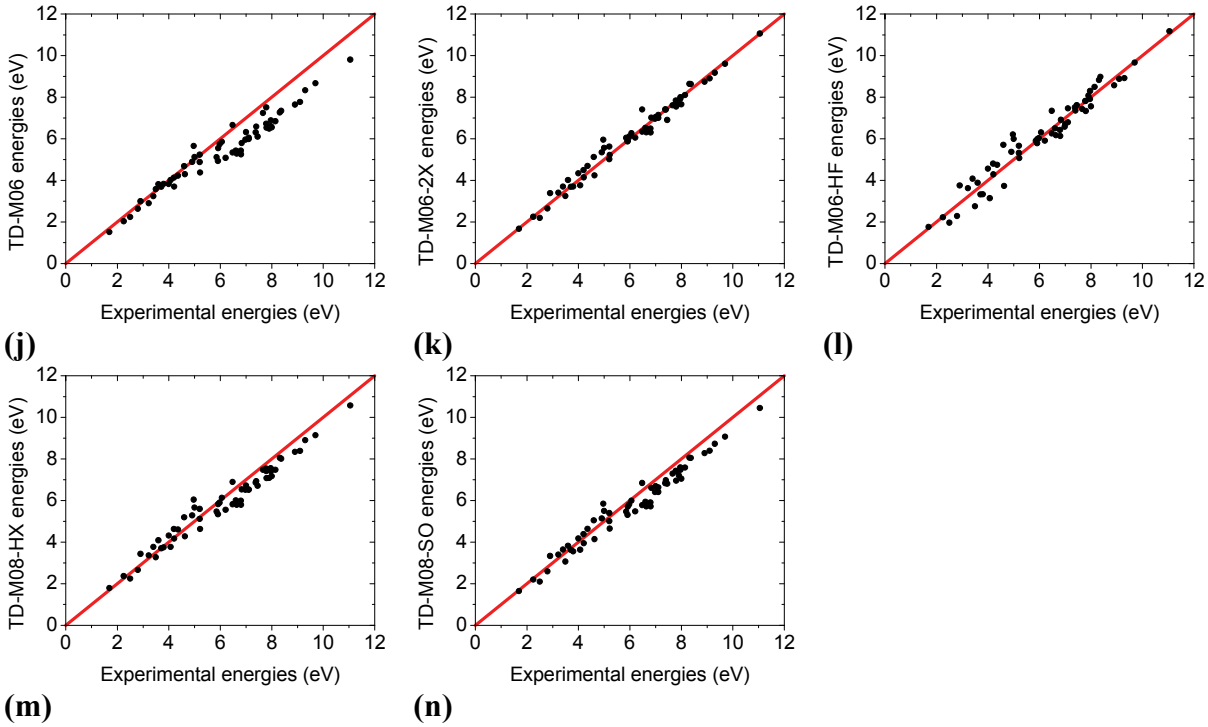

Among LDA, GGA, and GH-GGA functionals, the PBE0 (MAE = 0.28 eV, RMS = 0.36 eV) functional gives the lowest MAE and RMS values overall. The B3LYP (MAE = 0.34 eV, RMS = 0.42 eV) and X3LYP (MAE = 0.33 eV, RMS = 0.41 eV) functionals are within 0.5 eV of the MAE and RMS values of PBE0. The PBE0 functional consist of 25% of HF exchange and performs better overall compared to the BHHLYP (MAE = 0.35 eV, RMS = 0.47 eV) functional, which contains 50% of HF exchange. The latter result suggests that increasing the amount of HF exchange alone will not necessarily result in better performance for the calculation of vertically excited states. Among the LDA, GGA, and GH-GGA functionals, the OLYP (MAE = 0.77 eV, RMS = 0.93 eV) functional produces the largest MAE and RMS values overall. Astonishingly, the LDA functional, SVWN (MAE = 0.54 eV, RMS = 0.65 eV), outperforms the M06 (MAE = 0.69 eV, RMS = 0.85 eV), PKZB (MAE = 0.68 eV, RMS = 0.81 eV), and TPSSm (MAE = 0.55 eV, RMS = 0.66 eV), and all GGA functionals overall.

Between mGGAs and GH-mGGAs, the M06-2X (MAE = 0.22 eV, RMS = 0.30 eV) functional gives the lowest MAE and RMS values while the general-purpose M06 (MAE =

0.69 eV, RMS = 0.85 eV) functional produces the largest. In the case of the M06 functional, doubling the amount of HF exchange significantly improves the performance for the calculation of vertically excited states. The M06-L (MAE = 0.39 eV, RMS = 0.50 eV) functional offers the best overall performance among mGGAs. Convergence issues aside, the M06-L functional performs better than any of the GGA functionals and is almost at the same level of performance as BHHLYP. The benefit of pure density functionals is the increase in computational performance due to the avoidance of calculating the exchange integrals needed for any GH density functional. The recent M08-HX (MAE = 0.44 eV, RMS = 0.50 eV) and M08-SO (MAE = 0.45 eV, RMS = 0.51 eV) functionals offer intermediate performance overall among GH-mGGAs and perform better overall than most mGGAs, with M06-L being the exception.

4. Conclusions

The performance of 24 density functionals for the calculation of vertical excitation energies within the linear response TDDFT formalism was analyzed against a benchmark set consisting of 101 experimental excited state energies. Due to convergence issues in the ground state geometry optimizations, the benchmark set for mGGAs and GH-mGGAs only consisted of 60 excited states. The CAM-B3LYP (MAE = 0.22 eV) and the M06-2X (MAE = 0.17 eV) functionals are recommended for Rydberg excited states. For valence states, the B3LYP (MAE = 0.26 eV), X3LYP (MAE = 0.26 eV), PBE0 (MAE = 0.30 eV), and M06 (MAE = 0.25 eV) functionals offer equal performance. The M06-L functional is an attractive option for the calculation of valence excited states since it is a pure density functional, and it does not require the computation of the exchange integrals needed for admixture of HF exchange in GH functionals. For singlet states, the PBE0 (MAE = 0.25 eV) and M06-2X (MAE = 0.22 eV) functionals offer the best performance. For triplet states, GH functionals are needed with B3LYP (MAE = 0.31 eV), X3LYP (MAE = 0.31 eV), PBE0 (MAE = 0.32 eV), and M06-2X (MAE = 0.24 eV) performing well. The CAM-B3LYP (MAE = 1.10 eV) functional is not recommend for the treatment of triplet excited states.

Overall, the best performing pure density functional is M06-L (MAE = 0.39 eV). The best overall performing GH-GGA functional is PBE0 (MAE = 0.28 eV). The best overall performing GH-mGGA functional is M06-2X (MAE = 0.22 eV). Of the GGA functionals

tested, none could be recommended since the LDA functional, SVWN (MAE = 0.54 eV), outperforms all GGA functionals overall. In light of the unresolved convergence issues for several of the mGGAs and GH-mGGAs, the best overall density functional based on the benchmark used in this study is the PBE0 functional which offers a balanced treatment of singlet (MAE = 0.25) , triplet (MAE = 0.32 eV), valence (MAE = 0.30 eV), and Rydberg (MAE = 0.25) excited states.

Acknowledgements

This work was supported by a grant from the Air Force Office of Scientific Research. S.S. thanks Mr. Leo C. DeSesso for invaluable assistance in reviewing and editing the manuscript.

Supporting Information

Table S3. List of excited states considered in current benchmark with experimental values and references.

Molecule	State	Type		Expt. (eV)	References
benzene					
	1^1B_{2u}	Valence	$\pi \rightarrow \pi^*$	4.90	[109]
	1^1B_{1u}	Valence	$\pi \rightarrow \pi^*$	6.20	[110]
	1^1E_{1g}	Rydberg	3s	6.33	[111]
	1^1A_{2u}	Rydberg	3p	6.93	[112]
	1^1E_{2u}	Rydberg	3p	6.95	[113]
	1^3B_{1u}	Valence	$\pi \rightarrow \pi^*$	3.95	[114]
	1^3E_{1u}	Valence	$\pi \rightarrow \pi^*$	4.76	[114]
	1^3B_{2u}	Valence	$\pi \rightarrow \pi^*$	5.60	[114]
butadiene					
	1^1B_u	Valence	$\pi \rightarrow \pi^*$	5.92	[115]
	1^1B_g	Rydberg	3s	6.21	[116]
	1^1A_u	Rydberg	3p	6.64	[116]
	2^1A_u	Rydberg	3p	6.80	[115]
	1^3B_u	Valence	$\pi \rightarrow \pi^*$	3.22	[117]
	1^3A_g	Valence	$\pi \rightarrow \pi^*$	4.91	[117]
	1^3A_u	Rydberg	3p	6.81	[118]
cyclopentadiene					
	1^1B_2	Valence	$\pi \rightarrow \pi^*$	5.34	[119]
	1^1A_2	Rydberg	3s	5.63	[120]
	1^1B_1	Rydberg	3p	6.25	[121]
	2^1A_2	Rydberg	3p	6.26	[121]
	2^1A_1	Valence	$\pi \rightarrow \pi^*$	6.2	[122]
	2^1B_2	Rydberg	3p	6.31	[121]
	3^1B_1	Rydberg	3s	7.85	[123]
	1^3B_2	Valence	$\pi \rightarrow \pi^*$	3.10	[124]
ethylene					
	1^1B_{3u}	Rydberg	3s	7.11	[125]
	1^1B_{1g}	Rydberg	3p	7.80	[125]
	1^1B_{1u}	Valence	$\pi \rightarrow \pi^*$	7.66	[125]
	1^1B_{2g}	Rydberg	3p	8.0	[125]
	1^3B_{3u}	Rydberg	3s	6.98	[125]
	1^3B_{1u}	Rydberg	3p	7.79	[125]
	1^3A_g	Rydberg	3p	8.15	[125]

Table S3. continue.

Molecule	State	Type		Expt. (eV)	References
formaldehyde					
	1^1A_2	Valence	$n \rightarrow \pi^*$	4.07	[126]
	1^1B_2	Rydberg	3s	7.11	[126]
	2^1B_2	Rydberg	3p	7.97	[126]
	2^1A_1	Rydberg	3p	8.14	[126]
	2^1A_2	Rydberg	3p	8.37	[126]
	1^3A_2	Valence	$n \rightarrow \pi^*$	3.50	[126]
	1^3B_2	Rydberg	3s	6.83	[126]
	2^3B_2	Rydberg	3p	7.79	[126]
	2^3A_1	Rydberg	3p	7.96	[126]
	2^3A_2	Rydberg	3p	8.31	[126]
furan					
	1^1A_2	Rydberg	3s	5.91	[126]
	1^1B_2	Valence	$\pi \rightarrow \pi^*$	6.06	[127]
	1^1B_1	Rydberg	3p	6.48	[128]
	2^1B_2	Rydberg	3p	6.48	[128]
	2^1A_2	Rydberg	3p	6.61	[128]
	3^1B_1	Rydberg	3s	7.38	[128]
	1^3B_2	Valence	$\pi \rightarrow \pi^*$	4.0	[129]
	1^3A_1	Valence	$\pi \rightarrow \pi^*$	5.2	[129]
methylenecyclopropene					
	1^1B_2	Valence	$\pi \rightarrow \pi^*$	4.01	[130]
	1^1B_1	Valence	$\sigma \rightarrow \pi^*$	5.12	[130]
	2^1A_1	Valence	$\pi \rightarrow \pi^*$	6.02	[130]
pyrazine					
	1^1B_{3u}	Valence	$n \rightarrow \pi^*$	4.22	[131]
	1^1A_u	Valence	$n \rightarrow \pi^*$	4.72	[132]
	1^1B_{2u}	Valence	$\pi \rightarrow \pi^*$	4.81	[133]
	1^1B_{2g}	Valence	$n \rightarrow \pi^*$	5.46	[134]
	1^1B_{1g}	Valence	$n \rightarrow \pi^*$	6.10	[132]
	1^1A_g	Valence	$n \rightarrow \sigma^*$	6.30	[135]
	1^1B_{1u}	Valence	$\pi \rightarrow \pi^*$	6.51	[133]
	2^1B_{2u}	Valence	$n \rightarrow \sigma^*$	6.75	[135]
	2^1B_{1u}	Valence	$n \rightarrow \sigma^*$	6.84	[135]
	3^1B_{1u}	Valence	$\pi \rightarrow \pi^*$	7.67	[133]
	1^3B_{3u}	Valence	$n \rightarrow \pi^*$	3.42	[134]
	1^3B_{1u}	Valence	$\pi \rightarrow \pi^*$	4.04	[134]
	1^3A_u	Valence	$n \rightarrow \pi^*$	4.2	[134]
	1^3B_{2u}	Valence	$\pi \rightarrow \pi^*$	4.5	[134]
	1^3B_{2g}	Valence	$n \rightarrow \pi^*$	4.6	[134]
	2^3B_{1u}	Valence	$\pi \rightarrow \pi^*$	5.7	[134]

Table S3. continue.

Molecule	State	Type		Expt. (eV)	References
pyridine					
	1^1B_1	Valence	$n \rightarrow \pi^*$	4.59	[135]
	1^1B_2	Valence	$\pi \rightarrow \pi^*$	4.99	[135]
	1^1A_2	Valence	$n \rightarrow \pi^*$	5.43	[135]
	1^3A_1	Valence	$\pi \rightarrow \pi^*$	4.1	[135]
	1^3B_2	Valence	$\pi \rightarrow \pi^*$	4.84	[135]
	1^3A_2	Valence	$n \rightarrow \pi^*$	5.43	[135]
pyrrole					
	1^1A_2	Rydberg	3s	5.22	[127]
	2^1B_1	Rydberg	3p	5.86	[136]
	2^1B_2	Valence	$\pi \rightarrow \pi^*$	5.98	[137]
	1^3B_2	Valence	$\pi \rightarrow \pi^*$	4.21	[138]
s-tetrazine					
	1^1B_{3u}	Valence	$n \rightarrow \pi^*$	2.25	[139]
	1^1A_u	Valence	$n \rightarrow \pi^*$	3.4	[140]
	1^1B_{2u}	Valence	$\pi \rightarrow \pi^*$	4.97	[141]
	2^1A_u	Valence	$n \rightarrow \pi^*$	5.0	[141]
	1^3B_{3u}	Valence	$n \rightarrow \pi^*$	1.69	[141]
	1^3A_u	Valence	$n \rightarrow \pi^*$	2.90	[141]
	1^3B_{1g}	Valence	$n \rightarrow \pi^*$	3.6	[141]
	1^3B_{2u}	Valence	$n \rightarrow \pi^*$	4.2	[141]
	2^3A_u	Valence	$n \rightarrow \pi^*$	4.6	[141]
s-trans acrolein					
	$1^1A''$	Valence	$n \rightarrow \pi^*$	3.71	[142]
s-trans glyoxal					
	1^1A_u	Valence	$n \rightarrow \pi^*$	2.8	[143]
	1^1B_g	Valence	$n \rightarrow \pi^*$	4.63	[144]
	2^1B_g	Valence	$n \rightarrow \pi^*$	7.45	[126]
	1^1B_u	Rydberg	3p	7.9	[143]
	1^3A_u	Valence	$n \rightarrow \pi^*$	2.5	[143]
	1^3B_g	Valence	$n \rightarrow \pi^*$	3.8	[143]
	1^3B_u	Valence	$\pi \rightarrow \pi^*$	5.2	[143]
water					
	1^1B_1	Rydberg	3s	7.4	[145]
	1^1A_2	Rydberg	3p	9.1	[145]
	2^1A_1	Rydberg	3s	9.7	[145]
	1^1B_2	Rydberg	3p	11.05	[146]
	1^3B_1	Rydberg	3s	7.0	[145]
	1^3A_2	Rydberg	3p	8.9	[145]
	1^3A_1	Rydberg	3s	9.3	[145]

Table S4. The performance of density functionals for TD-DFT calculations of singlet excited states.

Excited States (count)	Functional	MSE	MAE	RMS
Singlet (63)				
	SVWN	-0.46	0.56	0.68
	BLYP	-0.70	0.75	0.85
	PW91	-0.60	0.66	0.76
	PBE	-0.57	0.64	0.74
	OLYP	-0.84	0.89	1.01
	BHHLYP	0.30	0.34	0.47
	B3LYP	-0.22	0.36	0.44
	PBE0	0.00	0.25	0.35
	X3LYP	-0.20	0.35	0.43
	CAM-B3LYP	0.13	0.28	0.37
Singlet (35)				
	VS98	-0.35	0.45	0.60
	PKZB	-0.69	0.75	0.87
	TPSS	-0.52	0.59	0.71
	M06-L	-0.28	0.42	0.54
	TPSSm	-0.55	0.62	0.74
	revTPSS	-0.40	0.49	0.62
	TPSSh	-0.30	0.40	0.52
	M05	-0.25	0.35	0.46
	M05-2X	0.43	0.51	0.60
	M06	-0.76	0.81	0.94
	M06-2X	0.00	0.21	0.32
	M06-HF	0.00	0.36	0.47
	M08-HX	-0.35	0.50	0.56
	M08-SO	-0.41	0.52	0.57

Table S5. The performance of density functionals for TD-DFT calculations of triplet excited states.

Excited States (count)	Functional	MSE	MAE	RMS
Triplet (38)				
	SVWN	-0.32	0.51	0.59
	BLYP	-0.55	0.56	0.69
	PW91	-0.54	0.55	0.67
	PBE	-0.52	0.54	0.65
	OLYP	-0.56	0.59	0.76
	BHHLYP	-0.08	0.37	0.46
	B3LYP	-0.28	0.31	0.39
	PBE0	-0.26	0.32	0.37
	X3LYP	-0.27	0.31	0.38
	CAM-B3LYP	1.07	1.10	1.42
Triplet (25)				
	VS98	-0.40	0.40	0.50
	PKZB	-0.56	0.57	0.71
	TPSS	-0.49	0.49	0.58
	M06-L	-0.27	0.35	0.45
	TPSSm	-0.51	0.51	0.61
	revTPSS	-0.42	0.43	0.51
	TPSSh	-0.36	0.36	0.44
	M05	-0.40	0.42	0.51
	M05-2X	0.21	0.37	0.44
	M06	-0.47	0.51	0.70
	M06-2X	0.08	0.24	0.29
	M06-HF	0.09	0.40	0.48
	M08-HX	-0.05	0.34	0.40
	M08-SO	-0.16	0.35	0.40

Table S6. The performance of density functionals for TD-DFT calculations of valence excited states.

Excited States (count)	Functional	MSE	MAE	RMS
Valence (60)				
	SVWN	-0.30	0.48	0.61
	BLYP	-0.44	0.48	0.60
	PW91	-0.41	0.47	0.59
	PBE	-0.41	0.47	0.58
	OLYP	-0.41	0.47	0.60
	BHHLYP	0.14	0.42	0.54
	B3LYP	-0.12	0.26	0.36
	PBE0	-0.06	0.30	0.39
	X3LYP	-0.10	0.26	0.35
	CAM-B3LYP	0.78	0.84	1.16
Valence (28)				
	VS98	-0.27	0.33	0.50
	PKZB	-0.36	0.40	0.57
	TPSS	-0.34	0.38	0.54
	M06-L	-0.12	0.29	0.42
	TPSSm	-0.35	0.39	0.55
	revTPSS	-0.31	0.36	0.53
	TPSSh	-0.23	0.31	0.46
	M05	-0.31	0.37	0.51
	M05-2X	0.05	0.29	0.37
	M06	-0.15	0.25	0.36
	M06-2X	0.11	0.29	0.36
	M06-HF	0.15	0.48	0.59
	M08-HX	0.12	0.30	0.39
	M08-SO	-0.01	0.30	0.35

Table S7. The performance of density functionals for TD-DFT calculations of Rydberg excited states.

Excited States (count)	Functional	MSE	MAE	RMS
Rydberg (41)				
	SVWN	-0.56	0.61	0.70
	BLYP	-0.94	0.97	1.01
	PW91	-0.82	0.84	0.89
	PBE	-0.76	0.79	0.85
	OLYP	-1.21	1.21	1.26
	BHHLYP	0.19	0.25	0.34
	B3LYP	-0.42	0.46	0.50
	PBE0	-0.15	0.25	0.31
	X3LYP	-0.41	0.44	0.49
	CAM-B3LYP	0.05	0.22	0.30
Rydberg (32)				
	VS98	-0.45	0.52	0.60
	PKZB	-0.89	0.92	0.97
	TPSS	-0.65	0.70	0.75
	M06-L	-0.41	0.48	0.57
	TPSSm	-0.70	0.74	0.79
	revTPSS	-0.49	0.55	0.61
	TPSSh	-0.41	0.46	0.52
	M05	-0.32	0.38	0.45
	M05-2X	0.58	0.59	0.65
	M06	-1.06	1.08	1.12
	M06-2X	-0.04	0.17	0.25
	M06-HF	-0.06	0.28	0.35
	M08-HX	-0.53	0.55	0.58
	M08-SO	-0.56	0.58	0.62

Table S8. The performance of density functionals for TD-DFT calculations of n→π* excited states.

Excited States (count)	Functional	MSE	MAE	RMS
n→π* (26)				
	SVWN	-0.67	0.69	0.81
	BLYP	-0.59	0.59	0.72
	PW91	-0.61	0.61	0.74
	PBE	-0.62	0.62	0.75
	OLYP	-0.52	0.52	0.67
	BHHLYP	0.26	0.32	0.44
	B3LYP	-0.16	0.25	0.38
	PBE0	-0.12	0.28	0.39
	X3LYP	-0.12	0.25	0.37
	CAM-B3LYP	0.46	0.56	0.71
n→π* (16)				
	VS98	-0.38	0.39	0.59
	PKZB	-0.50	0.50	0.70
	TPSS	-0.46	0.46	0.65
	M06-L	-0.23	0.32	0.48
	TPSSm	-0.46	0.46	0.65
	revTPSS	-0.44	0.44	0.63
	TPSSh	-0.28	0.31	0.50
	M05	-0.25	0.27	0.42
	M05-2X	0.00	0.31	0.36
	M06	-0.14	0.22	0.37
	M06-2X	0.03	0.29	0.34
	M06-HF	0.01	0.58	0.66
	M08-HX	0.07	0.34	0.40
	M08-SO	-0.06	0.32	0.36

Table S9. The performance of density functionals for TD-DFT calculations of π→π* excited states.

Excited States (count)	Functional	MSE	MAE	RMS
π→π* (30)				
	SVWN	0.05	0.30	0.37
	BLYP	-0.26	0.35	0.41
	PW91	-0.20	0.32	0.38
	PBE	-0.19	0.31	0.37
	OLYP	-0.24	0.36	0.43
	BHHLYP	-0.04	0.46	0.57
	B3LYP	-0.09	0.27	0.35
	PBE0	-0.05	0.32	0.40
	X3LYP	-0.08	0.27	0.36
	CAM-B3LYP	1.10	1.14	1.49
π →π* (12)				
	VS98	-0.12	0.26	0.35
	PKZB	-0.17	0.27	0.33
	TPSS	-0.18	0.28	0.36
	M06-L	0.02	0.25	0.31
	TPSSm	-0.19	0.28	0.36
	revTPSS	-0.14	0.26	0.35
	TPSSh	-0.17	0.30	0.40
	M05	-0.38	0.50	0.60
	M05-2X	0.12	0.26	0.37
	M06	-0.17	0.29	0.34
	M06-2X	0.23	0.28	0.37
	M06-HF	0.32	0.36	0.48
	M08-HX	0.18	0.26	0.38
	M08-SO	0.05	0.27	0.33

Table S10. Errors (eV) in TD-DFT singlet vertical excitation energies for non-metaGGAs relative to experimental value (Error = $E_{TD\text{-}DFT} - E_{Experiment}$).

Molecule	State	Type		Expt.	SVWN	BLYP	PW91	PBE	OLYP	BHHLYP	B3LYP5	PBE0	X3LYP	CAM-B3LYP
benzene														
	1^1B_{2u}	V	π→π*	4.90	0.422	0.234	0.315	0.311	0.312	0.811	0.504	0.623	0.528	0.644
	1^1B_{1u}	V	π→π*	6.20	-0.125	-0.370	-0.264	-0.260	-0.288	-0.015	-0.151	-0.019	-0.135	0.008
	1^1E_{1g}	R	3s	6.33	-0.211	-0.684	-0.511	-0.444	-0.942	0.175	-0.256	0.054	-0.255	0.212
	1^1A_{2u}	R	3p	6.93	-0.220	-0.762	-0.529	-0.488	-1.022	0.050	-0.347	-0.026	-0.333	0.102
	1^1E_{2u}	R	3p	6.95	-0.230	-0.783	-0.538	-0.502	-1.059	0.261	-0.282	0.070	-0.318	0.325
butadiene														
	1^1B_u	V	π→π*	5.92	-0.402	-0.562	-0.500	-0.489	-0.549	0.018	-0.294	-0.176	-0.278	-0.036
	1^1B_g	R	3s	6.21	-0.364	-0.820	-0.659	-0.596	-1.099	-0.059	-0.446	-0.167	-0.446	-0.040
	1^1A_u	R	3p	6.64	-0.585	-0.991	-0.849	-0.781	-1.279	-0.194	-0.607	-0.330	-0.609	-0.199
	2^1A_u	R	3p	6.80	-0.622	-1.111	-0.914	-0.866	-1.389	-0.214	-0.678	-0.373	-0.665	-0.177
cyclopentadiene														
	1^1B_2	V	π→π*	5.34	-0.396	-0.553	-0.489	-0.487	-0.527	-0.080	-0.327	-0.224	-0.310	-0.119
	1^1A_2	R	3s	5.63	-0.483	-0.871	-0.753	-0.673	-1.172	-0.016	-0.458	-0.185	-0.460	0.012
	1^1B_1	R	3p	6.25	-0.467	-0.936	-0.749	-0.699	-1.229	-0.063	-0.511	-0.217	-0.496	-0.010
	2^1A_2	R	3p	6.26	-0.470	-0.941	-0.743	-0.701	-1.249	0.014	-0.486	-0.178	-0.466	0.065
	2^1A_1	V	π→π*	6.2	-0.120	-0.272	-0.199	-0.200	-0.207	1.046	0.283	0.471	0.326	0.784
	2^1B_2	R	3p	6.31	-0.230	-0.632	-0.517	-0.433	-0.923	0.215	-0.228	0.038	-0.227	0.233
	3^1B_1	R	3s	7.85	-0.671	-1.060	-0.918	-0.850	-1.336	0.240	-0.464	-0.143	-0.448	0.131
ethylene														
	1^1B_{3u}	R	3s	7.11	-0.286	-0.766	-0.598	-0.534	-1.030	-0.008	-0.391	-0.105	-0.392	-0.051
	1^1B_{1g}	R	3p	7.80	-0.080	-0.359	-0.247	-0.225	-0.378	-0.047	-0.190	-0.050	-0.186	-0.067
	1^1B_{1u}	V	π→π*	7.66	-0.434	-0.896	-0.671	-0.638	-1.164	-0.089	-0.497	-0.195	-0.482	-0.118
	1^1B_{2g}	R	3p	8.0	-0.589	-1.152	-0.892	-0.874	-1.424	-0.205	-0.695	-0.362	-0.669	-0.228
formaldehyde														
	1^1A_2	V	n→π*	4.07	-0.316	-0.247	-0.239	-0.250	-0.174	0.148	-0.089	-0.053	-0.083	-0.070
	1^1B_2	R	3s	7.11	-1.112	-1.344	-1.259	-1.221	-1.630	0.329	-0.608	-0.340	-0.575	-0.201
	2^1B_2	R	3p	7.97	-0.785	-1.015	-0.985	-0.904	-1.361	0.417	-0.395	-0.151	-0.386	-0.120
	2^1A_1	R	3p	8.14	-1.194	-1.468	-1.344	-1.320	-1.754	0.294	-0.703	-0.420	-0.652	-0.243
	2^1A_2	R	3p	8.37	-0.483	-0.732	-0.682	-0.625	-1.132	0.800	-0.068	0.178	-0.047	0.190
furan														
	1^1A_2	R	3s	5.91	-0.287	-0.719	-0.577	-0.518	-1.051	0.089	-0.317	-0.055	-0.315	0.113
	1^1B_2	V	π→π*	6.06	0.004	-0.264	-0.170	-0.147	-0.263	0.220	-0.019	0.129	-0.010	0.159
	1^1B_1	R	3p	6.48	-0.376	-0.864	-0.656	-0.630	-1.175	-0.003	-0.437	-0.153	-0.416	0.038
	2^1B_2	R	3p	6.48	0.793	0.439	0.471	0.589	0.169	1.022	0.733	0.951	0.703	1.015
	2^1A_2	R	3p	6.61	-0.335	-0.834	-0.614	-0.598	-1.170	0.099	-0.381	-0.088	-0.354	0.145
	3^1B_1	R	3s	7.38	-0.480	-0.993	-0.800	-0.744	-1.262	0.240	-0.425	-0.080	-0.406	0.125

Table S10. continued.

Molecule	State	Type		Expt.	SVWN	BLYP	PW91	PBE	OLYP	BHHLYP	B3LYP5	PBE0	X3LYP	CAM-B3LYP
methylenecyclopropene														
	1^1B_2	V	π→π*	4.01	-0.431	-0.482	-0.450	-0.453	-0.477	0.640	0.010	0.164	0.043	0.489
	1^1B_1	V	σ→π*	5.12	-0.119	-0.590	-0.395	-0.357	-0.905	0.216	-0.168	0.115	-0.159	0.252
	2^1A_1	V	π→π*	6.02	-0.033	-0.347	-0.285	-0.195	-0.593	0.182	-0.083	0.119	-0.103	0.175
pyrazine														
	1^1B_{3u}	V	n→π*	4.22	-0.810	-0.676	-0.694	-0.704	-0.625	0.179	-0.299	-0.241	-0.271	-0.061
	1^1A_u	V	n→π*	4.72	-0.880	-0.686	-0.712	-0.721	-0.624	0.750	-0.102	0.002	-0.056	0.241
	1^1B_{2u}	V	π→π*	4.81	0.578	0.220	0.434	0.429	0.418	0.864	0.605	0.708	0.628	0.702
	1^1B_{2g}	V	n→π*	5.46	-0.453	-0.295	-0.380	-0.380	-0.277	0.657	0.097	0.254	0.134	0.398
	1^1B_{1g}	V	n→π*	6.10	-0.690	-0.586	-0.554	-0.556	-0.430	1.044	0.259	0.493	0.329	0.764
	1^1A_g	V	n→σ*	6.30	-0.770	-0.926	-0.886	-0.807	-1.249	0.814	-0.172	0.113	-0.152	0.400
	1^1B_{1u}	V	π→π*	6.51	-0.130	-0.365	-0.259	-0.215	-0.677	0.111	-0.036	0.096	-0.019	0.119
	2^1B_{2u}	V	n→σ*	6.75	-0.831	-1.032	-0.934	-0.884	-1.340	0.882	-0.216	0.100	-0.169	0.501
	2^1B_{1u}	V	n→σ*	6.84	-0.326	-0.581	-0.475	-0.467	-0.505	0.971	0.079	0.368	0.121	0.605
	3^1B_{1u}	V	π→π*	7.67	-0.612	-0.875	-0.758	-0.681	-1.083	0.470	-0.026	0.185	0.007	0.261
pyridine														
	1^1B_1	V	n→π*	4.59	-0.384	-0.269	-0.268	-0.275	-0.186	0.728	0.170	0.265	0.202	0.456
	1^1B_2	V	π→π*	4.99	0.460	0.254	0.337	0.333	0.333	0.826	0.526	0.644	0.550	0.654
	1^1A_2	V	n→π*	5.43	-1.140	-0.986	-0.994	-1.002	-0.901	0.537	-0.362	-0.232	-0.312	0.001
pyrrole														
	1^1A_2	R	3s	5.22	-0.275	-0.678	-0.563	-0.465	-0.972	0.156	-0.270	0.021	-0.279	0.142
	2^1B_1	R	3p	5.86	-0.016	-0.497	-0.301	-0.251	-0.783	0.327	-0.092	0.206	-0.077	0.361
	2^1B_2	V	π→π*	5.98	0.034	-0.259	-0.160	-0.121	-0.263	0.144	-0.046	0.120	-0.041	0.084
s-tetrazine														
	1^1B_{3u}	V	n→π*	2.25	-0.585	-0.372	-0.418	-0.423	-0.349	-0.047	-0.043	-0.012	-0.017	0.158
	1^1A_u	V	n→π*	3.4	-0.828	-0.530	-0.600	-0.611	-0.524	-0.062	-0.009	0.054	0.031	0.296
	1^1B_{2u}	V	π→π*	4.97	0.713	0.423	0.528	0.523	0.335	0.935	0.742	0.877	0.771	0.861
	2^1A_u	V	n→π*	5.0	-0.399	-0.354	-0.333	-0.342	-0.240	0.427	0.238	0.375	0.286	0.600
s-trans acrolein														
	$1^1A''$	V	n π*	3.71	-0.628	-0.551	-0.568	-0.585	-0.512	0.398	-0.108	-0.046	-0.077	0.141
s-trans glyoxal														
	1^1A_u	V	n→π*	2.8	-0.726	-0.588	-0.627	-0.643	-0.567	0.216	-0.221	-0.191	-0.196	-0.017
	1^1B_g	V	n→π*	4.63	-1.076	-0.975	-0.985	-1.000	-0.877	0.015	-0.457	-0.375	-0.429	-0.248
	2^1B_g	V	n→π*	7.45	-2.280	-2.285	-2.255	-2.272	-2.209	-0.133	-1.479	-1.263	-1.406	-0.864
	1^1B_u	R	3p	7.9	-1.446	-1.689	-1.621	-1.587	-2.000	0.091	-0.917	-0.659	-0.877	-0.395
water														
	1^1B_1	R	3s	7.4	-0.794	-1.128	-1.014	-0.962	-1.349	0.350	-0.470	-0.162	-0.454	-0.255
	1^1A_2	R	3p	9.1	-1.017	-1.432	-1.208	-1.225	-1.698	0.263	-0.672	-0.330	-0.620	-0.346
	2^1A_1	R	3s	9.7	-1.029	-1.282	-1.153	-1.079	-1.419	0.224	-0.627	-0.275	-0.611	-0.435
	1^1B_2	R	3p	11.05	-0.913	-1.256	-1.009	-1.013	-1.447	0.459	-0.503	-0.119	-0.448	-0.188

Table S11. Errors (eV) in TD-DFT triplet vertical excitation energies for non-metaGGAs relative to experimental value (Error = $E_{TD\text{-}DFT} - E_{Experiment}$).

Molecule	State	Type		Expt.	SVWN	BLYP	PW91	PBE	OLYP	BHHLYP	B3LYP5	PBE0	X3LYP	CAM-B3LYP
benzene														
	1^3B_{1u}	V	$\pi \rightarrow \pi^*$	3.95	0.513	0.034	0.022	0.032	0.069	-0.658	-0.125	-0.275	-0.130	1.647
	1^3E_{1u}	V	$\pi \rightarrow \pi^*$	4.76	0.047	-0.202	-0.170	-0.170	-0.142	0.118	-0.049	-0.011	-0.032	1.576
	1^3B_{2u}	V	$\pi \rightarrow \pi^*$	5.60	-0.546	-0.753	-0.702	-0.709	-0.689	-0.339	-0.540	-0.483	-0.520	1.604
butadiene														
	1^3B_u	V	$\pi \rightarrow \pi^*$	3.22	0.071	-0.265	-0.319	-0.314	-0.282	-0.739	-0.366	-0.540	-0.365	2.778
	1^3A_g	V	$\pi \rightarrow \pi^*$	4.91	0.532	0.083	0.071	0.077	0.091	-0.237	0.009	-0.095	0.012	2.225
	1^3A_u	R	3p	6.81	-0.789	-1.197	-1.070	-1.001	-1.474	-0.408	-0.814	-0.556	-0.817	-0.343
cyclopentadiene														
	1^3B_2	V	$\pi \rightarrow \pi^*$	3.10	0.153	-0.201	-0.230	-0.221	-0.197	-0.623	-0.283	-0.413	-0.282	2.210
ethylene														
	1^3B_{3u}	R	3s	6.98	-0.235	-0.725	-0.600	-0.534	-0.967	0.005	-0.358	-0.119	-0.361	0.153
	1^3B_{1u}	R	3p	7.79	-0.844	-0.647	-0.807	-0.799	-0.612	0.120	-0.328	-0.401	-0.309	0.397
	1^3A_g	R	3p	8.15	0.234	-0.215	-0.238	-0.117	-0.367	0.338	0.070	0.215	0.048	0.887
formaldehyde														
	1^3A_2	V	$n \rightarrow \pi^*$	3.50	-0.355	-0.380	-0.407	-0.420	-0.289	-0.079	-0.248	-0.276	-0.244	0.552
	1^3B_2	R	3s	6.83	-0.945	-1.199	-1.181	-1.150	-1.453	0.397	-0.482	-0.301	-0.453	0.170
	2^3B_2	R	3p	7.79	-0.693	-0.961	-0.967	-0.885	-1.282	0.392	-0.361	-0.165	-0.357	0.140
	2^3A_1	R	3p	7.96	-1.104	-1.392	-1.349	-1.328	-1.657	0.295	-0.645	-0.455	-0.599	0.032
	2^3A_2	R	3p	8.31	-0.399	-0.669	-0.645	-0.588	-1.069	0.851	-0.004	0.211	0.016	0.290
furan														
	1^3B_2	V	$\pi \rightarrow \pi^*$	4.0	0.276	-0.155	-0.132	-0.121	-0.095	-0.485	-0.197	-0.262	-0.194	2.332
	1^3A_1	V	$\pi \rightarrow \pi^*$	5.2	0.379	-0.036	0.017	0.026	0.053	-0.026	0.024	0.036	0.034	1.885
pyrazine														
	1^3B_{3u}	V	$n \rightarrow \pi^*$	3.42	-0.558	-0.512	-0.555	-0.564	-0.448	0.119	-0.221	-0.227	-0.200	0.781
	1^3B_{1u}	V	$\pi \rightarrow \pi^*$	4.04	0.589	0.125	0.118	0.127	0.156	-0.641	-0.037	-0.184	-0.043	2.717
	1^3A_u	V	$n \rightarrow \pi^*$	4.2	-0.455	-0.282	-0.327	-0.337	-0.219	1.094	0.282	0.352	0.327	0.780
	1^3B_{2u}	V	$\pi \rightarrow \pi^*$	4.5	-0.226	-0.491	-0.468	-0.474	-0.461	-0.331	-0.386	-0.388	-0.372	1.076
	1^3B_{2g}	V	$n \rightarrow \pi^*$	4.6	-0.243	-0.317	-0.297	-0.295	-0.154	0.401	0.039	0.108	0.064	1.308
	2^3B_{1u}	V	$\pi \rightarrow \pi^*$	5.7	-0.321	-0.728	-0.645	-0.642	-0.614	-0.453	-0.586	-0.516	-0.571	2.293
pyridine														
	1^3A_1	V	$\pi \rightarrow \pi^*$	4.1	0.483	0.005	0.000	0.009	0.043	-0.689	-0.148	-0.290	-0.152	2.466
	1^3B_2	V	$\pi \rightarrow \pi^*$	4.84	-0.222	-0.473	-0.441	-0.444	-0.423	-0.195	-0.326	-0.301	-0.309	0.860
	1^3A_2	V	$n \rightarrow \pi^*$	5.43	-1.244	-1.109	-1.134	-1.144	-1.025	0.353	-0.504	-0.407	-0.456	0.020
pyrrole														
	1^3B_2	V	$\pi \rightarrow \pi^*$	4.21	0.020	-0.452	-0.388	-0.369	-0.334	-0.862	-0.535	-0.550	-0.534	-0.235

Table S11. continued.

Molecule	State	Type		Expt.	SVWN	BLYP	PW91	PBE	OLYP	BHHLYP	B3LYP5	PBE0	X3LYP	CAM-B3LYP
s-tetrazine														
	1^3B_{3u}	V	n→π*	1.69	-0.606	-0.506	-0.578	-0.580	-0.473	-0.298	-0.286	-0.328	-0.270	0.754
	1^3A_u	V	n→π*	2.90	-0.581	-0.340	-0.430	-0.441	-0.329	0.064	0.110	0.123	0.144	0.821
	1^3B_{1g}	V	n→π*	3.6	-0.368	-0.252	-0.274	-0.266	-0.121	0.067	0.053	0.088	0.072	1.444
	1^3B_{2u}	V	n→π*	4.2	0.201	-0.148	-0.082	-0.083	-0.078	0.137	-0.040	-0.004	-0.026	1.684
	2^3A_u	V	n→π*	4.6	-0.477	-0.516	-0.514	-0.522	-0.389	0.208	0.023	-0.659	0.069	1.038
s-trans glyoxal														
	1^3A_u	V	n→π*	2.5	-0.925	-0.874	-0.946	-0.961	-0.839	-0.234	-0.569	-0.606	-0.548	0.326
	1^3B_g	V	n→π*	3.8	-0.732	-0.708	-0.746	-0.761	-0.598	0.040	-0.320	-0.307	-0.299	0.625
	1^3B_u	V	π→π*	5.2	-0.191	-0.613	-0.597	-0.595	-0.540	-1.069	-0.676	-0.774	-0.682	2.994
water														
	1^3B_1	R	3s	7.0	-0.702	-1.072	-0.988	-0.939	-1.234	0.264	-0.463	-0.204	-0.451	0.227
	1^3A_2	R	3p	8.9	-0.914	-1.358	-1.177	-1.184	-1.596	0.235	-0.631	-0.332	-0.587	-0.094
	1^3A_1	R	3s	9.3	-1.048	-1.358	-1.261	-1.197	-1.414	0.011	-0.744	-0.458	-0.730	0.055

Table S12. Errors (eV) in TD-DFT singlet vertical excitation energies for metaGGAs relative to experimental value (Error = $E_{TD\text{-}DFT} - E_{Experiment}$).

Molecule	State	Type		Expt.	VS98	PKZB	TPSS	M06-L	TPSSm	revTPSS	TPSSh	M05	M05-2X	M06	M06-2X	M06-HF	M08-HX	M08-SO
butadiene																		
	1^1B_u	V	π→π*	5.92	-0.335	-0.472	-0.384	-0.188	-0.401	-0.335	-0.266	-0.367	0.009	-0.375	-0.017	0.064	-0.097	-0.220
	1^1B_g	R	3s	6.21	-0.333	-0.686	-0.521	-0.289	-0.563	-0.370	-0.354	-0.321	0.484	-1.132	-0.155	-0.300	-0.653	-0.735
	1^1A_u	R	3p	6.64	-0.555	-0.870	-0.670	-0.473	-0.714	-0.514	-0.499	-0.499	0.358	-1.360	-0.334	-0.471	-0.847	-0.928
	2^1A_u	R	3p	6.80	-0.580	-0.969	-0.786	-0.575	-0.830	-0.627	-0.594	-0.512	0.371	-1.372	-0.309	-0.378	-0.810	-0.891
ethylene																		
	1^1B_{3u}	R	3s	7.11	-0.266	-0.625	-0.434	-0.182	-0.479	-0.274	-0.268	-0.312	0.487	-1.051	-0.109	-0.314	-0.595	-0.697
	1^1B_{1g}	R	3p	7.80	-0.071	-0.232	-0.136	0.108	-0.160	-0.065	-0.071	-0.353	-0.003	-0.424	-0.049	-0.224	-0.184	-0.365
	1^1B_{1u}	V	π→π*	7.66	-0.324	-0.756	-0.545	-0.401	-0.590	-0.381	-0.372	-0.364	0.297	-1.273	-0.246	-0.463	-0.724	-0.848
	1^1B_{2g}	R	3p	8.0	-0.561	-0.996	-0.788	-0.584	-0.836	-0.617	-0.590	-0.528	0.411	-1.447	-0.340	-0.444	-0.830	-0.951
formaldehyde																		
	1^1A_2	V	n→π*	4.07	0.027	-0.126	-0.012	0.341	-0.023	0.024	0.049	-0.093	-0.297	-0.064	-0.309	-0.931	-0.306	-0.437
	1^1B_2	R	3s	7.11	-0.886	-1.294	-0.996	-0.654	-1.043	-0.820	-0.653	-0.599	0.609	-1.122	0.029	0.351	-0.582	-0.475
	2^1B_2	R	3p	7.97	-0.411	-0.951	-0.672	-0.352	-0.720	-0.496	-0.386	-0.368	0.683	-1.085	0.029	0.329	-0.560	-0.493
	2^1A_1	R	3p	8.14	-0.989	-1.435	-1.128	-0.876	-1.172	-0.952	-0.775	-0.646	0.620	-1.298	-0.037	0.352	-0.664	-0.554
	2^1A_2	R	3p	8.37	-0.026	-0.699	-0.413	-0.179	-0.460	-0.226	-0.105	0.001	1.167	-1.029	0.258	0.611	-0.356	-0.326
furan																		
	1^1A_2	R	3s	5.91	-0.193	-0.620	-0.416	-0.220	-0.463	-0.246	-0.237	-0.155	0.631	-0.983	-0.039	-0.126	-0.568	-0.598
	1^1B_2	V	π→π*	6.06	0.021	-0.145	-0.061	0.136	-0.081	-0.004	0.045	-0.021	0.323	-0.204	0.209	0.248	0.074	-0.065
	1^1B_1	R	3p	6.48	-0.318	-0.765	-0.556	-0.386	-0.603	-0.384	-0.369	-0.215	0.604	-1.139	-0.137	-0.223	-0.659	-0.705
	2^1B_2	R	3p	6.48	0.984	0.577	0.688	1.043	0.642	0.841	0.824	0.800	1.514	0.180	0.929	0.860	0.409	0.360
	2^1A_2	R	3p	6.61	-0.242	-0.739	-0.522	-0.396	-0.569	-0.346	-0.325	-0.135	0.765	-1.179	-0.088	-0.107	-0.605	-0.671
	3^1B_1	R	3s	7.38	-0.381	-0.832	-0.630	-0.369	-0.677	-0.464	-0.374	-0.158	0.772	-1.075	0.032	0.126	-0.520	-0.545
pyrrole																		
	1^1A_2	R	3s	5.22	-0.094	-0.506	-0.330	-0.043	-0.375	-0.173	-0.149	-0.017	0.664	-0.842	0.000	-0.153	-0.594	-0.573
	2^1B_1	R	3p	5.86	0.044	-0.367	-0.170	0.046	-0.213	-0.007	0.006	0.160	0.640	-0.744	0.183	0.034	-0.386	-0.398
	2^1B_2	V	π→π*	5.98	0.021	-0.134	-0.053	0.129	-0.073	-0.001	0.039	-0.036	0.253	-0.243	0.125	0.047	-0.084	-0.176
s-tetrazine																		
	1^1B_{3u}	V	n→π*	2.25	-0.217	-0.272	-0.246	-0.195	-0.243	-0.247	-0.092	-0.407	-0.007	-0.219	0.001	-0.032	0.114	-0.048
	1^1A_u	V	n→π*	3.4	-0.335	-0.403	-0.331	-0.255	-0.330	-0.320	-0.088	-0.317	0.373	-0.161	0.295	0.677	0.367	0.239
	1^1B_{2u}	V	π→π*	4.97	0.684	0.509	0.574	0.727	0.557	0.618	0.716	0.704	1.043	0.683	0.980	1.240	1.075	0.874
	2^1A_u	V	n→π*	5.0	-0.104	-0.256	-0.143	-0.045	-0.150	-0.120	0.132	0.046	0.660	0.122	0.559	0.994	0.656	0.498

Table S12. continued.

Molecule	State	Type		Expt.	VS98	PKZB	TPSS	M06-L	TPSSm	revTPSS	TPSSh	M05	M05-2X	M06	M06-2X	M06-HF	M08-HX	M08-SO
s-trans acrolein																		
	$1^1A''$	V	n→π*	3.71	-0.289	-0.489	-0.385	-0.135	-0.395	-0.348	-0.166	-0.056	-0.006	-0.022	-0.020	-0.393	-0.007	-0.082
s-trans glyoxal																		
	1^1A_u	V	n→π*	2.8	-0.382	-0.544	-0.452	-0.225	-0.459	-0.423	-0.271	-0.235	-0.193	-0.169	-0.152	-0.520	-0.138	-0.211
	1^1B_g	V	n→π*	4.63	-0.698	-0.863	-0.794	-0.442	-0.800	-0.773	-0.519	-0.359	-0.418	-0.338	-0.390	-0.901	-0.357	-0.488
	2^1B_g	V	n→ π*	7.45	-1.893	-2.152	-1.989	-1.593	-2.009	-1.925	-1.632	-1.406	-0.491	-1.348	-0.546	0.167	-0.737	-0.643
	1^1B_u	R	3p	7.9	-1.272	-1.700	-1.373	-1.094	-1.426	-1.177	-1.015	-0.928	0.366	-1.411	-0.220	0.176	-0.816	-0.691
water																		
	1^1B_1	R	3s	7.4	-0.484	-0.994	-0.742	-0.231	-0.790	-0.573	-0.437	-0.288	0.521	-0.816	0.001	-0.041	-0.465	-0.429
	1^1A_2	R	3p	9.1	-0.663	-1.333	-1.048	-0.814	-1.097	-0.865	-0.700	-0.362	0.535	-1.330	-0.195	-0.220	-0.716	-0.703
	2^1A_1	R	3s	9.7	-0.602	-1.026	-0.849	-0.374	-0.882	-0.730	-0.549	-0.387	0.439	-1.027	-0.094	-0.038	-0.562	-0.631
	1^1B_2	R	3p	11.05	-0.441	-1.043	-0.830	-0.631	-0.864	-0.691	-0.488	-0.133	0.810	-1.245	0.009	0.122	-0.478	-0.600

References

1. Runge, E.; Gross, E. K. U. *Phys. Rev. Lett.* **1984**, 52, 997-1000.
2. Gross, E. K. U.; Kohn, W. *Adv. Quantum. Chem.* **1990**, 21, 255-291.
3. van Leeuwen, R. *Int. J. Mod. Phys. B* **2001**, 15, 1969-2023.
4. Casida, M. E., Time-dependent density-functional response theory for molecules. In *Recent Advances in Density Functional Methods*, Chong, D. P. Eds.; Recent Advances in Computational Chemistry; World Scientific: Singapore, 1995; 1, pp. 155-192.
5. Casida, M. E., Time-Dependent Density Functional Response Theory of Molecular Systems: Theory, Computational Methods, and Functionals. In *Recent Developments and Applications of Modern Density Functional Theory, Theoretical and Computational Chemistry*, Seminario, J. M. Eds.; Elsevier: Amsterdam, 1996, pp. 391-439.
6. Chiba, M.; Federov, D. G.; Kitaura, K. The Fragment Molecular Orbital-Based Time-Dependent Density Functional Theory for Excited States in Large Systems. In *The Fragment Molecular Orbital Method: Practical Applications to Large Molecular Systems*; Federov, D. G., Kitaura, K., Eds.; CRC Press, Boca Raton, Fl., **2009**; pp. 91-118.
7. A. D. Becke, *J. Chem. Phys.* **1993**, 98, 5648-5642.
8. P. J. Stephens, F. J. Devlin, C. F. Chablowski, M. J. Frisch, *J. Phys. Chem.* **1994**, 98, 11623-11627.
9. R. H. Hertwig, W. Koch, *Chem. Phys. Lett.* **1997**, 268, 345-351.
10. J. P. Perdew, K. Burke, M. Ernzerhof, *Phys. Rev. Lett.* **1996**, 77, 3865-3868.
11. J. P. Perdew, K. Burke, M. Ernzerhof, *Phys. Rev. Lett.* **1997**, 78, 1396.
12. C. Adamo, V. Barone, *J. Chem. Phys.* **1999**, 110, 6158-6170.
13. T. V. Voorhis, G. E. Scuseria, *J. Chem. Phys.* **1998**, 109, 400-410.
14. J. P. Perdew, S. Kurth, A. Zupan, P. Blaha, *Phys. Rev. Lett.* **1999**, 82, 2544-2547.
15. J. P. Perdew, J. Tao, V. N. Staroverov, G. E. Scuseria, *Phy. Rev. Lett.* **2003**, 91, 146401-1-146401-4.
16. J. P. Perdew, J. Tao, V. N. Staroverov, G. E. Scuseria, *J. Chem. Phys.* **2004**, 120, 6898-6911.
17. Y. Zhao, D. G. Truhlar, *J. Chem. Phys.* **2006**, 125, 194101-1-194101-18.
18. J. P. Perdew, A. Ruzsinszky, J. Tao, G. I. Csonka, G. E. Scuseria, *Phys. Rev. A* **2007**, 76, 042506-1-042506-6.
19. J. P. Perdew, A. Ruzsinszky, G. I. Csonka, L. A. Constantin, J. Sun, *Phys. Rev. Lett.* **2009**, 103, 026403-1-026403-4.
20. V. N. Staroverov, G. E. Scuseria, J. Tao, J. P. Perdew, *J. Chem. Phys.* **2003**, 119, 12129-12137.
21. V. N. Staroverov, G. E. Scuseria, J. Tao, J. P. Perdew, *J. Chem. Phys.* **2004**, 121, 11507.
22. Y. Zhao, N. E. Schultz, D. G. Truhlar, *J. Chem. Phys.* **2005**, 123, 161103-1-161103-4.
23. Y. Zhao, D. G. Truhlar, *J. Comput. Chem. Theory Comput.* **2006**, 2, 1009-1018.
24. Y. Zhao, D. G. Truhlar, *Theo. Chem. Acc.*, **2008**, 120, 215-241.
25. Y. Zhao, D. G. Truhlar, *J. Phys. Chem. A*, **2006**, 110, 13126-13130.
26. Y. Zhao, D. G. Truhlar, *J. Chem. Theory Comput.* **2008**, 4, 1849-1868.

27. Strange, R.; Manby, F. R.; Knowles, P. J. *Comput. Phys. Comm.* **2001**, 136, 310-318.
28. Mattson, A. E. *Science* **2002**, 298, 759-760.
29. Jacquemin, D.; Perpète, E. A.; Ciofini, I.; Adamo, C.; Valero, R.; Zhao, Y.; Truhlar, D. G. *J. Chem. Theory Comput.* **2010**, 6, 2071-2085.
30. Sorkin, A.; Iron, M. A.; Truhlar, D. G. *J. Chem. Theory Comput.* **2008**, 4, 307-315.
31. Tao, J.; Tretiak, S.; Zhu, J.-X. *J. Chem. Phys.* **2008**, 128, 084110-1-084110-8.
32. Cui, G.; Yang, W. *Mol. Phys.* **2010**, 108, 2745-2750.
33. Jacquemin, D.; Perpete, E. A.; Ciofini, I.; Adamo, C. *J. Chem. Theory Comput.* **2010**, 6, 1532-1537.
34. Guido, C. A.; Jacquemin, D.; Adamo, C.; Benedetta, M. *J. Phys. Chem. A* **2010**, 114, 13402-13410.
35. Plötner, J.; Tozer, D. J.; Dreuw, A. *J. Chem. Theory Comput.* **2010**, 6, 2315-2324.
36. Caricato, M.; Trucks, G. W.; Frisch, M. J.; Wiberg, K. B. *J. Chem. Theory Comput.* **2010**, 6, 370-383.
37. Perpète, E. A.; Jacquemin, D. *J. Mol. Struct.: (THEOCHEM)* **2009**, 914, 100-105.
38. Goerigk, L.; Moellmann, J.; Grimme, S. *Phys. Chem. Chem. Phys.* **2009**, 11, 4611-4620.
39. Jacquemin, D.; Wathelet, V.; Perpète, E. A.; Adamo, C. *J. Chem. Theory Comput.* **2009**, 5, 2420-2435.
40. Jacquemin, D.; Perpète, E. A.; Scuseria, G. E.; Ciofini, I.; Adamo, C. *J. Chem. Theory Comput.* **2008**, 4, 123-135.
41. Zhao, Y.; Truhlar, D. G. *J. Phys. Chem. A* **2006**, 110, 13126-13130.
42. Silva-Junior, M. R.; Schreiber, M.; Sauer, S. P. A.; Thiel, W. *J. Chem. Phys.* **2008**, 129, 104103-1-104103-14.
43. Hirata, S.; Head-Gordon, M. *Chem. Phys. Lett.* **1999**, 314, 291-299.
44. Krishnan, R.; Binkley, J. S.; Seeger, R.; Pople, J. A. *J. Chem. Phys.* **1980**, 72, 650-654.
45. Frisch, M. J.; Pople, J. A.; Binkley, J. S. *J. Chem. Phys.* **1984**, 80, 3265-3269.
46. Clark, T.; Chandrasekhar, J.; Spitznagel, G. W.; Schleyer, P. V. R. *J. Comp. Chem.* **1983**, 4, 294-301.
47. Feller, D., *J. Comp. Chem.* **1996**, 17, 1571-1586.
48. Schuchardt, K.L.; Didier, B.T.; Elsethagen, T.; Sun, L.; Gurumoorthi, V.; Chase, J.; Li, J.; Windus, T.L.D *J. Chem. Info. Model* **2007**, 47, 1045-1052.
49. Murray, C. W.; Handy, N. C.; Laming, G. J. *Mol. Phys.* **1993**, 78, 997-101.
50. Lebedev, V. I.; Laikov, D. N. *Dokl. Math.* **1999**, 59, 477-481.
51. Chiba, M.; Tsuneda, T.; Hirao, K. *J. Chem. Phys.* **2006**, 124, 144106-1-144106-11.
52. Peach, M. J. G.; Benfield, P.; Helgaker, T.; Tozer, D. J. *J. Chem. Phys.* **2008**, 128, 044118-1-044118-8.
53. Peach, M. J. G.; Sueur, C. R. L.; Ruud, K.; Guillaume, M.; Tozer, D. J. *Phys. Chem. Chem. Phys.* **2009**, 11, 4465-4470.
54. Peach, M. J. G.; Tozer, D. J. *J. Mol. Struct.: THEOCHEM* **2009**, 914, 110-114.
55. Wiggins, P.; Williams, J. A. G.; Tozer, D, J. *J. Chem. Phys.* **2009**, 131, 091101-1-091101-4.
56. Dwyer, A. D.; Tozer, D. J. *Phys. Chem. Chem. Phys.* **2010**, 12, 2816-2818.
57. Gordon, M. S.; Schmidt, M. W. Advances in Electronic Structure Theory: GAMESS: A Decade Later. In *Theory and Applications of Computational Chemistry: The First*

Forty Years; Dykstra, C. E., Frenking, G., Kim, K. S., Scuseria, G. E., Eds.; Elsevier, Amsterdam, **2005**; pp. 1167-1189.
58. Bode, B. M.; Gordon, M. S. *J. Mol. Graphics Mod.* **1998**, 16, 133-138.
59. Sension, R. J.; Hudson, B. S. *J. Chem. Phys.* **1989**, 90, 1377-1389.
60. Foresman, J. B.; Head-Gordon, M.; Pople, J. A.; Frisch, M. J. *J. Phys. Chem.* **1992**, 96, 135-149.
61. Wilberg, K. B.; Hadad, C. M.; Foresman, J. B.; Chupka, W. A. *J. Phys. Chem.* **1992**, 96, 10756-10768.
62. Serrano-Andrés, L.; Merchán, M.; Nebot-Gil, I.; Roos, B. O.; Fülscher, M. *J. Am. Chem. Soc.* **1993**, 115, 6184-6197.
63. Hirao, K.; Hashimoto, N. T. *Chem. Phys. Lett.* **1995**, 235, 430-435.
64. Gwaltney, S. R.; Nooijen, M.; Bartlett, R. J. *Chem. Phys. Lett.* **1996**, 248, 189-198.
65. Nakano, H.; Tsuneda, T.; Hashimoto, T.; Hirao, K. *J. Chem. Phys.* **1996**, 104, 2312-2320.
66. Watts, J. D.; Gwaltney, S. R.; Bartlett, R. J. **1996**, 105, 6979-6988.
67. Bene, J. E.; Watts, J. D.; Bartlett, R. J. *J. Chem. Phys.* **1997**, 106, 6051-6060.
68. Andrejkovics, I.; Nagy, Á. *Chem. Phys. Lett.* **1998**, 296, 489-493.
69. Stratmann, R. E.; Scuseria, G. E.; Frisch, M. J. *J. Chem. Phys.* **1998**, 109, 8218-8224.
70. Nakajima, T.; Nakatsuji, H. *Chem. Phys.* **1999**, 242, 177-193.
71. Nakajima, T.; Nakatsuji, H. *Chem. Phys. Lett.* **1999**, 300, 1-8.
72. Hirata, S.; Head-Gordon, M. *Chem. Phys. Lett.* **1999**, 314, 291-299.
73. Adamo, C.; Scuseria, G. E.; Barone, V. *J. Chem. Phys.* **1999**, 2889-2899.
74. Handy, N. C.; Tozer, D. J. *J. Comp. Chem.* **1999**, 20, 106-113.
75. Rubio, M.; Roos, B. O. *Mol. Phys.* **1999**, 96, 603-615.
76. Adamo, C.; Barone, V. *Chem. Phys. Lett.* **2000**, 330, 152-160.
77. Weber, P.; Reimers, J. R. *J. Phys. Chem. A* **1999**, 103, 9821-9829.
78. Cai, Z.-L.; Tozer, D. J.; Reimers, J. R. *J. Chem. Phys.* **2000**, 113, 7084-7096.
79. Cai, Z.-L.; Reimers, J. R. *J. Phys. Chem. A.* **2000**, 104, 8389-8408.
80. Nooijen, M. *J. Phys. Chem. A* **2000**, 104, 4553-4561.
81. Wan, J.; Hada, M.; Ehara, M.; Nakatsuji, H. *J. Chem. Phys.* **2001**, 114, 5117-5123.
82. Head, J. D. *Int. J. Quant. Chem.* **2003**, 95, 580-592.
83. Aquilante, V.; Barone, V.; Roos, B. O. *J. Chem. Phys.* **2003**, 119, 12323-12334.
84. Hirata, S.; Zhan, C.-G.; Aprà, E.; Windus, T. L.; Dixon, D. A. *J. Phys. Chem. A* **2003**, 107, 10154-10158.
85. Pitarch-Ruiz, J.; Sanchez-Marin, J.; Meras, A. S. D.; Maynau, D. *Mol. Phys.* **2003**, 101, 483-494.
86. Cave, R. J.; Zhang, F.; Maitra, N. T.; Burke, K. *Chem. Phys. Lett.* **2004**, 389, 39-42.
87. Parac, M.; Grimme, S. *J. Phys. Chem. A* **2002**, 106, 6844-6850.
88. Faassen, M. van; Boeji, P. L. de *J. Chem. Phys.* **2004**, 120, 8353-8363.
89. Jacquemin, D.; Perpète, E. A.; Scalmani, G.; Frisch, M. J.; Ciofini, I.; Adamo, C. *Chem. Phys. Lett.* **2006**, 421, 272-276.
90. Miura, M.; Aoki, Y.; Champange, B. *J. Chem. Phys.* **2007**, 127, 084103-1-084103-16.
91. Li, Y.; Wan, J.; Xu, X. *J. Comp. Chem.* **2007**, 28, 1658-1667.
92. Fukuda, R.; Nakatsuji, H. *J. Chem. Phys.* **2008**, 094105-1-094105-14.
93. Rubio, M.; Serrano-Andrés, L.; Merchán, M. *J. Chem. Phys.* **2008**, 128, 104305.

94. Yamamoto, S.; Tatewaki, H.; Diercksen, G. H. F. *Int. J. Quant. Chem.* **2004**, 103, 45-53.
95. Musial, M.; Bartlett, R. J. *J. Chem. Phys.* **2007**, 127, 024106-1-024106-9
96. Tozer, D. J.; Handy, N. C. *J. Chem. Phys.* **1998**, 109, 10180-10189.
97. Casida, M. E.; Jamorski, C.; Casida, K. C.; Salahub, D. R. *J. Chem. Phys.* **1998**, 108, 4439-4449.
98. Tozer, D. J.; Amos, R. D.; Handy, N. C.; Roos, B. O.; Serrano-Andres, L. *Mol. Phys.* **1999**, 97, 859-868.
99. J. C. Slater *Phys. Rev.* **1951**, 81, 385-390.
100. S. H. Vosko, L. Wilk, M. Nusair, *Can. J. Phys.* **1980**, 58, 1200-1211.
101. A. D. Becke, *Phys. Rev. A* **1988**, 38, 3098-3100.
102. C. Lee, W. Yang, R. G. Parr, *Phys. Rev. B* **1988**, 37, 785-789.
103. J. P. Perdew, Y. Wang, *Phys. Rev. B* **1992**, 45, 13244-13249.
104. J. P. Perdew, J. A. Chevray, S. H. Vosko, K. A. Jackson, M. R. Pederson, D. J. Singh, C. Fiolhais, *Phys. Rev. B* **1992**, 46, 6671-6687.
105. N. C. Handy, A. J. Cohen, *Mol. Phys.* **2001**, 99, 403-412.
106. A. D. Becke, *J. Chem. Phys.* **1993**, 98, 1372-1377.
107. X. Xu, Q. Zhang, R. P. Muller, W. A. Goddard, *J. Chem. Phys.* **2005**, 122, 014105-1-014105-14.
108. T. Yanai, D. P. Tew, N. C. Handy, *Chem. Phys. Lett.* **2004**, 393, 51-57.
109. Hiraya, A.; Sobatake, K. *J. Chem. Phys.* **1991**, 94, 7700-7706.
110. Nakashima, N.; Inoue, H.; Sumitani, M.; Yoshihara, K. *J. Chem. Phys.* **1980**, 73, 5976-5980.
111. Johnson, P. M. *J. Chem. Phys.* **1976**, 64, 4143-4148.
112. Whetten, R. L.; Grubb, S. G.; Otis, C. E.; Albrecht, A. C.; Grant, E. R. *J. Chem. Phys.* **1985**, 82, 1115-1134.
113. Johnson, P. M.; Korenowski, G. M. *Chem. Phys. Lett.* **1983**, 97, 53-56
114. Doering, J. P. *J. Chem. Phys.* **1969**, 51, 2866-2870.
115. Flicker, W. M.; Mosher, O. A.; Kupperman, A. *Chem. Phys.* **1978**, 30, 307-314.
116. Doering, J. P.; McDiarmid, R. *J. Chem. Phys.* **1981**, 75, 2477-2478
117. Mosher, O. A.; Flicker, W. M.; Kupperman, A. *J. Chem. Phys.* **1973**, 59, 6502-6511.
118. Saha, B.; Ehara, M.; Nakatsuji, H. *J. Chem. Phys.* **2006**, 125, 014316-1-014316-14.
119. Price, W. C.; Walsh, A. D. *Proc. R. Soc. London Ser. A* **1941**, 179, 201-214.
120. McDiarmid, R.; Sabljić, A. *J. Phys. Chem.* **1991**, 95, 6455-6462.
121. Sabljic, A.; McDiarmid, R.; Gedanken, A. *J. Phys. Chem.* **1992**, 96, 2442-2448.
122. McDiarmid, R.; Sabljić, A.; Doering, J. P. *J. Chem. Phys.* **1985**, 83, 2147-2152.
123. Derrick, P. J.; Asbrink, L.; Edqvist, O.; Jonsson, B. O.; Lindholm, E. *Int. J. Mass. Spectrom. Ion Phys.* **1971**, 6, 203-215.
124. Frueholz, R. P.; Flicker, W. M.; Mosher, O. A.; Kupperman, A. *J. Chem. Phys.* **1979**, 70, 2003-2013.
125. Serrano-Andres, L.; Merchan, M.; Nebot-Gil, I.; Lindh, R.; Roos, B. O. *J. Chem. Phys.* **1993**, 98, 3151-3162.
126. Robin, M. B. *Higher Excited States of Polyatomic Molecules*, Academic Press, New York, **1985.**
127. Flicker, W. M.; Mosher, O. A.; Kupperman, A. *J. Chem. Phys.* **1976**, 64, 1315-1321.

128. Derrick, P. J.; Åsbrink, L.; Edqvist, O.; Jonsson, B.-Ö.; Lindholm *Int. J. Mass. Spectrom. Ion Phys.* **1971**, 6, 161-175.
129. Van Veen, E. H. *Chem. Phys. Lett.* **1976**, 41, 535-539.
130. Staley, S. W.; Norden, T. D. *J. Am. Chem. Soc.* **1984**, 106, 3699-3700.
131. Hackmeyer, H.; Whitten, J. L. *J. Chem. Phys.* **1971**, 54, 3739-3750.
132. Wadt, W. R.; Goddard, W. A.; Dunning, T. H. *J. Chem. Phys.* **1976**, 65, 438-445.
133. Bolovinos, A.; Tsekeris, P.; Philis, J.; Pantons, E.; Andritsopoulos *J. Mol. Spectrosc* **1984**, 103, 240-256.
134. Walker, I. C.; Palmer, M. H. *Chem. Phys.* **1991**, 153, 169-187.
135. Walker, I. C.; Palmer, M. H.; Hopkirk, A. *Chem. Phys.* **1989**, 141, 365-378.
136. Bavia, M.; Bertinelli, F.; Taliani, C.; Zauli, C. *Mol. Phys.***1976**, 31, 479-489.
137. Horvath, G.; Kiss, A. I. *Spectrochim. Acta A* **1967**, 23, 921-924.
138. Flicker, W. M.; Mosher, O. A.; Kupperman, A. *Chem. Phys. Lett.* **1976**, 38, 489-492.
139. Innes, K. K. *J. Mol. Spectrosc.* **1988**, 132, 492-544.
140. Innes, K. K. *J. Mol. Spectrosc.* **1988**, 129, 140-144.
141. Palmer, M. H.; McNab, H.; Reed, D.; Pollacchi, A.; Walker, I. C.; Guest, M. F.; Siggel, R. F. *Chem. Phys.* **1997**, 191-211
142. Becker, R. S.; Inuzuka, K.; King. J. *J. Chem. Phys.* **1970**, 52, 5164-5170.
143. Verhaart, G. J.; Brongersma, H. H. *Chem. Phys. Lett.* **1980**, 72, 176-180.
144. McMurry, H. L. *J. Chem. Phys.* **1941**, 9, 231-240
145. Chutjian, A.; Trajmer, S.; Hall, R. I. *J. Chem. Phys.* **1975**, 63, 892-898
146. Ishiguro, E.; Sasanuma, M.; Masuko, H.; Morioka, Y.; Nakamura, M. *J. Phys. B* **1978**, 11, 993-1010.

CHAPTER 5. A COMBINED COUPLED-CLUSTER/EFFECTIVE FRAGMENT POTENTIAL APPROACH TO SOLVENT EFFECTS

A paper to be submitted to *The Journal of Chemical Physics*

Sarom Sok[†], Lyudmila V. Slipchenko[‡], Mark S. Gordon[†]

Abstract

The effective fragment potential method (EFP) is interfaced with coupled-cluster (CC) theory for both the ground and electronically excited states in a hybrid quantum mechanics/molecular mechanics (QM/MM) scheme to treat solvent effects. The optimization of the solvent polarization is limited to the reference state, since it has been demonstrated previously that this provides the vast majority of the solvent-solute induction interaction. The computational cost of the new CC/EFP method is nearly the same as single gas-phase CC calculation on the QM region. The CC/EFP method is applied to the study of the neutral hydrolysis mechanism of 1-methylsilatrane and the solvation of the hydroxyl and nitrate anion. Comparisons are made to fully *ab initio* calculations in which the solvent molecules are treated quantum mechanically with CC theory. The applicability and accuracy of the CC/EFP method is also used to calculate the solvent-induced shift of the $\pi \rightarrow \pi^*$ charge-transfer excited state of *p*-nitroaniline in water and compared to reported experimental values.

1. Introduction

Coupled-cluster (CC) theory [1-3] offers an attractive approach for capturing dynamic correlation, by considering n-body interactions in a systematic manner [4]. Use of an exponential *ansatz* allows truncated CC methods to approach the exact wavefunction for a given atomic basis set [5], while retaining size consistency and size extensivity. [6]. As a

[†]Department of Chemistry and Ames Laboratory, Iowa State University, Ames, Iowa 50011
[‡]Department of Chemistry, Purdue University, West Lafayette, Indiana 47907

result, CC theory has become the single-reference electronic structure method of choice for obtaining accurate ground- and excited-state molecular energies and properties of chemical systems at or near equilibrium in the gas phase. However, a majority of chemical phenomena occur in solution and the effect of the surrounding environment (solvent) needs to be considered to accurately model chemical systems in the condensed-phase [7,8]. Efficient methods for modeling solvent effects are needed, because the direct treatment of solvent molecules using a supermolecular approach is precluded by the computationally prohibitive formal scaling of popular CC methods, e.g., CCSD (coupled-cluster with single and double excitations) (N^6) [9] and CCSD(T) (coupled-cluster with single and double excitations plus perturbative triple excitation corrections) (N^7) [10], where N is a measure of the system size in terms of basis functions (BF).

Two common methods for modeling solvent effects are continuum and discrete approaches. Both methods feature partitioning of the chemical system into two regions that are treated at different levels of accuracy: the chemically active (solute) region, treated with some level of quantum mechanics, and the solvent region, modeled using continuum or discrete base methods that are usually classical or semi-classical in nature.

Continuum based methods place the solute in a molecular cavity surrounded by a homogeneous dielectric medium representing the solvent [11,12]. Continuum based methods are computationally efficient, reasonably accurate for bulk properties of the solvent, and do not require configurational sampling [13]. The weaknesses of continuum based methods are sensitivity to cavitation parameters and inability to treat specific solute-solvent interactions due to the implicit nature of the solvent, such as hydrogen bonding [14,15]. Moreover, a consequence of the implicit averaging of solvent configurations introduced by the use of a homogeneous dielectric medium in continuum based methods is the absence of line broadening in the calculation of molecular properties due to solvent fluctuations.

Discrete methods treat each solvent molecule explicitly, retain the structural nature of the solvent molecules and take into account specific solute-solvent interactions. The balance between computational complexity and accuracy of discrete methods is dependent on the level of sophistication and empiricism of the model potentials used. Bulk features of the solvent are frequently obtained using molecular dynamics (MD) or Monte Carlo (MC)

simulations through a hybrid quantum mechanics/molecular mechanics (QM/MM) scheme [16-20]. Discrete methods explicitly average solvent effects, requiring sufficient sampling of configurations and potentially becoming a bottleneck as the size of the environment increases; therefore, accurate and computationally efficient discrete solvation approaches are necessary. Because of the inherent statistical nature of solutions [21], discrete methods offer an attractive compromise between accuracy and computational tractability, especially when the solvent-solute interactions include hydrogen bonding.

The effective fragment potential (EFP) method is a discrete QM-based method for modeling environmental effects [22-27]. The original EFP method (EFP1) was designed to model the condensed-phase of water and has been successfully applied to the study of chemical reactions in aqueous solution [28-31], ion solvation relevant to atmospheric and biological processes [32,33], the dipole moment of water [34], environmental effects on biomolecules [35-38], and solvent induced shifts of organic chromophores [39-42] [43]. The EFP1 method consists of three terms added as one-electron contributions to the quantum mechanical Hamiltonian of the solute: Coulomb (electrostatic), polarization (induction), and a remainder term to capture all interactions not accounted for by the first two terms. The Coulomb and polarization terms are determined from QM calculations on a single water molecule, while the remainder term is fitted to a QM based water dimer potential. In the Hartree-Fock (HF) based EFP1 method, EFP1/HF, the remainder term contains exchange repulsion and charge-transfer interactions [23]. In the density functional theory (DFT) based EFP1 method, EFP1/DFT, the remainder term also includes short-range electron correlation [25]. The computational overhead of including environmental effects with the EFP1 method is accomplished by the use of one-electron potentials to describe the EFP1 interaction terms. The EFP method for water has been interfaced with several QM methods, including HF [23], DFT [25], multi-configurational self-consistent field (MCSCF) [29], time-dependent DFT (TD-DFT) [39,44], singly excited configuration interaction (CIS) [40], equations-of-motion coupled cluster with single and double excitations (EOM-CCSD) [41], singly excited configuration interaction with perturbative doubles correction (CIS(D)) [42], and multi-reference perturbation theory (MRPT) [43].

In the present work, the development of a new hybrid QM/MM scheme in the General Atomic and Molecular Electronic Structure System (GAMESS) quantum chemistry code [45] is presented in which the chemically important QM region is treated with CC theory, and the environment is described using the EFP1 method. In several previous papers on solvent effects on electronic excited states, it has been demonstrated that the response of the ground state (more generally, the reference state) electron density accounts for the vast majority of the solvent-solute interactions (typically more than 95%) [40,44,43]. Therefore, in the approach used here, the effect of solvent polarization due to the EFP1 fragment molecules is included only in the optimization of the reference wavefunction. This approach does not re-equilibriate the solvent polarization with the CC wavefunction and consequently avoids the computational overhead of calculating the CC reduced one-particle density matrix. The accuracy of the CC/EFP1 method is assessed using the hydrolysis mechanism of 1-substituted silatranes and the solvation of the hydroxyl and nitrate anions. The CC/EFP1 approach is also applied to the calculation of the solvatochromic shift of the lowest singlet $\pi\rightarrow\pi^*$ excited state of *p*-nitroaniline (*p*NA) in water.

Silatranes belong to a special class of biologically active heterocyclic pentacoordinated organosilicon compounds [46,47]. The biological and non-biological applications of these species depend on the pronounced hydrolytic stability of 1-substituted silatranes compared to related acyclic analogs [48,49]. The experimental activation energy for the hydrolysis of 1-methylsilatrane in neutral medium is overestimated by second-order perturbation theory (MP2) [50] with solvent effects described by the conductor-like polarizable continuum model [51]. In the latter study, intramolecular hydrogen bonding and the presence of an additional water molecule participating in the hydrolysis process lowers the barrier associated with the rate-determining step in the hydrolysis process. Adding explicit solvent molecules in the calculation of the intrinsic reaction coordinate (IRC) [52] and performing single-point energy calculations on the stationary points along the reaction pathway using the completely renormalized left eigenvalue coupled cluster (CR-CC(2,3)) method of Piecuch *et al.* [53,54] interfaced with EFP1 method may resolve the discrepancies

between experimental and theoretical activation energies associated with the neutral hydrolysis of 1-methylsilatrane.

Solvated anions play an important role in atmospheric and biological processes [55-59]. The chemistry and photochemistry of solvated anions is dependent on the location of the anion relative to the solvent cage, surface vs. interior [60]. Studies on gas-phase solvated anions aim to provide insight that can be extrapolated to the bulk. Of considerable interest is the crossover point from surface to interior solvation [33,61-66]. For the nitrate anion, force field MD calculations predict a crossover point between 300 and 500 waters while fully *ab initio* MP2 calculations suggest the crossover point occurs at a much smaller value, ≈ 32 waters [33]. The relative energies of the global minimum structures for surface and interior solvated cluster of $OH^-(H_2O)_{n=14,16}$ and $NO_3^-(H_2O)_{15}$ are studied using the CCSD(T)/EFP1 method and are compared with fully *ab initio* calculations.

pNA is a prototypical organic push-pull (donor-π-acceptor) chromophore that has been the subject of many theoretical investigations [41,42,67-77]. pNA possesses a strong $\pi\rightarrow\pi^*$ charge-transfer absorption band in the near-ultraviolet to visible region [67]. The peak of the absorption band is strongly dependent on the solvent polarity [70,78]. An experimental red shift of the charge-transfer excited state of -0.98 eV is observed upon going from the gas-, 4.24 eV [78], to the condensed-phase, 3.26 eV [79,80]. Due to the non-local nature of the charge-transfer excited-state, popular hybrid density functionals tend to underestimate the vertical excitation energy in the gas-phase in addition to the solvent shift in water [81]. The underestimation is attributed to the incorrect long-range (non-local) behavior of the exchange functional used [82,83]. QM/MM (CIS(D)/EFP1) studies by Kosenkov and Slipchenko reproduced the red shift in the lowest singlet $\pi\rightarrow\pi^*$ charge-transfer excited state in water to within 0.02 eV of experiment and the spectral line width in the condensed-phase to within 0.14 eV [42]. Here, the accuracy of the CC/EFP1 approach for the excited state is assessed with the calculation of the solvent induced shift of the lowest $\pi\rightarrow\pi^*$ charge-transfer excited state of pNA.

The structure of this article is as follows. In Section 2, the details of the CC/EFP1 method for the ground state are presented. Section 3 describes the computational methods

employed in the current study. Application and assessment of the accuracy of the CC/EFP1 method is presented in Section 4. Concluding remarks are given in Section 5.

2. Theory

The EFP1 method has been discussed in several papers [22,23,25,28], therefore only a brief overview is given here.

The EFP1 method divides the chemical system into two regions: a chemically active region containing the solute plus any desired number of solvent molecules and a solvent region representing the environment. The chemically active region is treated using QM methods and described by a QM Hamiltonian, $\hat{H}_{\mathrm{QM}}$. The solvent region is explicitly modeled using EFP1 fragment molecules. The solute-solvent (QM-EFP1) and solvent-solvent (EFP1-EFP1) interactions are represented by a set of one-electron potentials, $\hat{V}_{\mathrm{QM\text{-}EFP1}}$ and $\hat{V}_{\mathrm{EFP1\text{-}EFP1}}$, respectively, that are added to the QM Hamiltonian:

$$\hat{H}_{\mathrm{system}} = \hat{H}_{\mathrm{QM/EFP1}} = \hat{H}_{\mathrm{QM}} + \hat{V}_{\mathrm{EFP1}} \tag{1}$$

The resulting energy, $\mathrm{E}_{\mathrm{QM/EFP1}}$ is the sum of the energy of the QM region, E_{QM}, and the EFP1 interaction energy, E_{EFP1},

$$E_{\mathrm{QM/EFP1}} = E_{\mathrm{QM}} + E_{\mathrm{EFP1}} \tag{2}$$

The EFP1 interaction energy is defined by the EFP1 interaction potential, $\hat{V}_{\mathrm{EFP1}}$, and contains energy terms for QM-EFP1 and EFP1-EFP1 interactions,

$$E_{\mathrm{EFP1}} = E_{\mathrm{QM\text{-}EFP1}} + E_{\mathrm{EFP1\text{-}EFP1}} \tag{3}$$

The EFP1 interaction potential consists of terms describing Coulomb (Coul), polarization (Pol), and a remainder term (Rem) that capture interactions that are not accounted for in the previous two terms (i.e. exchange repulsion and charge-transfer),

$$\hat{V}_{\mathrm{EFP1}} = \hat{V}^{\mathrm{Coul}} + \hat{V}^{\mathrm{Pol}} + \hat{V}^{\mathrm{Rem}} \tag{4}$$

For the ηth solvent (effective fragment) molecule, the EFP1 interaction potential with an electron in the QM region is given by,

$$\hat{V}_{el}(\eta,s)=\sum_{k=1}^{K}\hat{V}_{k}^{\mathrm{Coul}}(\eta,s)+\sum_{l=1}^{L}\hat{V}_{l}^{\mathrm{Pol}}(\eta,s)+\sum_{m=1}^{M}\hat{V}_{m}^{\mathrm{Rem}}(\eta,s) \quad (5)$$

where s denotes the electronic coordinates. Expressions similar to the right-hand side of Eq. (5) describing nuclear-fragment and fragment-fragment interactions are also added to the Hamiltonian of the entire system. There is no nuclear-fragment interaction analogous to the remainder term since the interactions represented by the latter (i.e. exchange repulsion and charge-transfer) are purely electronic effects.

The first term in Eq. (5) represents the Coulomb interaction and is expressed using a distributed multicenter, multipolar expansion of the fragment molecular density [84,85], carried out through octupole moments. The Coulomb interaction is scaled by a distance-dependent damping term to account for overlapping charge densities at small intermolecular distances. The second term in Eq. (5) represents the polarization, the response in the electronic structure of a molecule due to the presence of an external field (another molecule), and is expressed using localized molecular orbital (LMO) polarizability tensors [23]. The polarization term is iterated until self-consistency is achieved and accounts for many-body effects [27,86,87]. More specifically, the induced dipoles of the EFP1 fragments are first iterated until self-consistency with each other and then iterated with the electronic wavefunction describing the QM region. The last term in Eq. (5) is a remainder term containing interaction energy components not captured by the Coulomb and polarization terms. For QM-EFP interactions, the remainder term is expressed as a linear combination of two simple Gaussian functions, while the fragment-fragment interactions are described using a single exponential. If a HF-based water dimer potential is used, the remainder term will contain exchange repulsion and charge-transfer interactions [23]. If a DFT-based water dimer potential is used, the remainder term will also include short-range electron correlation [25].

The solvent polarization effects due to the EFP1 fragment molecules are included only in the optimization of the reference wavefunction, chosen to be the HF/EFP1 solution. The CC equations are then solved using the optimized solvent field of the reference state and the HF Hamiltonian modified by the Coulomb, polarization, and remainder contributions from the EFP1 solvent molecules. A more rigorous approach to combining the EFP1 solvent

model with CC theory would require a coupled iterative procedure that includes the solvent polarization due to the EFP1 fragment molecules in the optimization of both the reference and CC electron density. Such a procedure would require the calculation of the CC reduced one-particle density matrix at every iteration. Fortunately, previous studies suggest that such very time-consuming calculations are not necessary. In the present approach, each CC/EFP1 calculation has a computational cost that is equivalent to a gas-phase CC calculation on the QM region.

3. Computational Methods

All calculations were performed using the General Atomic and Molecular Electronic Structure System (GAMESS) quantum chemistry code [45] and visualized using MacMolPlt [88]. Core orbitals were frozen for all reported calculations.

Hydrolysis of 1-methylsilatrane

The reaction pathway for the hydrolysis of 1-methylsilatrane proceeding through a 4-center (1 water) and 6-center (2 waters) transition-state in the presence of two DFT-based EFP1 waters [25] was calculated using MP2 and the 6-31G(d) basis set [89-92]. Reactants, intermediates, and products were characterized by a positive definite Hessian matrix (second derivative matrix of the energy with respect to nuclear coordinates). Transition state structures were characterized by a single negative value in the Hessian matrix. Intrinsic reaction coordinate (IRC) calculations with the Gonzalez-Schlegel second-order algorithm and a step size of 0.05 $(amu)^{1/2}$ bohr were used to link transition state structures with corresponding reactants and products [93]. Relative energies were obtained by conducting single-point calculations using the CR-CC(2,3)/EFP1 method and the 6-31G(d) basis set at all MP2/EFP1/6-31G(d) stationary points on the reaction pathway, denoted CR-CC(2,3)/EFP1//MP2/EFP1/6-31G(d). Comparisons are made to fully *ab initio* calculations by replacing the EFP1 fragments with QM waters.

Anion Solvation

Global minimum energy structures for the interior and exterior solvated hydroxyl anion, $OH^-(H_2O)_{n=14, 16}$ [94] with 14 and 16 HF-based EFP1 waters [23] were obtained using a MC [95]/simulated annealing (SA) [96] approach with the hydroxyl anion defined with HF and the 6-31++G(d,p) basis set. The relative energies of solvated hydroxyl anion were calculated using the CCSD(T)/EFP1 method and the 6-31++G(d) basis set. Comparisons are made to fully *ab initio* calculations by replacing the EFP1 fragments with QM waters.

Global minimum energy structures for the interior and exterior solvated nitrate anion $NO_3^-(H_2O)_{15}$ [33] with 15 DFT-based EFP1 waters were obtained using a MC/SA approach with the nitrate anion defined with MP2 and the DH(d,p) basis set [97]. The relative energies of solvated nitrate anion were calculated using the CCSD(T)/EFP1 method and the 6-31+G(d). Comparisons are made to fully *ab initio* calculations by replacing the EFP1 fragments with QM waters.

Solvent-Induced Shift of the π→π Excitation of p-Nitroaniline in Water*

Solvatochromic (solvent induced) shift values are calculated as the difference between gas- and condensed-phase vertical excitation energies of *p*NA. The lowest singlet π→π* vertical excitation energy was calculated for each system. In the condensed-phase, the π→π* vertical excitation energy of the solute is taken as the central value of a Gaussian function fitted to the histogram of calculated vertical excitation energies.

The computational methodology employed to obtain the structures used in the solvent induced shift calculations of the π→π* excitation of *p*NA in water has been outlined in a separate work [81]. The structure of the solute used in the gas-phase excited-state calculation was obtained from an optimized ground-state geometry of *p*NA calculated with DFT using the Becke 3-parameter (exchange) [98] and Lee-Yang-Parr (correlation) [99] (B3LYP) hybrid functional [100] and the DH(d,p) basis set, in C1 symmetry. Condensed-phase structures were obtained from snapshots of a 20 picosecond QM/MM (B3LYP/EFP1) MD simulation production run of *p*NA with 150 EFP1 waters (2000 configurations). Both gas- and condensed-phase vertical excitation energies for the π→π* excitation of *p*NA were calculated using the EOM-CCSD [101-103] method with the DH(d,p) basis set.

Comparisons are made with the CIS(D)/EFP1/6-31+G(d) calculations of Kosenkov and Slipchenko [42] and experimentally observed solvent shift values.

Additional EOM-CCSD excited-state calculations using the 6-31+G(d) basis set were performed on the gas-phase structure and a set of statistically uncorrelated condensed-phase configurations [104] to investigate the basis set dependence on the calculated solvent-induced shift. A total of 58 statistically uncorrelated configurations were needed to obtain the converged average of 2000 snapshots.

4. Results and Discussions

Hydrolysis of 1-methylsilatrane

The single-point CR-CC(2,3)/EFP1/6-31G(d) calculated barrier heights and net reaction energies, $\triangle E_{reaction}$, for the neutral hydrolysis of 1-methylsilatrane in the presence of two EFP1/DFT waters are summarized in Table 1.

Table 1. CR-CC(2,3)/EFP1//MP2/EFP1/6-31G(d) calculated barrier heights and net reaction energy (kcal/mol) for the hydrolysis of 1-methylsilatrane in the presence of two EFP1 waters. Fully *ab initio* CR-CC(2,3)//MP2/EFP1/6-31G(d) values are given in parentheses. CR-CC(2,3)//MP2/6-31G(d) values from ref. [51] are shown in square brackets for comparison.

	$E(TS_{HYD})$			$E(TS_{POST})$			ΔE(Reaction)		
Transition-State	Number of EFP1 Waters*			Number of EFP1 Waters*			Number of EFP1 Waters*		
Type/QM Waters	2		0	2		0	2		0
4-center/1 water	33.6	(33.4)	[37.2]				5.9	(3.8)	[4.7]
6-center/2 water	32.3	(29.0)	[34.3]	21.9	(18.8)	[22.1]	9.9	(6.4)	[3.8]

* The number of EFP1 waters is in addition to the number of QM waters participating in the hydrolysis reaction.

The experimental activation energy for the neutral hydrolysis of 1-methylsilatrane, Eq. (6), is 12.1 kcal/mol [105].

$$N(CH_2CH_2O)_3Si{-}CH_3 + 3H_2O \rightarrow N(CH_2CH_2OH)_3 + CH_3{-}Si(OH)_3 \qquad (6)$$

In the presence of one QM water, 1-methylsilatrane hydrolyzes through a mechanism involving the formation of a 4-center transition state between the hydrolyzing water and the

silatrane framework, TS_{HYD} in Figure 1. In the presence of two QM waters, the hydrolysis mechanism for 1-methylsilatrane proceeds through a 6-center transition state with the additional water serving as a proton shuttle, TS_{HYD} in Figure 2.

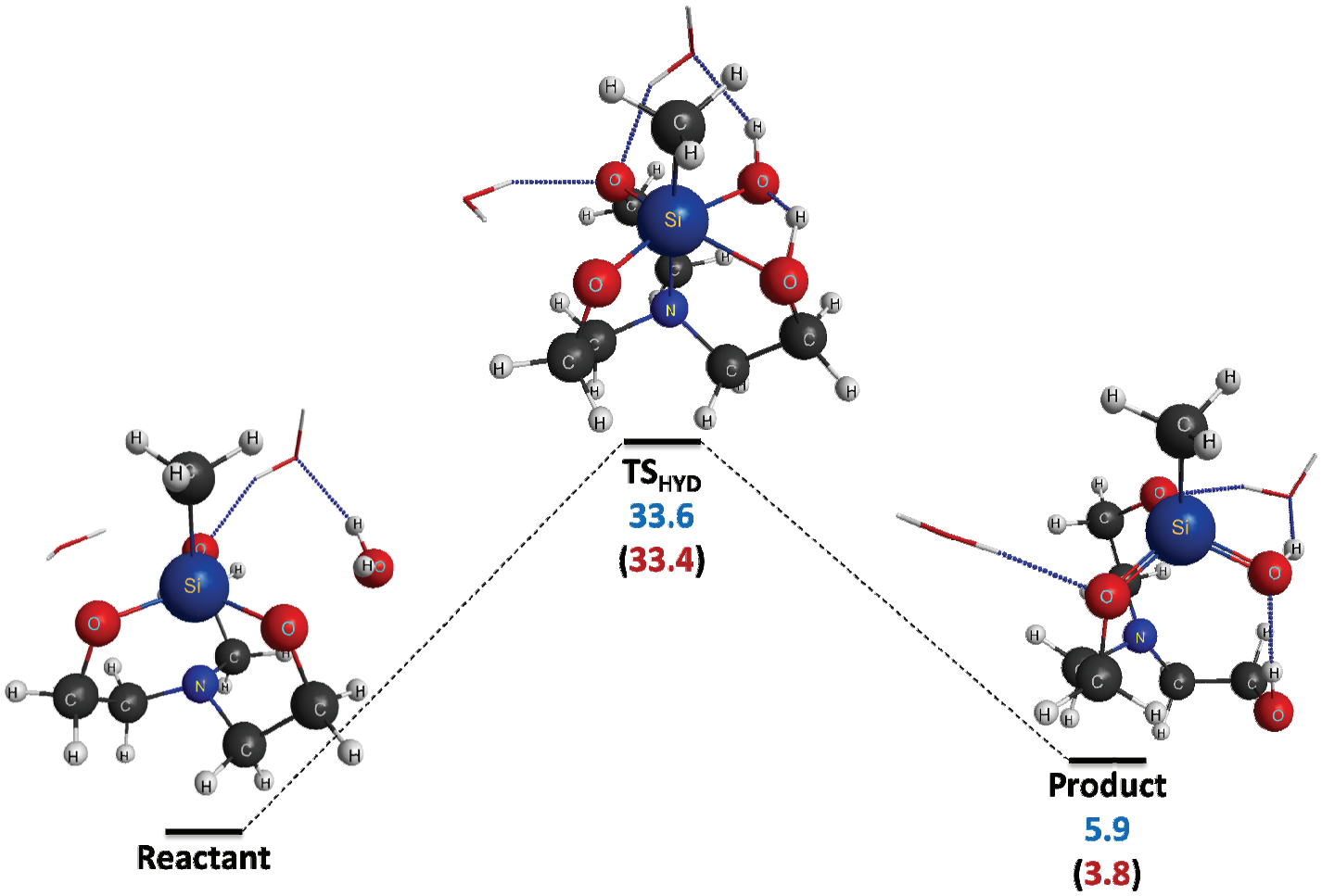

Figure 1. MP2/EFP1/6-31G(d) calculated reaction pathway for the hydrolysis of 1-methylsilatrane involving a four-center transition-state (one water molecule) in the presence of two EFP1 waters (displayed as wire frame). CR-CC(2,3)/EFP1/6-31G(d) calculated single-point energies (kcal/mol) on stationary-point geometries obtained at the MP2/EFP1/6-31G(d) level of theory are shown (blue online). Fully *ab initio* CR-CC(2,3)/6-31G(d) single-point energies are given in parentheses (red online). Energy values are relative to reactant.

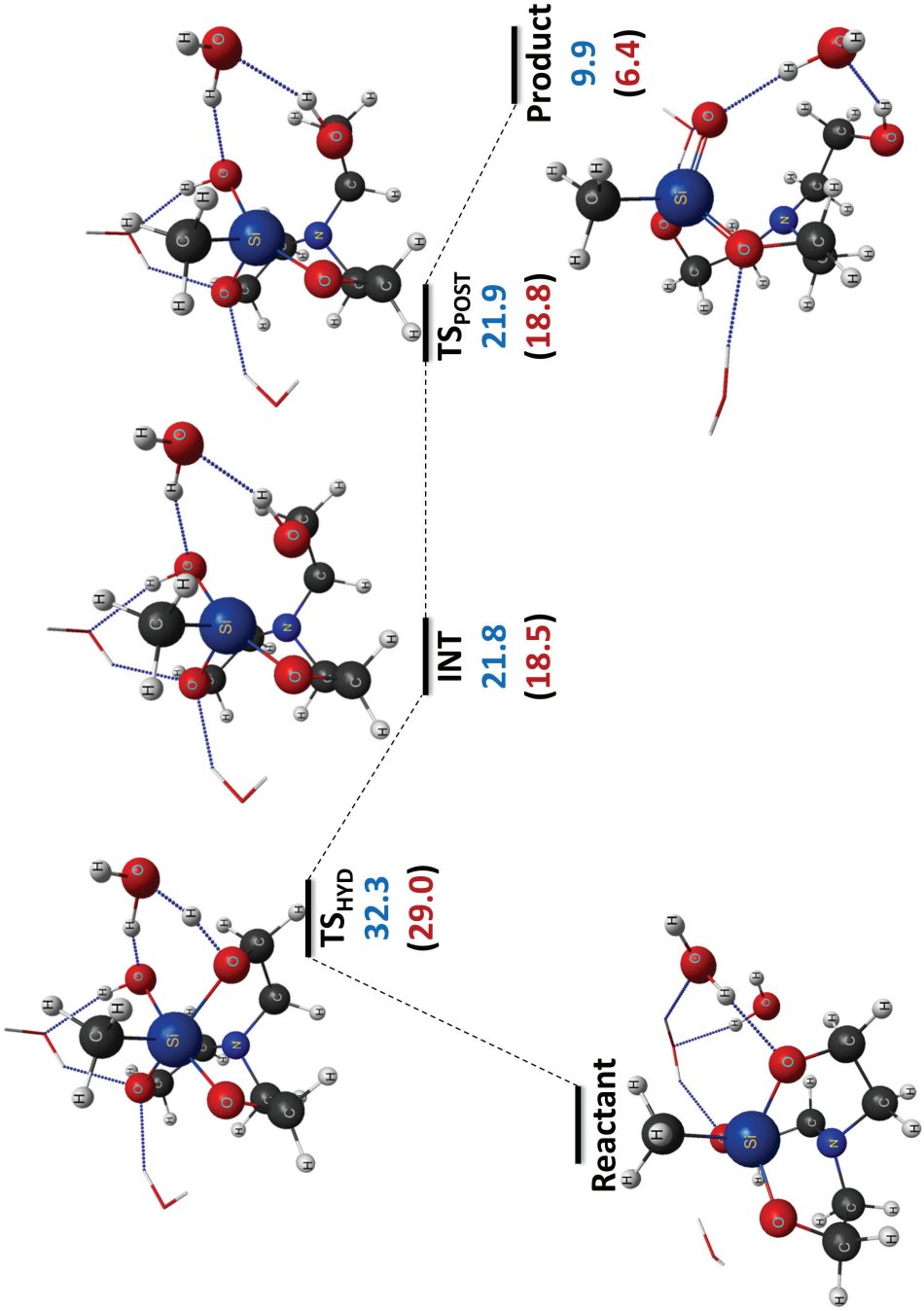

Figure 2. MP2/EFP1/6-31G(d) calculated reaction pathway for the hydrolysis of 1-methylsilatrane involving a six-center transition-state (two water molecule) in the presence of two EFP1 waters (displayed as wire frame). CR-CC(2,3)/EFP1/6-31G(d) calculated single-point energies (kcal/mol) on stationary-point geometries obtained at the MP2/EFP1/6-31G(d) level of theory are shown (blue online). Fully *ab initio* CR-CC(2,3)/6-31G(d) single-point energies are given in parentheses (red online). Energy values are relative to reactant.

The single-point CR-CC(2,3)/6-31G(d) calculated gas-phase values [51] suggest that the barrier to hydrolysis, $E(TS_{HYD})$, is overestimated compared to experiment for both 4-center (1 water) and 6-center (2 waters) reaction pathways. As demonstrated in Table 1, the addition of two EFP1/DFT water molecules reduces the barrier to hydrolysis by 3.6 and 1.9 kcal/mol for the 4-center and 6-center reaction pathways, respectively. The reduction in the barrier to hydrolysis emphasizes the importance of the environment (not captured in the previous paper), and is likely due to stabilization of the transition state by hydrogen bonding of the EFP1 water molecules with the chemically active quantum region. These EFP-QM hydrogen bonding interactions are illustrated in Figures 1 and 2. It is likely that adding additional EFP water molecules will further reduce the predicted barrier heights [106]. The discrepancy between single-point CR-CC(2,3)/EFP1/6-31G(d) and fully *ab initio* calculations, where the EFP1 waters are replaced by QM waters, is less than 4 kcal/mol.

Anion Solvation

Relative energies of surface and interior solvated structures of the hydroxyl (OH^-) anion in the presence 14 and 16 EFP1/HF1 waters are listed in Table 2. The CCSD(T) and HF relative energies are very similar. The CCSD(T)/EFP1/6-31++G(d) method predicts the interior structure (Figure 3b) to be 4.1 kcal/mol higher in energy than the global minimum structure (Figure 3a) at 14 waters. For 14 waters, the CCSD(T)/EFP1/6-31++G(d) is in excellent agreement with the fully *ab initio* values, differing by less than one kcal/mol. For 16 waters, the difference between the all-QM and the CCSD(T)/EFP predictions is a bit larger, 2.9 vs. 0.6 kcal/mol. So, the fully *ab initio* calculations predict that the surface and interior solvated structures are nearly isoenergetic. Analysis of the largest CC amplitudes indicates a delocalized CC wavefunction for the interior solvated hydroxyl anion at 16 waters with excitations involving the water cage. It may be that the EFP method has difficulty capturing this delocalization effect.

Figure 3. HF/EFP1/6-31++G(d,p) MC/SA minimum energy structures for OH^- with 14 and 16 waters: (a) hydroxyl on the surface, global minimum with 14 waters; (b) interior hydroxyl, local minimum with 14 waters; (c) hydroxyl on the surface, global minimum with 16 waters; (d) interior hydroxyl, local minimum with 16 waters. CCSD(T)/EFP1/6-31++G(d) calculated single-point energies (kcal/mol) are shown (blue online). Fully *ab initio* CCSD(T)/6-31++G(d) single-point energies are given in parentheses (red online). Energy values are relative to the respective global minimum structure. The oxygen atom of the hydroxyl anion is circled (green online).

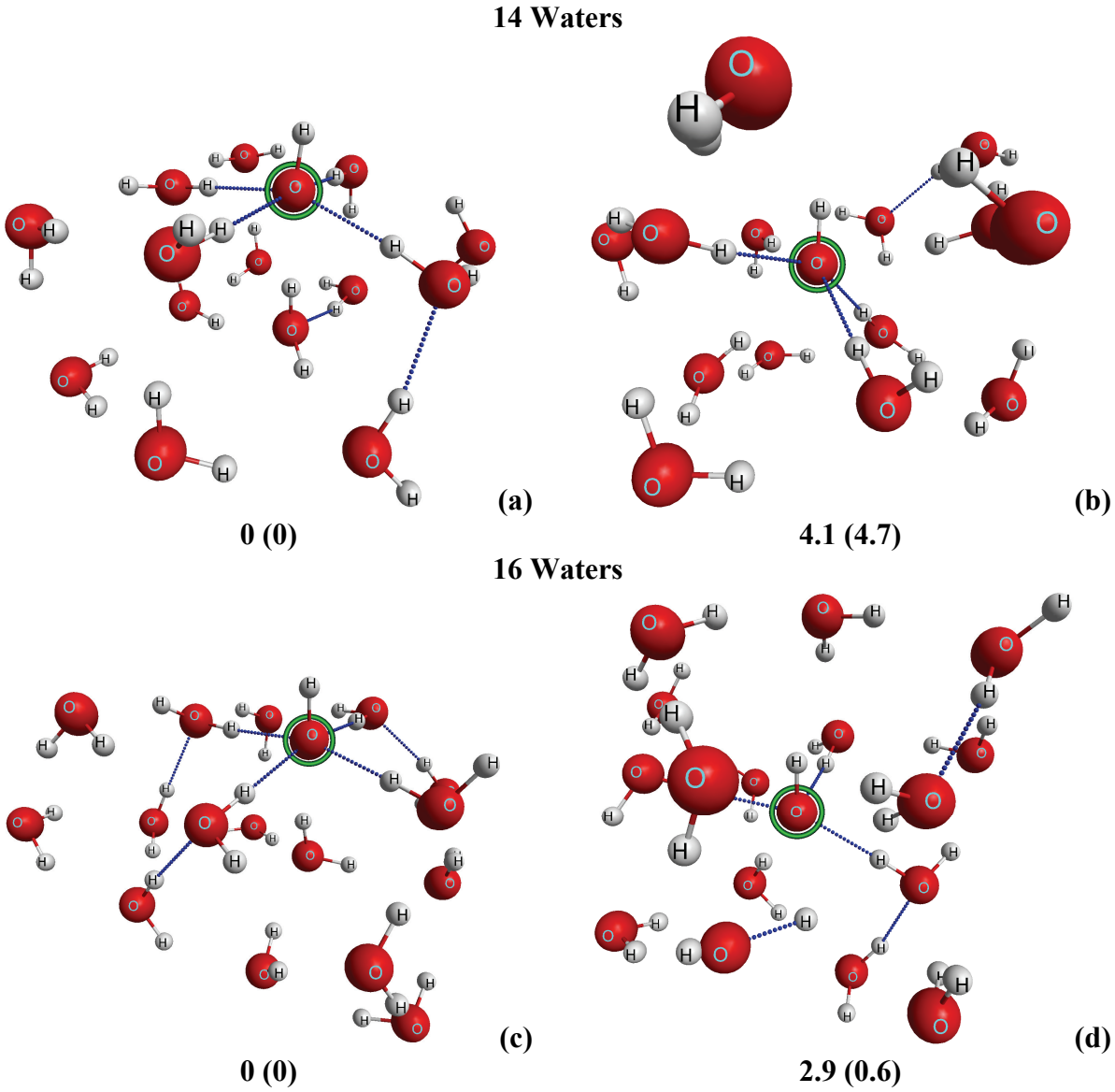

Relative energies of surface and interior solvated structures of the nitrate anion (NO_3^-) in the presence of 15 DFT-based EFP1 waters are listed in Table 3. The CCSD(T)/EFP1/6-31+G(d) method, in which all water molecules are treated with EFP1/DFT, predicts the interior solvated structure (Figure 4c) to be 6.7 kcal/mol higher in energy than the MC/SA global minimum surface structure (Figure 4a). Fully *ab initio* calculations (all waters are QM) suggest only a 1.0 kcal/mol difference between the interior solvated and global minimum surface structure for the nitrate anion with 15 waters. Analysis of the largest CC amplitudes again suggests a highly delocalized CC wavefunction with excitations involving the water cage, a phenomenon that the EFP method may not be able to fully capture.. The difference between CCSD(T)/EFP1/6-31+G(d) and fully CCSD(T) relative energies is much smaller for the local minimum surface structure (Figure 4b), 1.3 kcal/mol. The most important point here is that while there are small differences in relative energies between CCSD(T) and CCSD(T)/EFP relative energies, on the order of 5 kcal/mol or less, both sets of calculations predict that when only 15 water molecules are present, interior and surface structures are energetically competitive. This prediction is in significant contrast to the prediction of MD simulations with simple force fields that suggest that 300 or more water molecules are needed for the interior structures to be energetically competitive [33].

Figure 4. MP2/EFP1/DH(d,p) MC/SA minimum energy structures for NO_3^- with 15 EFP1 waters (displayed as wire frame): (a) nitrate on the surface, global minimum; (b) nitrate on surface, local minimum; (c) interior nitrate, local minimum. CCSD(T)/EFP1/6-31+G(d) calculated single-point energies (kcal/mol) are shown (blue online). Fully *ab initio* CCSD(T)/6-31+G(d) singlet-point energies are given in parentheses (red online). Energy values are relative to the global minimum structure.

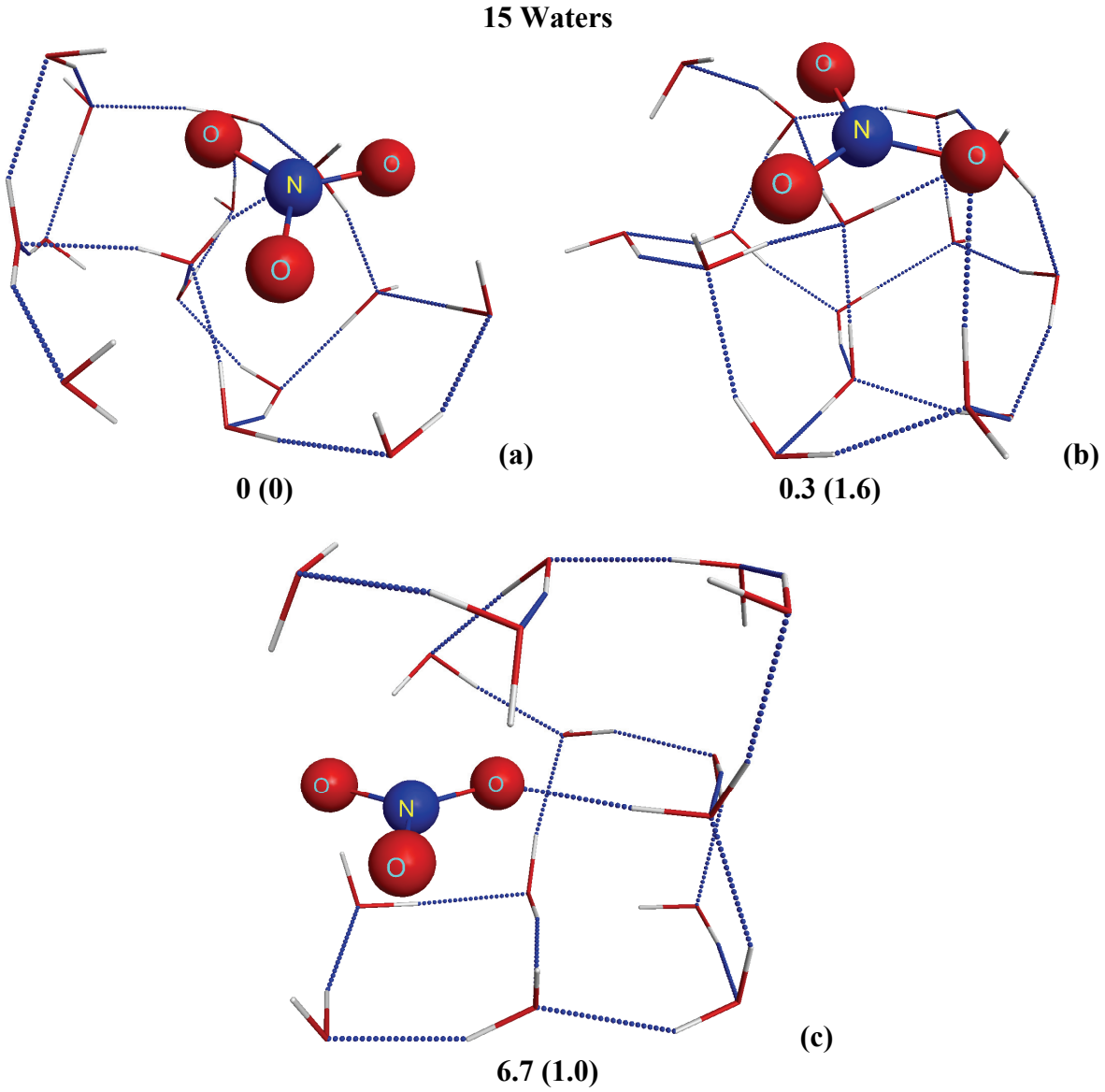

Solvent Induced Shift of the π→π Excitation of p-Nitroaniline in Water*

The simulated spectrum of the lowest singlet π→π* charge-transfer excited state of *p*NA in the condensed phase is shown in Figure 5. The EOM-CCSD/EFP1/DH(d,p) calculated charge-transfer band is centered at 3.47 eV.

Figure 5. Simulated condensed-phase spectrum for the π→π* excitation of *p*-nitroaniline (dashed line). Gaussian function centered at 3.47 eV fitted to the histogram of EOM-CCSD/EFP1/DH(d,p) calculated π→π* vertical excitations energies on 2000 configurations obtained from a 20 picosecond QM/MM (B3LYP/EFP1) MD simulation production run.

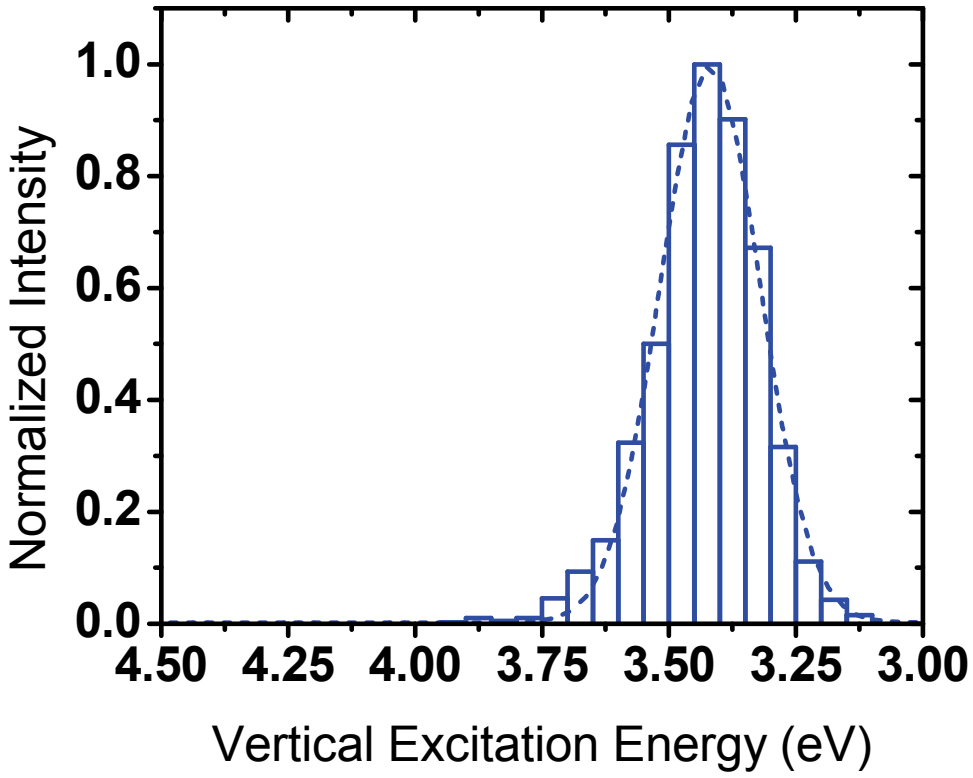

The dominant molecular orbitals involved in the π→π* transition are illustrated in Figure 6. The zwitterionic character of the ground state of *p*NA has been observed to increase in aqueous solution as compared to the gas-phase [81]. Upon excitation, electron density from the amino group is transferred to the nitro group and results in a further increase in zwitterionic (charge-separated) character. The red shift observed in the lowest singlet π→π*

charge-transfer excited state in water is likely due to the stabilization of the zwitterionic character through hydrogen bonding [79-81].

Figure 6. *p*-nitroaniline π and π* molecular orbitals

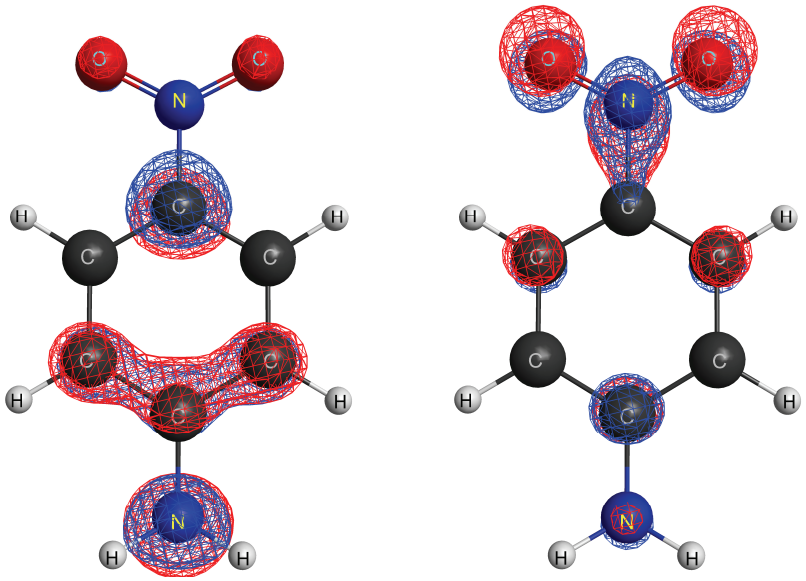

Table 4. Comparison of QM/EFP1 calculated spectral line width (FWHM) and solvent shifts of the lowest singlet π→π* charge-transfer excited state of *p*-nitroaniline obtained from a 20 picosecond QM/MM (B3LYP/EFP1) MD simulation production run.

	Excitation Energy (eV) QM Method/EFP1/Basis Set					
π→π*	**TD-B3LYP/ DH(d,p)[a]**	**TD-CAM-B3LYP/ DH(d,p)[a]**	**EOM-CCSD/ DH(d,p)**	**EOM-CCSD/ 6-31+G(d)**	**CIS(D)/ 6-31+G(d)[b]**	**Exptl.[c]**
Gas	3.97	4.40	4.73	4.57	4.65	4.24
Condensed	3.37	3.50	3.45	3.41	3.65	3.26
Shift	-0.60	-0.90	-1.28	-1.16	-1.00	-0.98
Line Width	0.22	0.20	0.26	0.27	0.46	0.60

[a] Ref. [81]
[b] Ref. [42]
[c] Ref. [78-80]

For the configurations used in the current study, on average, *p*NA is found to hydrogen bond to three EFP1 water molecules. Table 4 summarizes the solvent shift for the $\pi \rightarrow \pi^*$ charge-transfer excited state of *p*NA for several QM/EFP methods. The TD-B3LYP/DH(d,p) calculated solvent shift of Sok and Gordon underestimates the experimental solvent shift by 0.38 eV [81]. Sok and Gordon have attributed the discrepancy to the incorrect long-range behavior of the exchange functional used. Slightly better results are obtained using the EOM-CCSD/EFP1/DH(d,p) method. Increasing the basis set slightly improves the agreement with experiment. However, the EOM-CCSD/EFP1 spectral full line width at half maximum (FWHM), ≈ 0.26 eV, underestimates the experimental value of 0.6 eV [80]. Predicting spectral line widths that are in agreement with experiment may require the use of periodic boundary conditions in the QM/MM MD simulations used to acquire the configurations sampled, as was accomplished by Kosenkov and Slipchenko [42].

5. Conclusions

An approach to combining CC theory with the EFP1 method for water in a QM/MM scheme has been developed in which optimization of the solvent polarization is performed in the reference state. The CC/EFP1 method was applied to the study of the hydrolysis mechanism of 1-methylsilatrane, the solvation of the hydroxyl and nitrate anions, and of the lowest singlet $\pi \rightarrow \pi^*$ charge-transfer excited state of *p*NA in water. The discrepancy between CC/EFP1 and fully *ab initio* calculated values for the systems studied in the ground-state in this work is less than ≈ 6 kcal/mol. The CC/EFP1 method developed in the current study may not be applicable for quantitative studies on delocalized systems in which many-body effects may be important. However, the CC/EFP1 method offers qualitative insight and at least semi-quantitative predictions.

The CC/EFP1 approach offers a computationally attractive option for the inclusion of environmental effects in CC calculations with the total computational cost being nearly equivalent to single gas-phase CC calculation. The low computational overhead is due in part to avoiding the computation of the CC reduced one-particle density matrix which is required in order to optimize the solvent polarization with respect to the CC wavefunction.

The results suggest that capturing solvent effects in the reference state offers a significant step towards a complete description of environmental effects with CC theory.

Acknowledgements

This work was supported by a grant from the Air Force Office of Scientific Research. The authors thank Drs. Pooja Arora and Daniel Kemp for providing their structures for OH^- and NO_3^-. Mr. Leo C. DeSesso provided invaluable assistance in reviewing and editing the manuscript.

References

1. Čížek, J. *J. Chem. Phys.* **1966**, 45, 4256.
2. Čížek, J. *Adv. Chem. Phys.* **1969**, 14, 35.
3. Čížek, J.; Paldus, J. *Int. J. Quantum Chem.* **1971**, 5, 359.
4. Crawford, D. T.; Schaefer III, H. F. An Introduction to Coupled Cluster Theory for Computational Chemist. In *Rev. Comput. Chem.*; Vol. 14, Lipkowitz, K. B., Boyd, D. B., Eds.; Wiley-VCH, New York, **2000** ; pp. 33.
5. Helgaker, T.; Jorgensen, P.; Olsen, J. *Molecular Electronic Structure Theory*, John Wiley & Sons, New York, **2000**.
6. Shavitt, I.; Bartlett, R. J. *Many-Body Methods in Chemistry and Physics: MBPT and Coupled-Cluster Theory*, Cambridge University Press, New York, **2009**.
7. Reichardt, C. *Solvent and Solvent Effects in Organic Chemistry*, 3rd Ed., Wiley-VCH, Weinheim, **2003**.
8. Canuto, S., Eds.; *Solvation Effects in Molecules and Biomolecules: Computational Methods and Applications*, Springer Science, The Netherlands, **2008**.
9. Purvis, G. D.; Bartlett, R. J. *J. Chem. Phys.* **1982**, 76, 1910.
10. Raghavachari, K.; Trucks, G. W.; Pople, J. A.; Head-Gordon, M. *Chem. Phys. Lett.* **1989**, 157, 479.
11. Onsager, L. *J. Am. Chem. Soc.* **1936**, 58, 1486.
12. Tomasi, J. *Chem. Rev.* **1994**, 94, 2027.
13. Mennucci, B., Cammi, R., Eds.; *Continuum Solvation Models in Chemical Physics: From Theory to Applications*, Wiley, Hoboken, **2007**.
14. Besley, N. A.; Hirst, J. D. *J. Am. Chem. Soc.* **1999**, 121, 8559.
15. Tomasi, J.; Mennucci, B.; Cammi, R. *Chem. Rev.* **2005**, 105, 2999.
16. Warshell, A.; Levitt, M. *J. Mol. Biol.* **1976**, 103, 227.
17. Singh, U. C.; Kollman, P. A. *J. Comput. Chem.* **1986**, 7, 718.
18. Field, M. J.; Bash, P. A.; Karplus, M. *J. Comput. Chem.* **1990**, 11, 700.
19. Gao, J.; Luque, F. J.; Orozco, M. *J. Chem. Phys.* **1993**, 98, 2975.
20. Gao, J. Methods and Applications of Combined Quantum Mechanical and Molecular Mechanical Potentials. In *Reviews in Computational Chemistry*, Vol. 7, Lipkowitz, K. B., Boyd, D. B., Eds.; Wiley-VCH, New York, **1995**, pp. 119.

21. Coutinho, K.; Rivelino, R.; Georg, H. C.; Canuto, S. The Sequential QM/MM Method and Its Application to Solvent Effects in Electronic and Structural Properties of Solutes. In *Solvation Effects in Molecules and Biomolecules: Computational Methods and Applications*; Cantuo, S., Eds.; Springer, **2008**, pp. 159.
22. Jensen, J. H.; Day, P. D.; Gordon, M. S.; Basch, H.; Cohen, D.; Garmer, D. R.; Kraus, M.; Stevens, W. J. Effective Fragment Potential Method for Modeling Intermolecular Hydrogen-Bonding Effects on Quantum Mechanical Calculations. In *ACS Symposium Series*, Vol. 569, Smith, D. A. Eds.; American Chemical Society, Washington D.C., **1994**, pp. 139.
23. Day, P. N.; Jensen, J. H.; Gordon, M. S.; Webb, S. P.; Stevens, W. J.; Krauss, M.; Garmer, D.; Basch, H.; Cohen, D. *J. Chem. Phys.* **1996**, 105, 1968.
24. Gordon, M. S.; Freitag, M. A.; Bandyopadhyay, P.; Jensen, J. H.; Kairys, V.; Stevens, W. A. *J. Chem. Phys. A* **2001**, 105, 293.
25. Adamovic, I.; Freitag, M. A.; Gordon, M. S. *J. Chem. Phys.* **2003**, 118, 6725.
26. Gordon, M. S.; Slipchenko, L.; Li, H.; Jensen, J. H. *Annu. Rep. Comput. Chem.* **2007**, 3, 177.
27. Ghosh, D.; Kosenkov, D.; Vanovschi, V.; Williams, C. F.; Herbert, J. M.; Gordon, M. S.; Schmidt, M. W.; Slipchenko, L. V.; Krylov, A. I. *J. Phys. Chem. A* **2010**, 114, 12739.
28. Chen, W.; Gordon, M. S. *J. Chem. Phys.* **1996**, 105, 11081.
29. Webb, S. P.; Gordon, M. S. *J. Phys. Chem. A* **1999**, 103, 1265.
30. Adamovic, I.; Gordon, M. S. *J. Phys. Chem. A* **2005**, 109, 1629.
31. Ferreria, D. E. C.; Florentino, B. P. D.; Rocha, W. R.; Nome, F. *J. Phys. Chem. B.* **2009**, 113, 14831.
32. Kemp, D. D.; Gordon, M. S. *J. Phys. Chem. A* **2005**, 109, 7688.
33. Miller, Y.; Thomas, J. L.; Kemp, D. D.; Finlayson-Pitts, B. J.; Gordon, M. S.; Tobias, D. J.; Gerber, R. B. *J. Phys. Chem. A* **2009**, 113, 12805.
34. Kemp, D. D.; Gordon, M. S. *J. Phys. Chem. A* **2008**, 112, 4885.
35. Krauss, M. *Computers & Chem.* **1994**, 19, 33.
36. Krauss, M.; Webb, S. P. *J. Chem. Phys.* **1997**, 107, 5771.
37. Krauss, M.; Wladowski, B. D. *Int. J. Quantum Chem.* **1998**, 69, 11.
38. Minikis, R. M.; Kairys, V.; Jensen, J. H. *J. Phys. Chem. A*, **2001**, 105, 3829.
39. Yoo, S.; Zahariev, F.; Sok, S.; Gordon, M. S. *J. Chem. Phys.* **2008**, 129, 144112.
40. Arora, P.; Slipchenko, L. V.; Webb, S. P.; DeFusco, A.; Gordon, M. S. *J. Phys. Chem. A* **2010**, 114, 6742.
41. Slipchenko, L. V. *J. Phys. Chem. A* **2010**, 114, 8824.
42. Kosenkov, D.; Slipchenko, L. V. *J. Phys. Chem. A* **2011**, 115, 392.
43. Defusco, A.; Ivanic, J.; Schmidt, M. W.; Gordon, M. S. *J. Phys. Chem. A* ASAP, **April 14, 2011**.
44. Minezawa, N.; Silva, N. D.; Zahariev, F.; Gordon, M. S. *J. Chem. Phys.* **2011**, 134, 054111.
45. Gordon, M. S.; Schmidt, M. W. Advances in Electronic Structure Theory: GAMESS: A Decade Later. In *Theory and Applications of Computational Chemistry: The First Forty Years*; Dykstra, C. E., Frenking, G., Kim, K. S., Scuseria, G. E., Eds.; Elsevier, Amsterdam, **2005**; pp. 1167.

46. Hencsei, P.; Bihátsi, L.; Kovács, I.; Wagner, Ö.; *Periodica Polytechnica Ser. Chem.* **1991**, 35, 115.
47. Hencsei, P.; Párkányi, L. *Rev. Silicon Germanium, Tin, Lead Compd.* **1985**, 8 191.
48. Voronkov, M. G.; Baryshok, V. P. *Vestnik Rossiiskoi Akademii Nauk* **2010**, 80, 985.
49. Puri, J. K.; Singh, R.; Chanal, V. K.; *Chem. Soc. Rev.* **2011**, 40, 1791.
50. Møller, Chr.; Plesset, M. S. *Phys. Rev.* **1934**, 46, 618.
51. Sok, S.; Gordon, M. S. *Comp. Theoret. Chem.* Submitted
52. Fukui, K. *Acc. Chem. Res.* **1981**, 14, 363.
53. Piecuch, P.; Kucharski, S. A.; Kowalski, K.; Musiał, M. *Computer Phys. Commun.* **2002**, 149, 71.
54. Piecuch, P.; Włoch, M. *J. Chem. Phys.* **2005**, 123, 224105.
55. Takashima, K.; Riveros, J. M. *Mass Spec. Rev.* **1998**, 17, 409.
56. Finlayson-Pitts, B. J.; Pitts, J. N. *Chemistry of the Upper and Lower Atmosphere*, Academic Press, San Diego, **2000**.
57. Wayne, R. P. *Chemistry of Atmospheres*, Oxford University Press, Oxford, **2000**.
58. Frank, H. *Chemical Physics of Ionic Solutions*, John Wiley and Sons, New York, **1956**.
59. Williams, R. J. P. *Bio-inorganic Chemistry*, American Chemical Society, Washington D.C., **1971**.
60. Nissenson, P.; Knox, C. J. H.; Finlayson-Pitts, B. J.; Phillips, L. F.; Dabdub, D. *Phys. Chem. Chem. Phys.* **2006**, 8, 4700.
61. Otten, D. E.; Petersen, P. B.; Saykally, R. J. *Chem. Phys. Lett.* **2007**, 449, 261.
62. Brown, M. A.; Winter, B.; Faubel, M.; Hemminger, J. C. *J. Am. Chem. Soc.* **2009**, 131, 8354.
63. Salvador, P.; Curtis, J. E.; Tobias, D.; Jungwirth, P. *Phys. Chem. Chem. Phys.* **2003**, 5, 3752.
64. Dang, L. X.; Chang, T. M.; Roeselova, M.; Garrett, B. C.; Tobias, D. J. *J. Chem. Phys.* **2006**, 124, 066101
65. Minofar, B.; Vacha, R.; Wahab, A.; Mahiuddin, S.; Kunz, W.; Jungwirth, P. *J. Phys. Chem. B* **2006**, 110, 15939.
66. Thomas, J. L.; Roeselova, M.; Dang, L. X.; Tobias, D. J. *J. Phys. Chem. A* **2007**, 111, 3091.
67. Benjamin, I. *Chem. Phys. Lett.* **1998**, 287, 480.
68. Sinha, H. K.; Yates, K. *Can. J. Chem.* **1991**, 69, 550.
69. Sinha, H. K.; Yates, K. *J. Am. Chem. Soc.* **1991**, 113, 6062.
70. Farztdinov, V. M.; Schanz, R.; Kovalenko, S. A.; Ernsting, N. P. *J. Phys. Chem. A* **2000**, 104, 11486.
71. Sim, F.; Chin, S.; Dupuis, M.; Rice, J. E. *J. Phys. Chem.* **1993**, 97, 1158.
72. Scalmani, G.; Frisch, M. J.; Mennucci, B.; Tomasi, J.; Cammi, R.; Barone, V. *J. Chem. Phys.* **2006**, 124, 094107.
73. Das, G. P.; Dudis, D. S. *J. Phys. Chem. A* **2000**, 104, 4767.
74. Moran, A. M.; Kelley, A. M.; Tretiak, S. *Chem. Phys. Lett.* **2003**, 367, 293.
75. Cammi, R.; Frediani, L.; Mennucci, B.; Ruud, K. *J. Chem. Phys.* **2003**, 119, 5818.
76. Rashid, A. N. *J. Mol. Struct.* **2004**, 681, 57.
77. Wang, C.-K.; Wang, Y.-H. *J. Chem. Phys.* **2005**, 119, 4409.
78. Millefiori, S.; Favini, G.; Millefiori, A.; Grasso, D. *Spectrochim. Acta* **1977**, 33A, 21.

79. Thomsen, C. L.; Thøgersen, J.; Keiding, S. R. *J. Phys. Chem. A* **1998**, 102, 1062.
80. Kovalenko, S. A.; Schanz, R.; Farztdinov, V. M.; Hennig, H.; Ernsting, N. P. *Chem. Phys. Lett.* **2000**, 323, 312.
81. Sok, S.; Gordon, M. S. *J. Phys. Chem. A* To be submitted **2011**.
82. Dreuw, A.; Weisman, J. L.; Head-Gordon, M. *J. Chem. Phys.* **2003**, 119, 2943.
83. Zhao, Y.; Truhlar, D. G. *J. Phys. Chem. A* **2006**, 110, 13126.
84. Stone, A. J. *Chem. Phys. Lett.* **1981**, 83, 233.
85. Stone, A. J. *The Theory of Intermolecular Forces*, Oxford University Press, Oxford, **1996**
86. Gordon, M. S.; Mullin, J. M.; Pruitt, S. R.; Roskop, L. B.; Slipchenko, L. V.; Boatz, J. A. *J. Phys. Chem. B* **2009**, 113, 9646.
87. Slipchenko, L. V.; Gordon, M. S. *Mol. Phys.* **2009**, 107, 999.
88. Bode, B. M.; Gordon, M. S. *J. Mol. Graphics Mod.* **1998**, 16, 133.
89. Ditchfield, R.; Hehre, W. J.; Pople, J. A. *J. Chem. Phys.* **1971**, 54, 724.
90. Hehre, W. J.; Ditchfield, R.; Pople, J. A. *J. Chem. Phys.* **1972**, 56, 2257.
91. Gordon, M. S. *Chem. Phys. Lett.* **1980,** 76, 163.
92. Francl, M. M.; Pietro, W. J.; Hehre, W. J.; Binkley, J. S.; Gordon, M.S.; DeFrees, D. J.; Pople, J. A. *J. Chem. Phys.* **1982**, 77, 3654.
93. Gonzalez, C.; Schlegel, H. B. *J. Chem. Phys.* **1990**, 94, 5523.
94. Arora, P. *Private communication*. **2011**, October 31.
95. Metropolis, N.; Rosenbluth, A. W.; Rosenbluth, M. N.; Teller, Augusta, H. *J. Chem. Phys.* **1953**, 21, 1087.
96. Kirkpatrick, S.; Galatt Jr., C. D.; Vecchi, M. P. *Science*, **1983**, 220, 671.
97. Dunning, T. H. Jr.; Hay, P. J. Gaussian Basis Sets for Molecular Calculations. In *Methods of Electronic Structure Theory*; Vol. 3, Schaefer, H. F. III, Eds.; Plenum, New York, **1977** ; pp. 1-27
98. Becke, A. D. *J. Chem. Phys* **1993**, 98, 5648.
99. Lee, C.; Yang, W.; Parr, G. R. *Phys. Rev. B* **1988**, 37, 785.
100. Stephens, P. J.; Devlin, F. J.; Chadalowski, C. F.; Frisch, M. J. *J. Phys. Chem.* **1994**, 98, 11623.
101. Koch, H.; Jensen, H. J. A.; Jorgensen, P.; Helgaker, T. *J. Chem. Phys.* **1990**, 93, 3345.
102. Sekino, H.; Bartlett, R. J. *Int. J. Quantum Chem.* 1984, 18, 255.
103. Stanton, J. F.; Bartlett, R. J. *J. Chem. Phys.* **1993**, 98, 7029.
104. Coutinho, K.; Rivelino, R.; Georg, H. C.; Canuto, S. The Sequential QM/MM Method and Its Application to Solvent Effects in Electronic and Structural Properties of Solutes. In *Solvation Effects in Molecules and Biomolecules: Computational Methods and Applications*; Cantuo, S., Eds.; Springer, **2008**, pp. 159.
105. Brodskaya, É. I.; Voronkov, M. G. *Izvestiya akademii nauk SSSR, Seriya khimicheskaya* **1986,** 7, 1694.
106. Kudo, T.; Gordon, M. S. *J. Am. Chem. Soc.* **1998**, 120, 11432.

CHAPTER 6. CONCLUSIONS

Neutral and acid-catalyzed hydrolysis mechanisms of 1-substituted silatranes (R = H, Cl, F, CH_3, NH_2, OH, PH_2, SiH_3) in the presence of one and two waters were studied at the MP2/6-31G(d) and CR-CC(2,3)//MP2/6-31G(d) level of theory in Chapter 2. Catalytic protonation alters the rate-determining step of the reaction mechanism involved with neutral hydrolysis of 1-substituted silatranes by separating concerted events: siloxane bond formation of the hydrolyzing water with the silicon center, proton-transfer from the hydrolyzing water molecule to the endocyclic oxygen of the leaving group, and ring cleavage. The presence of an additional water molecule significantly lowers the energy barriers associated with the acid-catalyzed hydrolysis mechanism by stabilizing transition states and intermediates through hydrogen bonding, proton transfer mediation and ring strain reduction. In addition, atomic charges derived from electrostatic potentials illustrate the conjecture that formation of hydrolysis products during the acid-catalyzed mechanism increases the positive charge on the silicon center, promoting nucleophilic attack of additional waters. Bond order analysis of the hydrolysis mechanism for 1-hydrosilatrane supports the notion that ring cleavage during neutral hydrolysis involves bond breaking of a siloxane group, while ring cleavage during acid-catalyzed hydrolysis is likely to involve bond breaking of a silanol Si-OH bond. Solvent effects do not alter the qualitative findings, suggesting that the insights acquired from theoretical gas-phase calculations may be transferrable to experimental observations. Findings in this study mirror several experimental observations, including the hydrolytic stability of 1-substituted silatranes and enhanced rates of hydrolysis upon the addition of an acid catalyst.

In Chapter 3, the solvent-induced shift for the lowest singlet $\pi \rightarrow \pi^*$ charge-transfer excited state of *p*NA in water was investigated using the TD-DFT/EFP1 method. The condensed-phase was modeled using QM/MM (B3LYP/EFP1) MD simulations with 150 EFP1/DFT water molecules. In transitioning from the gas- to the condensed-phase in water, an increase in the zwitterionic character of the ground-state geometry of *p*NA is predicted. The increase in zwitterionic character is reflected by the structural changes in the molecular framework and an increase in the dipole moment and charge separation of *p*NA in water.

The TD-B3LYP/EFP1 method reproduces the experimentally observed red shift in water. The largest contributions to the calculated solvent-shift are from solute-solvent electrostatic interactions and solute relaxation reflecting the observed increase in dipole moment and zwitterionic character of *p*NA. The discrepancy between calculated and experimental solvent shift is due in part to the error in the calculated gas-phase vertical excitation energy for the lowest singlet $\pi \rightarrow \pi^*$ charge-transfer excited state of *p*NA. However, the TD-B3LYP/EFP1 calculated condensed-phase vertical excitation energy of the charge-transfer excited state agrees with experiment [48-50] to within ≈ 0.1 eV. Using a density functional with an improved description of long-range effects, an improvement in the calculated solvent shift is obtained. For a single snapshot, the TD-B3LYP/EFP1 method reproduces the supermolecular TD-B3LYP value of the singlet $\pi \rightarrow \pi^*$ charge-transfer excitation energy of *p*NA with 150 water molecules to within ≈ 0.16 eV with a 3000-fold decrease in the total wall clock time. The TD-DFT/EFP1 method is shown to be an accurate and efficient discrete approach to modeling environmental effects for the study of optical properties of organic chromophores in aqueous media.

Chapter 4 analyzed the performance of 24 density functionals for the calculation of vertical excitation energies within the linear response TDDFT formalism against a benchmark set consisting of 101 experimental excited state energies. Due to convergence issues in the ground state geometry optimizations, the benchmark set for mGGAs and GH-mGGAs only consisted of 60 excited states. The CAM-B3LYP (MAE = 0.22 eV) and the M06-2X (MAE = 0.17 eV) functionals are recommended for Rydberg excited states. For valence states, the B3LYP (MAE = 0.26 eV), X3LYP (MAE = 0.26 eV), PBE0 (MAE = 0.30 eV), and M06 (MAE = 0.25 eV) functionals offer equal performance. The M06-L functional is an attractive option for the calculation of valence excited states since it is a pure density functional, and it does not require the computation of the exchange integrals needed for admixture of HF exchange in GH functionals. For singlet states, the PBE0 (MAE = 0.25 eV) and M06-2X (MAE = 0.22 eV) functionals offer the best performance. For triplet states, GH functionals are needed with B3LYP (MAE = 0.31 eV), X3LYP (MAE = 0.31 eV), PBE0 (MAE = 0.32 eV), and M06-2X (MAE = 0.24 eV) performing well. The CAM-B3LYP (MAE = 1.10 eV) functional is not recommend for the treatment of triplet excited states.

Overall, the best performing pure density functional is M06-L (MAE = 0.39 eV). The best overall performing GH-GGA functional is PBE0 (MAE = 0.28 eV). The best overall performing GH-mGGA functional is M06-2X (MAE = 0.22 eV). Of the GGA functionals tested, none could be recommended since the LDA functional, SVWN (MAE = 0.54 eV), outperforms all GGA functionals overall. In light of the unresolved convergence issues for several of the mGGAs and GH-mGGAs, the best overall density functional based on the benchmark used in this study is the PBE0 functional which offers a balanced treatment of singlet (MAE = 0.25) , triplet (MAE = 0.32 eV), valence (MAE = 0.30 eV), and Rydberg (MAE = 0.25) excited states.

Chapter 5 described an approach to combining CC theory with the EFP1 method for water in a QM/MM scheme has been developed in which optimization of the solvent polarization is performed in the reference state. The CC/EFP1 method was applied to the study of the hydrolysis mechanism of 1-methylsilatrane, the solvation of the hydroxyl and nitrate anions, and of the lowest singlet $\pi \rightarrow \pi^*$ charge-transfer excited state of *p*NA in water. The discrepancy between CC/EFP1 and fully *ab initio* calculated values for the systems studied in the ground-state in this work is less than ≈ 6 kcal/mol. The CC/EFP1 method developed in the current study may not be applicable for quantitative studies on delocalized systems in which many-body effects may be important. However, the CC/EFP1 method offers qualitative insight and at least semi-quantitative predictions. The CC/EFP1 approach offers a computationally attractive option for the inclusion of environmental effects in CC calculations with the total computational cost being nearly equivalent to single gas-phase CC calculation. The low computational overhead is due in part to avoiding the computation of the CC reduced one-particle density matrix which is required in order to optimize the solvent polarization with respect to the CC wavefunction. The results suggest that capturing solvent effects in the reference state offers a significant step towards a complete description of environmental effects with CC theory.

ACKNOWLEDGEMENTS

It is an honor to thank those who made this dissertation possible. This body of work would not have been completed were it not for the help of my research advisor, committee members, and the encouragement of teachers, educators, family, and friends.

I offer my sincerest gratitude to my research advisor, **Mark S. Gordon**, for his patience, support, and resources during my adventures at Iowa State University. Mark has shared with me the importance of "getting the right answers, for the right reasons". His Socratic method of teaching has made the field of quantum chemistry interesting and enjoyable to learn. Mark's guidance and wisdom with respect to research and life (baseball) has become the example that I strive to follow. Above all, I thank Mark for suggesting that I apply to Iowa State University. My experience in graduate school has been academically rewarding and exceptionally entertaining, to say the least.

I thank my program of study committee members for keeping me on task over the years and for their time and effort invested in reviewing my dissertation. I thank **Klaus Schmidt-Rohr** and **Xeuyu Song** for their teachings of quantum and statistical mechanics, respectively, and laying the foundation for my research. I thank **Thomas A. Holme** for his insightful questions and comments and **Kai-Ming Ho** for offering a physicist's perspective of my research.

The members of the Gordon research group have greatly contributed to my personal and professional maturation at Iowa State. The group has been a source of collaboration, knowledge, good humor, and friendship. I am especially grateful to the group members in the Vault at 201 Spedding Hall: **Luke Roskop** and **Spencer Pruitt** for offering a Minnesotans perspective on research and life; **Andrey Asadechev** for his daily offerings of poetic humor; and honorary Vault member **Nuwan De Silva** for enduring the pranks over the years. I thank **Mike Schmidt** for answering my coding related questions and forwarding emails to me from confused users running GAMESS on Microsoft Windows operating systems.

I thank the **Early Identification Program of George Mason University** (Fairfax, VA), my undergraduate institution, for seeing the potential in me at an early age. My family

immigrated to the United States from Cambodia in the early 1980's as refugees. I grew up with no father figure and my mother struggled to raise a family on her own. I found myself becoming heavily involved with gang activity prior to attending high school. Without the support and encouragement of many teachers and educators from the Early Identification Program this body of work would not have been possible, let alone graduating high school and attending college. I especially thank **Hortensia B. Cadenas**, **Alan G. Merten**, and the late **Doris Pulliam** for their role in my academic achievements and continued success.

I thank the teachers from **Arlington County Public Schools** who helped foster my interest in the sciences: **Mary Wright**, **Susan Hu**, and **Thomas Cruger**. My first science experiment was conducted under the care of **Mary Wright** at Barcroft Elementary School. I appreciate her continued encouragement during my studies at Iowa State.

I thank the members of **N.E.R.D.** for inspiring me through their music and **Pharrell Williams** for sharing the mantra that *wealth is of the heart and mind and not the pocket*.

I thank my friends for their support over the years. I especially thank **Leo C. DeSesso**, **Marvin Fuentes**, **Michelle D. Patena**, **Buntheon Chea**, **Won Lee**, **Tai Nguyen**, **Lamont Sovidaray**, **Ian Custalow**, **Vanna Hong**, and **Steven P. Carter** for good company and bearing witness to my growth from a young street kid to a scientist. I am deeply indebted to **Leo C. DeSesso** for his invaluable assistance in reviewing and editing my dissertation. I can safely say that I am more proficient in using semicolons in technical writing.

I thank my family for their love and encouragement. I thank my mother, **Phy Leang**, for checking up on me from time to time to ensure that I was eating well. I thank my brothers, **Sareoum Sok** and **Tony Leang**, for taking care of the family during my absence. I am grateful to my youngest sibling, **Lisa Leang**, for looking up to me as a role model and giving me the motivation to achieve.

Lastly, I express my deepest gratitude to my love **Julie H. Benalja** who has been supportive, patient, and faithful during my time at Iowa State. I thank her for keeping me grounded, putting up with my late nights, and never giving up on our relationship despite being separated by 1043 miles.

Sincerely,